

# POLITECNICO DI TORINO

**Corso di Laurea Magistrale in Ingegneria Biomedica**

## Tesi di Laurea Magistrale

“Electrospun polycaprolactone nanofibrous membranes loaded with Manuka Honey, Chitosan and essential oils by layer-by-layer assembly for antibacterial wound dressings”



**Politecnico  
di Torino**

**RELATORI**

Prof. Piergiorgio Gentile  
Prof. Irene Carmagnola  
Prof. Chiara Tonda Turo

**CANDIDATO**

Jacopo Tommasi

A.A. 2022/2023

*Ai miei nonni,*

*Le persone più autentiche che abbia mai conosciuto*

## Abstract

In this day and age, one of the main causes of discomfort in patients is chronic wounds, i.e. the prolonged inflammation that occurs during a healing process, which precludes skin regeneration and requires large expenditures of time and resources. Typical treatment for chronic wounds includes application of autografts, allografts collected from cadaver, and topical delivery of antioxidant, anti-inflammatory, and antibacterial agents. Chronic and non-healing wounds can lead to a range of adverse outcomes, including pathological inflammation, impaired angiogenesis, delayed re-epithelization, and the development of antibiotic-resistant biofilms. Additionally, the growing concern over antimicrobial resistance (AMR) has serious implications, where pathogens no longer respond to antimicrobial agents, rendering drugs ineffective and posing a significant risk for severe infections. Consequently, there is a critical need for the advancement of innovative treatment approaches.

One of the emerging therapeutic options involves the use of medicated dressings that incorporate bioactive molecules, including natural compounds like essential oils, Manuka Honey, and chitosan. These materials exhibit antimicrobial and antibacterial properties by interacting with bacterial cells, resulting in membrane disruption and interference with the cell division process. Importantly, it is noteworthy that no documented cases of resistance have been reported thus far, underscoring the significant advantages of their use.

. Therefore, the aim of this thesis was to develop antimicrobial certain for wound treatments. This work was carried out at Newcastle University (UK). Specifically, membranes were manufactured using the electrospinning technique, by using a polycaprolactone-based solution and then, after being treated by aminolysis, coated using the layer-by-layer method with natural polyelectrolytes, as Chitosan (as polyanion), Manuka Honey (as polycation) and, at last, the essential oils, in form of nanoemulsion. At the end, the membrane was subjected to a fatigue test to verify its degree of elasticity and strength.

Subsequently, the membranes were subjected to a comprehensive set of morphological, physicochemical, and biological characterizations. To investigate the morphology of the electrospun fibers both before and after surface functionalization, Scanning Electron Microscopy (SEM) imaging was employed. Fourier Transform Infrared Spectroscopy with Attenuated Total Reflection (FTIR-ATR) was utilized to analyze the functional groups present on the surface of the samples. Furthermore, the elemental composition of the material's surface was quantitatively evaluated using the X-Ray Photoelectron Spectroscopy (XPS) technique. The effectiveness of the membranes against bacteria was

investigated on both gram positive and negative bacterial strains (*Staphylococcus aureus* and *Pseudomonas aeruginosa*);

Moreover, the membranes were tested in presence of fibroblasts cells, to verify biocompatibility. The SEM results reveal the development of the layers and the progressive growth of the coating, resulting in a final thickness of approximately 160 nanometers for a coating comprising 14 layers. Moreover, FTIR-ATR and XPS analysis showed the distinction among different coating compositions, revealing the chemical groups and elements of the used polyelectrolytes respectively. Finally , tests were carried out on the developed cell cultures, in order to verify the efficacy of the developed membrane and its biocompatibility, such as live and dead, and presto blue, after undergoing treatment with Sudan Black, showing no cytotoxicity effects after seeing fibroblast cells up to 7 days of culture.

## Sommario

Abstract .....	2
Chapter 1: Introduction .....	6
1.1 Human Skin: an overview.....	6
1.2 Wounds: pathophysiology and treatments .....	10
1.2.1 The wound healing process.....	10
1.2.2 Chronic wounds: general features and socio-economic impact .....	12
1.2.3 Wound treatment .....	13
1.3 Wound Dressings: state of the art and new approaches .....	19
1.3.1 Traditional dressings.....	20
1.3.2 Modern dressings .....	20
1.3.3 Advanced & Smart dressings.....	22
1.4 Electrospinning technique: main features and biomedical applications.....	25
1.4.1 Working Mechanism.....	25
1.4.2 Parameters affecting the electrospinning process .....	27
1.4.3 Materials for the electrospinning: Polycaprolactone.....	31
1.4.4 Electrospinning applied to biomedical applications .....	32
1.5 Layer by layer assembly as a coating technique .....	34
1.5.1 Layer by Layer for biomedical applications – practical examples .....	38
1.6 Nanoemulsions .....	41
1.7 Antibacterial properties of natural compounds .....	42
1.7.1 Chitosan.....	42
1.7.2 Manuka Honey.....	44
1.7.3 Essential Oils .....	46
1.1 Aim of the work .....	50
Chapter 2: Materials and Methods .....	51
2.1 Materials.....	51
2.2 Manufacturing Methods .....	51
2.2.1 Preparation of essential oil nanoemulsions .....	51
2.2.2 Aminolysis of the membranes.....	52
2.2.3 Coating of the membranes – Layer by Layer technique .....	53

2.3	Characterization methods.....	55
2.3.1	Nanoemulsions .....	55
2.3.2	Membranes .....	57
2.4	Biological evaluation.....	62
2.4.1	Cellular Tests.....	62
2.4.2	Bacterial Tests.....	63
	Chapter 3: Results and Discussion.....	65
3.1	Nanoemulsions .....	65
3.1.2	Morphological Characterization - Transmission Electron Microscopy (TEM) .....	65
3.2	Morphological Characterization – Scansion Electron Microscopy (SEM).....	67
3.2.1	Electrospun membrane .....	67
3.3	Layer-by-layer coating.....	69
3.3.1	Morphological Characterization - Scansion Electron Microscopy (SEM) .....	70
3.3.2	Physicochemical Characterization.....	72
3.4	Biological evaluation .....	89
3.4.1	Cellular tests.....	89
3.3.4.2	PrestoBlue® Assay .....	89
3.4.3	Bacterial tests.....	94

# Chapter 1: Introduction

## 1.1 Human Skin: Overview

The skin represents the body's largest organ, encompassing the entire external surface. Together with its associated structures such as hair, nails, sweat glands, and sebaceous glands, it collectively forms the integumentary system. It comprises three primary layers: the epidermis, dermis, and the hypodermis, also known as the subcutaneous layer, as illustrated in Figure 1.1 [1].

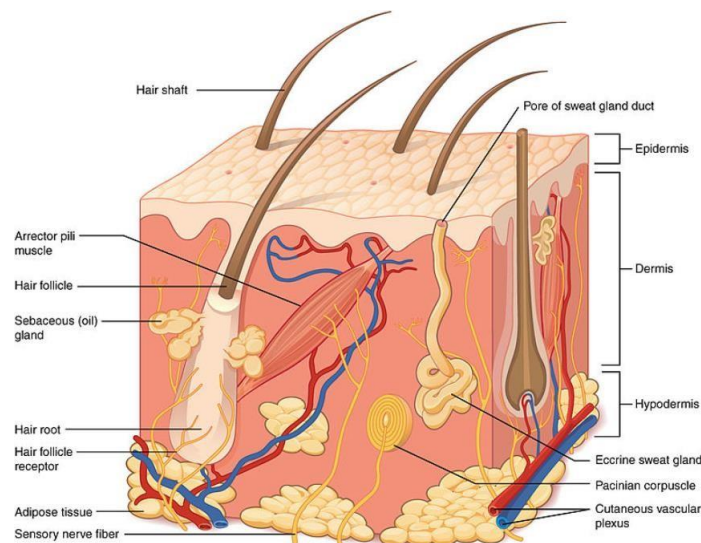


Figure 1.1 Representation of the Skin Layers: Epidermis, Dermis and Hypodermis. (Figure 5.2 of Anatomy and Physiology, OpenStax College)

The outermost layer of the skin is the epidermis, consisting of five layers, namely the stratum germinativum, spinosum, granulosum, lucidum, and corneum. Importantly, the epidermis lacks its blood supply and relies on nutrient diffusion for sustenance. The epidermal cells predominantly comprise keratinocytes, accounting for about 80% of the cell population. Additionally, there are dendritic cells, including melanocytes, Langerhans cells, and Merkel cells, responsible for pigmentation, immune response, and tactile sensitivity, respectively. Keratinocytes play a vital role in synthesizing keratin, a structural protein. They originate from the deepest layer, the stratum germinativum, and are continually pushed towards the surface of the epidermis in a process known as 'keratinization.' This process involves distinct phases of synthesis and degradation, resulting in the transformation of these cells from living polygonal cells to flattened, squamous, and non-living cells [1] [2]. The interface between the epidermis and the dermis is marked by the presence of the dermal-epidermal junction. This junction serves the dual

purpose of anchoring the two layers together and facilitating nutrient exchange [3].

The dermis, situated as the intermediate layer of the skin, primarily comprises collagen (approximately 70%) [4], along with elastin and hyaluronic acid. It imparts elasticity and tensile strength to the skin [2]. This layer consists of two distinct parts: the papillary dermis, which lies immediately beneath the epidermis and is relatively thin, and the reticular dermis, which is thicker and positioned between the papillary dermis and the hypodermis [4]. While it is mostly acellular, certain cellular components, including fibroblasts, macrophages, adipocytes, and mast cells, can be found within the dermis. Furthermore, the dermis houses glands, nerve endings, hair follicles, blood vessels, and touch receptors [2].

Beneath the dermis lies the hypodermis, a thicker layer characterized by loose connective tissue and adipose (fat) tissue. This layer contains blood vessels, nerves, lymphatic vessels, and glands [1]. The hypodermis plays a crucial role in protecting against impacts, serving as an energy reservoir, and providing insulation against cold temperatures [2] [4].

➤ **Barrier Function:**

The skin serves as a protective barrier against mechanical, thermal, and chemical factors. It also acts as a shield against microbial intrusion, UV radiation, and the loss of bodily fluids.

➤ **Sensory Function:**

The skin is rich in receptors throughout the body, contributing to the somatosensory system. These receptors can be categorized into mechanoreceptors, responsible for sensing pressure, vibrations, and texture; thermoreceptors; proprioceptors, which determine the body's relative segment positions and its position in the surrounding environment; and pain receptors.

➤ **Temperature Regulation and Insulation:**

Skin plays a pivotal role in maintaining the body's temperature. Approximately 90% of heat loss in the human body occurs through the skin. This heat exchange depends on heat transfer from internal tissues to the skin through blood vessels and heat conduction from the skin to the environment, involving mechanisms such as evaporation, conduction, convection, and radiation. This process is regulated by blood vessels, hair, sweat glands, and adipose tissue. The skin helps maintain the body's core temperature at a constant 37°C. In response to increased temperature, the skin undergoes vasodilation and sweating, while decreased temperature prompts vasoconstriction and hair straightening to conserve heat.

➤ **Immunological Defense:**

The skin provides a crucial biological defense against microorganisms. The first line of defense, known as innate immunity, includes antimicrobial substances, phagocytic cells like neutrophils and macrophages, natural killer cells, cytokines, and the complement system [7]. Innate immunity recognizes and limits microbial infections and activates adaptive immune responses. Innate immunity is rapid, nonspecific, and lacks memory [8]. On the other hand, adaptive immune responses are triggered by specific antigen recognition and can be humoral (involving B-lymphocytes) or cell-mediated (involving T-lymphocytes). Adaptive immunity is highly specific and possesses memory. Both immune responses collaborate with various immune cells in the process (see Figure 1.2).

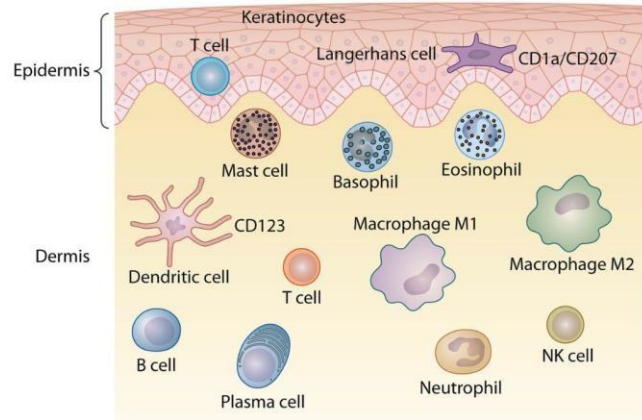


Figure 1.2 - Cells of epidermis and dermis that are responsible for innate and adaptive immune response [9].

## 1.2 Wounds: pathophysiology and treatments

### 1.2.1 The wound healing process

A wound is characterized as an interruption in the normal structure and function of a tissue [10] [11]. The processes of wound closure can lead to either regeneration or repair: regeneration involves the replacement of specific part of damaged tissue, while repair involves the deposition of collagen leading to fibrosis and the formation of a scar [11]. “A completely healed wound is defined as one that has been returned to a normal anatomical structure, function and appearance of the tissue within a reasonable period of time” [10]. The process of wound healing is intricate, involving the collaboration of cells, growth factors, and cytokines [11]. This process encompasses four distinct step: hemostasis, inflammation, proliferation, and remodeling [10] [11] [12]. It's important to note that these phases are not strictly isolated; they can overlap and occur concurrently over time [11] [13] [12] (see Figure 1.3).

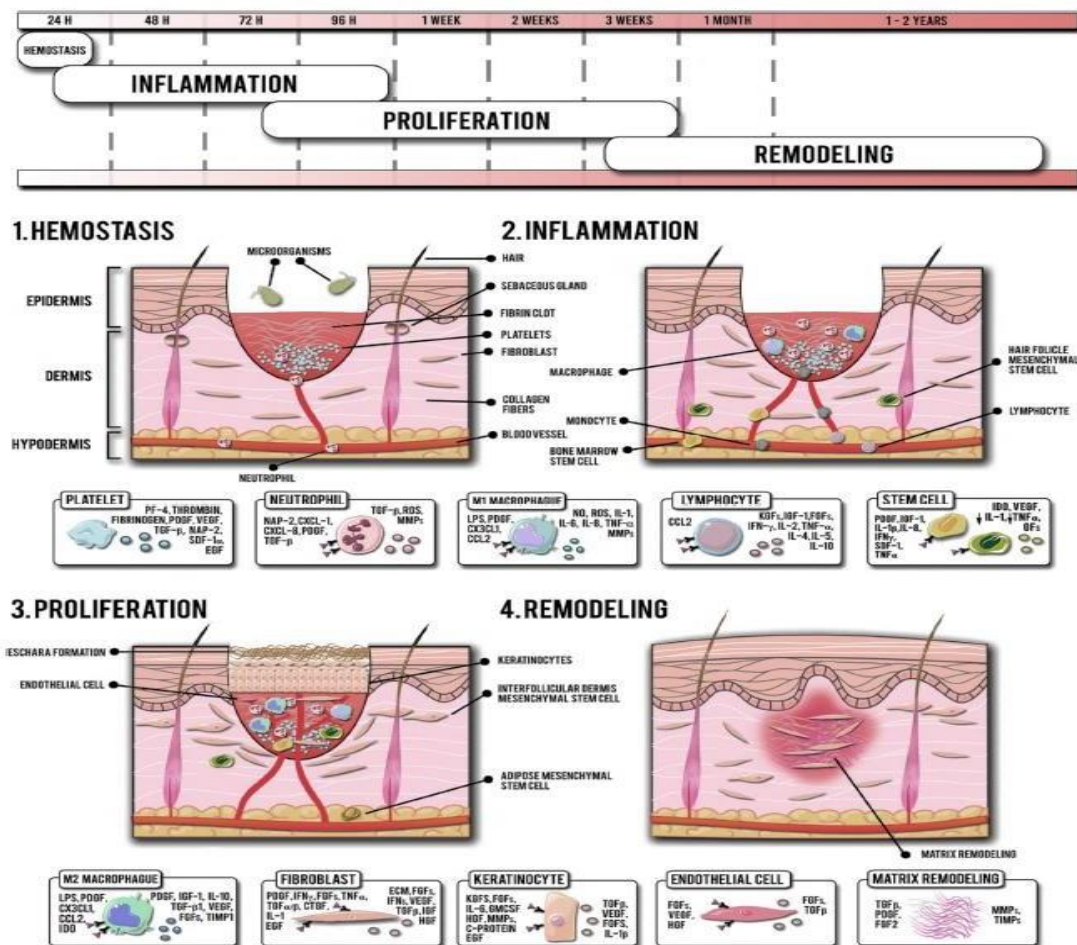


Figure 1.3 - Phases of healing process, timeline and cells involved. [14].

**Hemostasis and Coagulation:** After an injury, we have the constriction of the blood vessels, and subsequently, the formation of a fibrin network, initiating the process of coagulation [10][15]. This blood clot serves multiple functions, such as safeguarding the integrity of the vascular system, providing protection against external factors and microbes. [10] [15] [11] [12].

**Inflammation:** The inflammation phase can be divided into early and late stages [10]. During the early stage, neutrophils are recruited; their primary role is to phagocytize bacteria, eliminating them, and removing necrotic tissue [10] [11] [13]. Additionally, they attract other cells involved in the inflammatory response [11]. The late phase is characterized by the dominance of macrophages, which continue the phagocytic process, particularly targeting cellular debris [15] [11]. They also attract growth factors and other mediators, activating keratinocytes, fibroblasts, and endothelial cells to promote tissue regeneration [11]. Towards the end of the late phase, lymphocytes arrive at the site of injury, primarily acting against microbes and foreign materials [12].

**Proliferation:** The objectives of this phase encompass the establishment of granulation tissue to cover the wound, stimulating angiogenesis (the creation of new blood vessels from existing ones), and facilitating re-epithelization, as discussed in references [11] and [13]. Fibroblasts play a pivotal role during this phase, as they are responsible for generating vital components like fibronectin, hyaluronic acid, collagen, and proteoglycans, all of which are essential for the formation of the new extracellular matrix, as detailed in references [10], [11], and [12]. As a result, the provisional matrix is gradually replaced by granulation tissue [12]. In this tissue, the re-establishment of the vascular system occurs through angiogenesis, as discussed in reference [12]. The process of re-epithelization is directed by signaling pathways that involve keratinocytes and stem cells originating from sweat glands or hair follicles, as indicated in reference [11].

**Remodeling:** This step, involves the reorganization, degradation, and resynthesis of the extracellular matrix (ECM) [15], as well as the restructuring of collagen and wound contraction [12]. Finally, this phase culminates in the creation of new epithelial tissue and the formation of scar tissue [10]. The strength properties of the healed skin typically reach approximately 80% of the strength observed in intact skin, as highlighted in references [10] and [15].

### 1.2.2 Chronic wounds: general features and socio-economic impact

**Chronic Wounds:** Chronic wounds deviate from the typical healing process, often becoming arrested in one of the previously mentioned phases [12]. This leads to pathological inflammation [16], compromised angiogenesis, challenges in re-epithelization [14], and the development of drug-resistant biofilms [17]. A wound is typically categorized as 'chronic' if it fails to heal successfully within a three-month period [14]. Numerous factors can influence the wound healing process, including local factors such as infections, oxygen levels, foreign bodies, and venous insufficiency, as well as systemic factors like age, gender, stress, underlying diseases, obesity, alcoholism, smoking habits, nutrition, and immunodeficiency [13]. However, diabetes mellitus, vascular diseases, and pressure ulcers stand out as the primary clinical factors associated with chronic wounds [18] [19] (see Figure 1.4).

**Impact of Chronic Wounds:** Chronic wounds can persist for several years, significantly affecting patients' quality of life. This includes experiencing pain, reduced mobility, emotional distress, and, in severe cases, disabilities or the necessity for amputation [20].



Figure 1.4 - Factors involved in the failure of the healing process leading to the development of a chronic wound and pictures of different types of chronic wounds. That is A) Venous Leg Ulcer, B) Arterial Leg Ulcer, C) Diabetic Foot Ulcer, D) Pressure Ulcer. Images of the wounds from [21].

**Prevalence of Chronic Wounds:** It is estimated that approximately 1-2% of the population in developed countries will experience chronic wounds at some point in their lives [17] [22]. In recent years, the number of individuals afflicted by this condition has risen, primarily due to increased life expectancy and the presence of concurrent health issues [17]. Consequently, the treatment of chronic wounds poses a significant financial burden in terms of both time and resources [17].

#### Wound treatment

Chronic wounds are characterized by their complexity, and effectively managing them often necessitates the adoption of a multidisciplinary approach, as recommended in reference [24]. The first and pivotal step in delivering appropriate treatment is the comprehensive assessment of both the patient and the wound itself [24]. Following this evaluation, the process of wound bed preparation is initiated, guided by the TIME principle [24] [25] [26], which comprises the following steps:

**(T)** ->Tissue Assessment: This involves the removal of necrotic tissue and foreign bodies, such as bacteria that can form biofilms. This step is essential for creating a more conducive

environment for healing.

**(I)** ->Inflammation and Infection Management: This step entails the use of local antiseptics and/or systemic administration of antibiotics to address inflammation and infection within the wound.

(M) Effective moisture control, ensuring that the exudates are balanced: research has shown that wounds maintained in a moist environment tend to heal faster in comparison to those left dry and exposed to the air.

(E) Management of wound periphery and facilitation of epithelialization restoration.

The solutions employed to treat wounds can be summarized in five categories: systemic therapies; local therapies (dressing-free); skin grafting; skin substitutes and dressing therapies [14].

➤ **Systemic therapies:**

Antimicrobials in Wound Management: Antimicrobial agents are employed to combat microorganisms that affect wounds, including bacteria, fungi, viruses, and others [26]. These agents can take the form of antibiotics, antiseptics, or disinfectants. However, there are certain limitations associated with the systemic administration of drugs. In particular, when bacteria form biofilms, it becomes challenging for antibiotics to effectively target them [14]. Additionally, ensuring that antibiotics reach the intended target can be problematic, and they may come with side effects [14]. Moreover, the indiscriminate use of antibiotics can lead to the development of antibiotic-resistant strains of bacteria [26].

➤ **Local therapies:**

They can be physical or pharmacological treatments. The most common physical treatments are indicated in table 1.1.

**Table 1.1** Most common local physical therapies for wound treatment.

Therapy	Description	References
Compression therapy	External and gradual pressure applied by a bandage	[14]
Negative pressure wound therapy	Sub-atmospheric pressure applied by a vacuum device to eliminate exudates	[14] [26]
Hyperbaric oxygen therapy	Administration of 100% oxygen at above-atmospheric pressure (1.5 – 3 atm) to hypoxic tissues	[26] [27]
Low-power light therapy (photobiomodulation)	Red/near infrared light wavelengths are used to penetrate into the tissues and to stimulate repair and healing	[28]

Low-intensity pulsed ultrasound	An acoustic wave is produced in order to travel through tissues and to perform positive effects on reducing inflammation, enhancing proliferation and formation of granulation tissue	[28]
Extracorporeal shock waves	Mechanical energy pulses at high amplitude that are effective in increasing perfusion and oxygen amount	[28] [26]
Electrical stimulation	Conducted using a pair of electrodes, one positioned within the wound bed and the other in close proximity to the wound's surrounding skin, it has been demonstrated that the most effective form of electrical stimulation for promoting wound healing is in the form of pulsed direct current (pulsed DC).	[26] [27]
Plasma	It is a combination of gas containing negatively charged electrons and strongly charged positive ions. In this particular application, it is employed at a low temperature. Plasma is proficient in combating pathogens and has a positive impact on the activation of keratinocytes and fibroblasts.	[28] [26]

Local therapies encompass pharmacological treatments as well. Effective wound healing isn't limited to antibiotics and antiseptics but also extends to natural compounds. Some examples include essential oils, Aloe Vera, Manuka honey, eucalyptus [14] [26], growth factors, stem cells [24] [14] [28], and graphene oxide [14]. (1.7)

➤ **Skin grafting:**

In this procedure, a segment of skin is relocated from its original location to the area requiring repair [29]. Autografts are taken from the same patient, allografts are sourced from another individual of the same species, and xenografts are derived from a different species, typically animals, as outlined in references [14] and [29]. There are two types of grafts that is used: one that include the epidermis and a portion of the dermis, called split-thickness grafts, and full-thickness grafts, which encompass both the epidermis and the entire dermis [14] [29]. These grafts can also be categorized based on their donor source.

➤ **Skin substitutes:**

Skin substitutes serve the purpose of emulating natural skin without grafts from any donors. These substitutes can be made up of just the extracellular matrix or may incorporate cells, and they can be constructed from natural or synthetic materials. Additionally, they can be designed to be either temporary or permanent solutions. Several examples of skin substitutes include Biobrane<sup>®</sup>, Integra<sup>®</sup>, Alloderm<sup>®</sup> (which are acellular skin substitutes), as well as Transcyte<sup>®</sup>, Dermagraft<sup>®</sup>, and Apligraf<sup>®</sup> (cellular skin substitutes) [30].

➤ **Dressing therapies:**

The use of wound dressings dates back to ancient times, with civilizations like the Mesopotamians, Egyptians, and Ancient Greeks employing techniques such as washing wounds with substances like wine, vinegar, or milk, followed by the application of honey, resin, or medicinal herbs. These treatments were then covered with materials like linen or boiled wool. The 19th century witnessed a significant advancement in wound management with the introduction of antiseptics. Subsequently, in the 20th century, the first modern dressings were developed [31] [32] [33].

Emergence of Smart Wound Dressings: Presently, there is ongoing research and development in the field of smart wound dressings. The following section will delve into dressing therapies in more detail.

### Tissue Engineering in Wound Care:

Skin substitutes and specific categories of dressings are essential components of tissue engineering techniques. "Tissue engineering (TE)" is a multidisciplinary field that combines principles from engineering and the life sciences to develop biological replacements capable of restoring, maintaining, or enhancing tissue function [34]. Figure 1.5 provides a visual representation of the fundamental elements employed in tissue engineering, which include scaffolds, cells, and bioactive factors. Scaffolds play a pivotal role in tissue repair and reconstruction by filling empty spaces, providing structural support, and facilitating the delivery of cells and bioactive molecules [35].

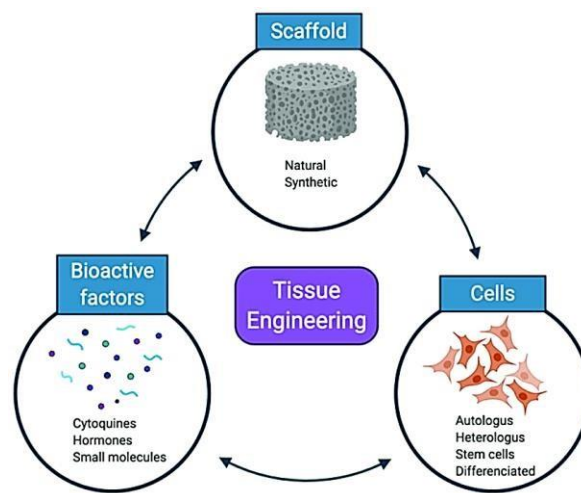


Figure 1.4 - Tissue engineering cardinal elements [36]

### 1.3 Wound Dressings: state of the art and new approaches

When we use substances to cover the wound site and contact directly with the wound itself, we are dealing with a wound dressings (WD) [33] [37]. Their primary purpose is to create an optimal environment conducive to successful healing. Although there is a wide range of dressing types, they share common goals, which encompass preventing wound infections, managing exudate and related odors, reducing patient discomfort and pain, accelerating the healing process, and concealing the wound for cosmetic reasons [37].

Figure 1.6 outlines the general requirements that dressings must meet.

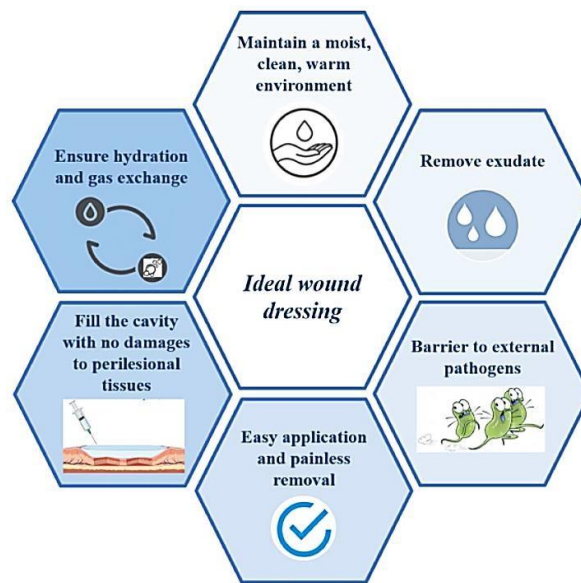


Figure 1.5 - Main requirements of an ideal wound dressing [38].

Various wound types may necessitate distinct dressings, each possessing unique functional attributes. There is no universal dressing suitable for all types of wounds [39]. Therefore, the selection of the most appropriate dressing is contingent upon the specific characteristics of the wound, which include depth, size, exudate volume, potential infection, location, and other pertinent factors [40].

### 1.3.1 Traditional dressings

These dressings are often referred to as passive and non-occlusive dressings and encompass materials such as gauze, plasters, bandages, lint, and cotton wool [33]. Their primary role is to provide mechanical protection to the wound and act as a barrier against contaminants [40] [32]. They are most appropriate for clean and dry wounds with minimal exudate [40]. However, a notable drawback is their propensity to adhere to the wound bed, causing pain upon removal and necessitating frequent changes [40] [32]. Consequently, there has been a significant shift from traditional dressings to more modern alternatives with enhanced features that are better suited for various types of wounds [33] [40].

### 1.3.2 Modern dressings

Modern dressings have been designed both to cover wounds, and to facilitate and enhance the healing process [32]. They can be categorized into four primary groups: hydrogels, hydrocolloids, films, and foams[32].

*Hydrogels* are formulated by cross-linking primarily natural-based polymers, resulting in a three-dimensional porous structure that facilitates cell migration and the deposition of the extracellular matrix (ECM), ultimately promoting re-epithelization [28]. They are characterized by their high-water content, which makes them particularly well-suited for rehydrating dry wounds and maintaining a moist environment [14]. Hydrogels can assist in autolytic debridement [42] and offer pain relief due to their cooling properties [14]. They are non-irritating, easy to apply and remove, and are cost-effective. However, it's worth noting that hydrogels are not suitable for highly exuding wounds and may not provide effective protection against pathogens [43].

*Hydrocolloids* are widely used dressings consisting of an inner gel-forming layer and an outer occlusive layer. They retain moisture, are easily removable [43], promote autolytic debridement [40], and offer better protection against bacteria compared to hydrogels. Nonetheless, their use with infected wounds is not recommended [38].

Semi-permeable films are thin polymer sheets that can conform to wound shapes with ease. They allow for gas exchange and serve as an impermeable barrier against bacteria and fluids [43]. Nevertheless, they are not suitable for highly exuding wounds due to their limited absorbent capacity [40] [43], and their removal can potentially be traumatic [43].

*Foam dressings* have a sponge-like structure with adjustable absorbent properties based

on pore size and thickness [42]. They are suitable for highly exuding wounds and maintain a moist environment at the wound bed interface. However, they are not suitable for dry or low-exuding wounds [43]. Additionally, there is a risk of tissue formation within the foam pores if not changed regularly, leading to painful removal [43].

Some commercial examples of these dressing are listed in table 1.2.

*Table 1.2 Categories of modern wound dressing and commercial examples.*

<b>Dressing</b>	<b>Example</b>
Hydrogels	Nu-gel <sup>®</sup> , Clearsite <sup>®</sup> , Hypergel <sup>®</sup> , Carrasyn <sup>®</sup> , Aquaform <sup>®</sup>
Hydrocolloids	Duoderm <sup>®</sup> , NuDerm <sup>®</sup> , Comfeel <sup>®</sup> , Cutinova <sup>®</sup> , Tegaserb <sup>™</sup>
Films	Bioclusive <sup>®</sup> , Tegaderm <sup>™</sup> , Opsite <sup>™</sup> , Hydrofilm <sup>®</sup>
Foams	Tegafoam <sup>™</sup> , Allevyn <sup>®</sup> , PermaFoam <sup>®</sup> , Lyofoam <sup>®</sup>

*Multilayer dressings* are created by combining previously treated dressings to incorporate their distinct characteristics [40] [42].

Dressings can also be medicated to enhance their effectiveness in the wound healing process [38] [40]. They can be both bioactive wound dressings and drug-loaded wound dressings [38]. Bioactive dressings can be prepared by incorporating bioactive macromolecules (such as chitosan, collagen, and alginate), which play a role in skin regeneration, as well as antimicrobial peptides (AMPs), natural antiseptics (e.g., Manuka honey), or synthetic antiseptics [38]. Drug-loaded dressings are designed to contain a cargo that is subsequently released in situ; they may include antibacterial agents, anti-inflammatory and analgesic medications, and biological factors like Growth Factors [38].

### 1.3.3 Advanced & Smart dressings

The necessity to address the constraints of conventional dressings has given rise to a novel category of dressings referred to as advanced or smart dressings. These dressings have the capability to engage with the wound environment in order to augment the response tailored to specific conditions.

**Stimuli-Responsive Dressings:** Stimuli-responsive dressings can react to changes in the physical and chemical characteristics of the wound environment, either spontaneously or through external triggers [44]. Self-responding dressings can be activated by alterations in factors like pH, temperature, chemokines/cytokines levels, reactive oxygen species (ROS), and glucose within the wound bed [38]. Externally triggered dressings, on the other hand, rely on external stimuli, such as increased temperature or exposure to near-infrared (NIR) light [38].

**Other Smart Dressings:** Additionally, there are self-healing dressings, which are suitable for body parts subject to movement and are stretchable to accommodate such movement. Self-removal dressings have been developed to reduce pain during removal, often utilizing thermosensitive or light-triggered polymers [44].

**Automated Dressings:** Over the past six years, automated dressings have been introduced [44]. These dressings are equipped with sensors to monitor wound conditions, decision-making algorithms, and actuators for drug delivery [38]. Table 1.3 provides examples of patented systems in this category.

Patent ID	Patented advanced wound dressing platforms	Patent ID Description	Classification
CN109152860A	Wound dressing comprising an acid-hydrolyzing oligomer and an acid-activable prodrug which is activated in the presence of acid environment		Self-responding wound dressing
CN108524999A	Long-term-healing wound dressing composed by different layers for the prolonged release of drugs: a quick releasing layer for the delivery of anti-bacterial agents and an acid-pH-controlled layer for long-term drug delivery		Self-responding wound dressing
US2005159695A1	Wound dressing sensitive to enzymes (e.g., elastase and collagenase) for the controlled release of therapeutic agents in the infected wound area		Self-responding wound dressing
US2006286155A1	Drug-loaded wound dressing comprising oligopeptide sequences which are cleavable by kallikrein-reach wound fluids for the controlled release of therapeutic agents		Self-responding wound dressing
GB2393656A	Wound dressing sensitive to proteases associated with wound fluids for the controlled release of therapeutic agents		Self-responding wound dressing
WO03026544A1	Wound dressing able to release the payload in response to the absorption of fluids present in the wound bed		Self-responding wound dressing

CN110665120A	Chitosan-based wound dressing equipped with flexible electronics for remote monitoring and drug release	Externally triggered wound dressing
WO2018211458A1	Fiber-based wound dressing equipped with a sensor element configured to undergo changes in response to a parameter associated to wound fluids and a supply of therapeutic agents	Automated wound dressing
CN104114136A	Automated wound dressing equipped with two field reservoirs, an electrokinetic pump and a controller for the delivery of the therapy in the wound area	Automated wound dressing

**Table 1.3** Example of patents of advanced WDs [38].

## 1.4 Electrospinning technique: Biomedical applications and Key Characteristics

Two different techniques can be used in bioengineering for the fabrication of scaffolds: conventional non-conventional methods, referred to as rapid prototyping. Conventional methods encompass the following techniques: Freeze-Drying, Solvent Casting Particle Leaching, Gas Foaming, Electrospinning, and Phase separation. Conversely, rapid prototyping involves, 3D bioprinting, Selective Laser Sintering, Fused Deposition Modeling and Stereolithography[45] [46].

In this work, the electrospinning technique has been used to fabricate membranes for wound healing applications; in this section, the focus will be put on this technique. Electrospinning, in biomedical field, is a broadly employed technique.

This technology enables the production of non-woven substrates composed of an uninterrupted network of ultrathin fibers, which range in size from tens of nanometers to a few micrometers. These substrates exhibit high porosity and possess a significantly large surface area, as discussed in references [47] and [48]. Additional benefits include the ability to tailor the porosity and shape of the substrates, as well as precise control over the composition of the nanofibers, as mentioned in reference [47].

### 1.4.1 Working Mechanism

The fundamental configuration of an electrospinning device consists of a high-voltage power source, a syringe pump, an emitter (often in the form of a needle spinneret), and a conductive collector. This setup can be arranged either vertically or horizontally, as illustrated in Figure 1.7.

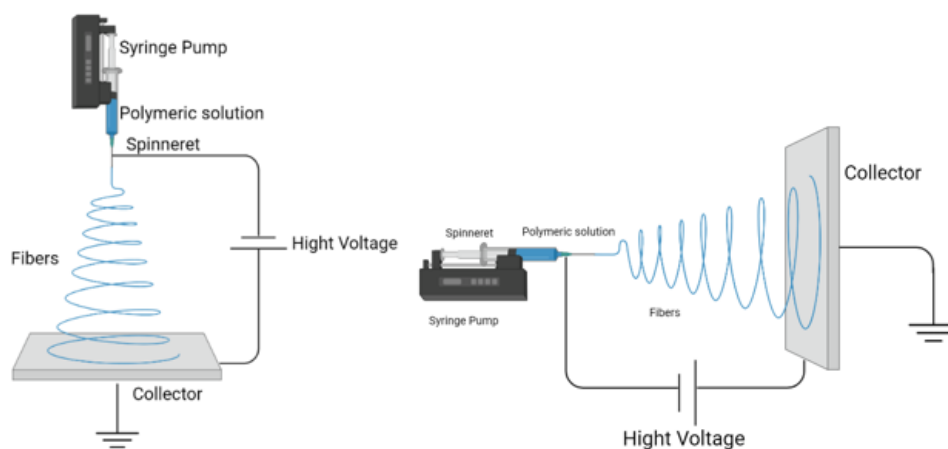
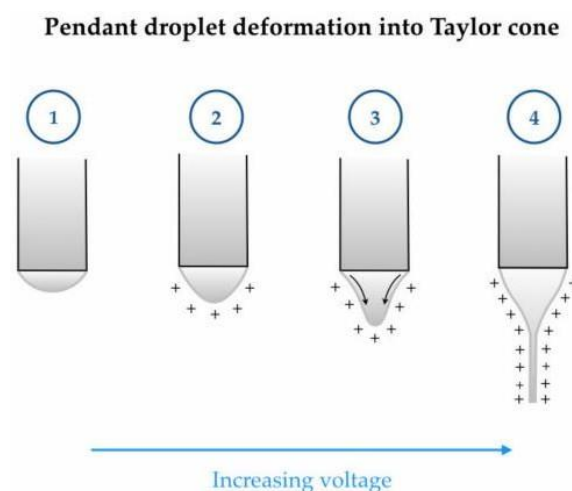


Figure 1.6 - Electrospinning setup. a) Vertical and b) Horizontal configurations [47].

In the course of the electrospinning process, the pump propels the polymeric solution through the needle-emitter, and at the needle's tip, a drop of the solution forms because of its surface tension [50] [51]. At this stage, a high voltage is applied, resulting in the electrification of the solution and the generation of surface charges [50]. These charges exhibit mutual repulsion, counteracting surface tension. Consequently, this causes the formation of Taylor cone, a drop in the shape of a cone. [50] [51] [52], directed toward the collector (counter electrode). If the droplets breaks and transform into a jet, it means that the applied voltage surpasses a critical threshold, overcoming surface tension. This mechanism is depicted in Figure 1.8.



*Figure1. 7 - 1) Droplet formation; 2) Electrification of the solution with formation of superficial charges; 3) Taylor cone; 4) Ejection of the jet of liquid [53].*

The aircraft initially adheres to a linear path as it is drawn towards the receptor. Nevertheless, it experiences disturbances that disturb its straightness, which are frequently denoted as irregularities [54] [50] [55]. These instabilities include Rayleigh instability, asymmetrical instability, and whipping/bending instability. Earnshaw's theorem provides an explanation for the occurrence of instability, stating that "An electrically charged body, when placed within an electric field, cannot maintain a stable equilibrium solely under the influence of electric forces" [55]. Our primary focus will be on the whipping or bending instability, which plays a pivotal role in the generation of submicron-scale fibers [56].

As the solvent-laden jet travels from the emitter to the collector, the solvent begins to evaporate, resulting in a reduction in the jet's diameter. This is closely associated with an elevation in the charge density on the jet's surface, leading to an increase in repulsive

forces and causing the jet to accelerate towards the collector.

The high velocity of the jet leads to the formation of bends, loops, and spirals, with the jet progressively elongating and thinning in diameter. Since each segment of the loop carries an identical electrical charge, repulsion forces drive this process to occur repeatedly, forming a conical pattern [54] [50].

Throughout this process, the solvent undergoes evaporation, and the fibers are subsequently deposited onto the collector, solidifying in the process [51] [54] [55]. This mechanism is visually represented in Figure 1.9.

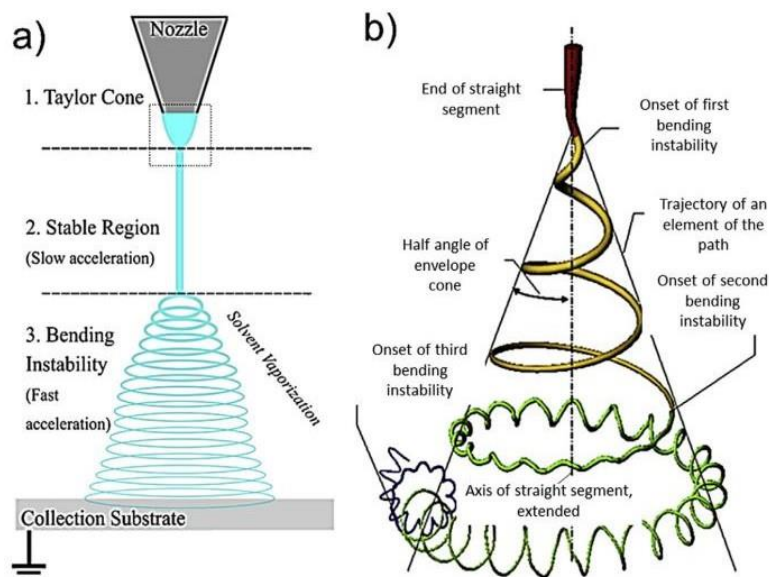


Figure 1.8 - a) Distinction between three zones of the jet: Taylor cone, linearity region and instability zone; b) Zoom of the instability zone, with a focus on bending and loops [57].

#### 1.4.2 Parameters affecting the electrospinning process

Several parameters significantly impact the electrospinning process, and these can be categorized into solution parameters, process parameters, and environmental parameters, as highlighted in references [47] and [48]. These factors crucially affect the fibres morphology so we have to control and modify in order, to obtain the desired frames and fibre diameters [47] [54].

##### ➤ Solution Parameters:

*Concentration, Viscosity and Molecular Weight* of the polymer are correlated to each other. Inadequately low values for these parameters prevent the formation of continuous fibers and instead result in the presence of droplets, a phenomenon known as electrospraying, and the appearance of beaded fibers, as illustrated in Figure 1.9 [47]. This occurs due to insufficient molecular chain entanglement, which is not robust enough to overcome surface tension, leading to the breaking of the jet [54]. Moreover, excessively

high viscosities and concentrations will result in the production of thicker fibers, often taking a ribbon-like form [58]. This can potentially lead to challenges in ejecting the jet from the spinneret, causing interruptions in the process [47]. To achieve smooth fibers, it is essential to operate within the appropriate range of these parameters [59] (see Figure 1.10).

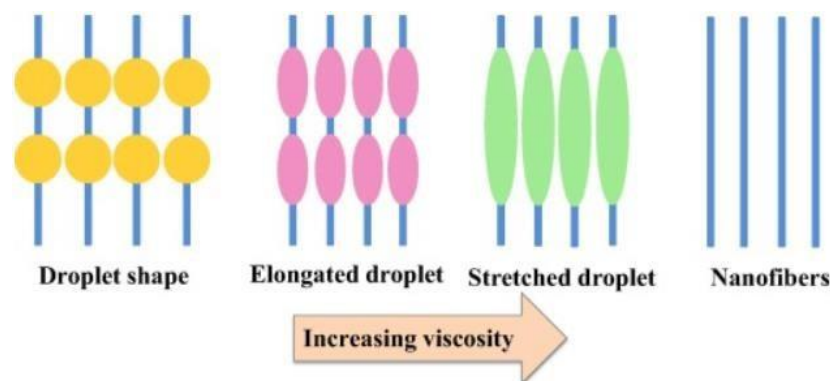


Figure 1. 9 - Effect of viscosity on fibres geometry: for low values of this parameter, defected fibres are created [60].

Interfacial tension and conductivity, represent supplementary solution factors that exert substantial influence on the electrospinning procedure's consequences. Reduced interfacial tension eases electrospinning at a reduced electrical potential and guards against bead formation, while an escalation in interfacial tension leads to the generation of droplets and instability in jet formation [47]. A higher value of conductivity is associated with fiber diameter reduction, whereas excessively low conductivity does not provide enough electrical force to elongate the jet, leading to the formation of beads [47].

Moreover, the selection of the solvent assumes a crucial role in these aspects. Opting for the right solvent or a combination of solvents necessitates considering its capacity to dissolve the polymer at the intended concentration and its effects on electrical conductance, consistency, and interfacial tension [54].

➤ **Process Parameters:**

The voltage that we applied, stands as a critical variable; it must surpass a certain threshold to initiate the process and lead to the formation of the Taylor cone [47] [61]. This threshold is primarily contingent upon the properties of the solution being used [54]. As the voltage increases, it leads to an alteration in the initial jet's shape, which subsequently affects the shape of the fibers [50] (see Figure 1.11). An elevation in voltage intensifies the whipping

instabilities, resulting in a reduction in fiber diameter due to jet elongation. Conversely, excessively high voltage values can give rise to the formation of beaded nanofibers and potential jet fragmentation into multiple jets [60] [54].

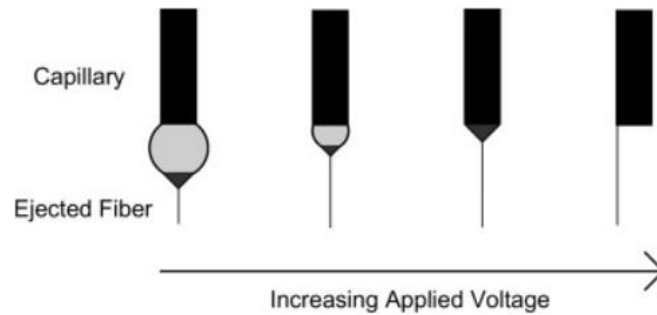


*Figure 1. 10 - Changes in the shape of the Initializing Jet as the applied voltage increases [62].*

The flow rate of the solution dispensed from the needle is crucial to ensure prompt replacement of the spun material, maintaining the continuity of the Taylor cone. However, it should not be excessively high to allow for complete solvent evaporation during the process [61] [47]. Failure to achieve this can result in the production of thicker fibers with beads and wrinkles [54].

The distance between the tip of the needle and the collector is another parameter of consideration. This element impacts the duration of deposition, the speed of solvent evaporation, and the attributes of jet instabilities, ultimately giving rise to variations in fiber composition and diameter [50] [47]. An intermediate spacing is often the most favorable; when the needle and collector are either too close or too distant, the formation of beads has been observed [47].

The electrospun base material can assume either a flat or cylindrical configuration, with fibers being either haphazardly dispersed or aligned, contingent upon the type of collector utilized.

Common collector designs are depicted in Figure 1.12

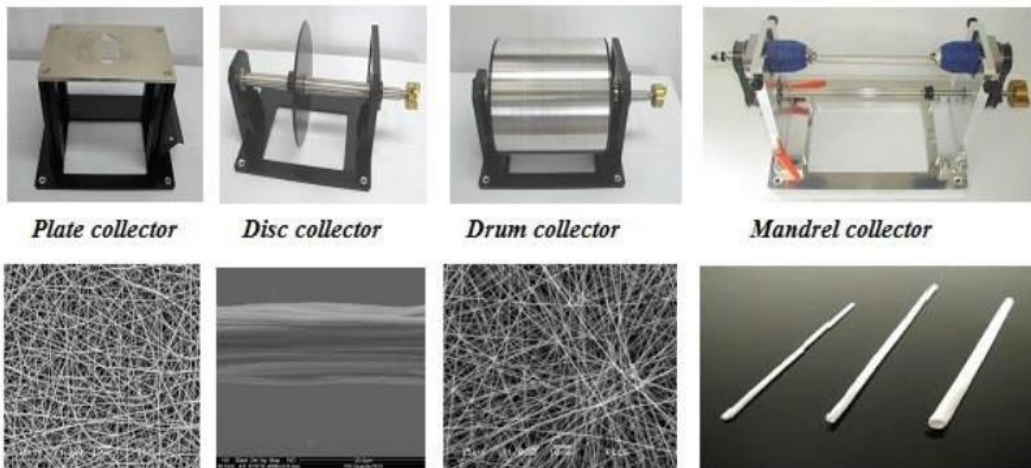


Figure 1.12 Most common collectors and the corresponding fibres [63].

➤ **Environmental Parameters:**

Environmental conditions, particularly temperature and moisture levels, constitute crucial considerations. Humidity influences the rate of solvent evaporation, with increased humidity causing a retardation in solvent evaporation, affording more time for fibers to elongate and attain a reduced diameter. Nonetheless, exceedingly elevated humidity levels (>60%) can lead to fibers cohering and failing to deposit as distinct entities [54]. When temperature increases, fibers become thinner, and this is due to enhanced electrical conductivity and reduced viscosity, because they have an inverse relationship [58] [59] [54]. Conversely, higher temperatures accelerate solvent evaporation, resulting in a faster fiber deposition process and reduced elongation [54].

#### 1.4.3 Materials for the electrospinning: Polycaprolactone

Biomaterials utilized in this field, must adhere to several essential criteria. Firstly, they should be biodegradable, biocompatible and bioresorbable to minimize inflammation and prevent the foreign body reaction. Additionally, the degradation products should be metabolized at a controlled rate to keep them within tolerable levels [64]. Finally, these biomaterials must establish a conducive milieu for the effective development of fresh tissue and provide sturdy mechanical reinforcement during the regeneration stage [64].

Numerous polymers have been effectively processed using the electrospinning technique [65], encompassing natural, synthetic, or blended polymers. Among the most commonly utilized ones are poly-( $\epsilon$ -caprolactone) (PCL), poly-(lactic-co-glycolic acid) (PLGA), poly-(lactic acid) (PLA), poly-( $\epsilon$ -caprolactone) (PCL), poly-(glycolic acid) (PGA), polyvinyl alcohol (PVA), poly-(ethylene oxide) (PEO), poly-(ethylene glycol) (PEG), alginate, chitosan, elastin, collagen and gelatin [66].

In this thesis work, PCL was employed to create the electrospun membranes. Polycaprolactone is a synthetic semi-crystalline polyester polymer, synthesized through the ring-opening polymerization of  $\epsilon$ -caprolactone [67]. It finds wide application in biomedical contexts. The chemical structure of PCL is depicted in Figure 1.13.

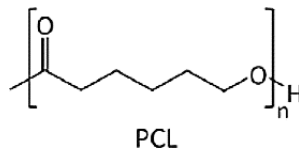


Figure 1.13 Chemical structure of PCL [68].

This is a biodegradable polymer, and the degradation process can vary in duration, ranging from months to years. The rate of degradation depends on factors such as the degree of crystallinity, molecular weight, and environmental conditions. The primary mode of degradation is hydrolytic, but it can also occur through the action of microorganisms [67]. Additional noteworthy properties of PCL include its hydrophobic nature and a low melting temperature that makes it highly processable, as discussed in reference [69]. Furthermore, PCL exhibits a rubbery state at body temperature, which contributes to its excellent mechanical properties, encompassing toughness, strength, and elasticity, as detailed in references [70] and [71].

#### 1.4.4 Electrospinning applied to biomedical applications

Electrospinning has a broad spectrum of applications within the field of bioengineering, with the most common being drug delivery, tissue engineering, and enzyme immobilization [60].

In tissue engineering, electrospinning is a versatile technique for producing scaffolds applicable to various regenerative purposes such as bone, cardiovascular, nerve, and skin regeneration [72]. Notably, electrospun membranes designed for wound healing applications offer numerous advantages.

Nanofibrous meshes, owing to their non-woven structure, random alignment, and nanoscale diameter, are highly effective in replicating the structure and function of the extracellular matrix (ECM). The ECM represents the acellular component of tissues that envelops and provides support to cells, guiding their growth and migration. It also plays a pivotal role in repair mechanisms [73].

The high surface area facilitates an ideal environment for cell attachment, growth, and differentiation [61]. Additionally, it permits the inclusion of biomolecules or therapeutic agents [61]. Furthermore, the high porosity, along with well-distributed and appropriately sized pores, grants the membrane excellent absorption capacity and enables gas exchange while preventing the ingress of bacteria and contaminants [61]. These characteristics are shown in figure 1.14.

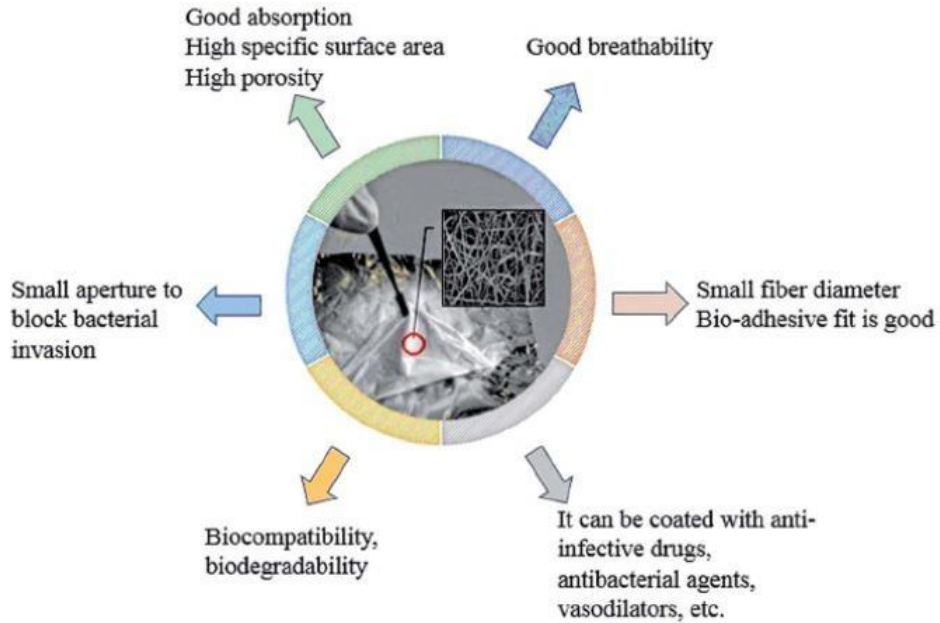


Figure 1.14 Properties of electrospun membranes for application in wound dressings [61].

PCL-electrospun membranes necessitate an additional step of surface functionalization (to attain the necessary biocompatibility and antibacterial properties required for wound healing applications) that plays a pivotal role in the field of biomedicine as it allows for the alteration of the physicochemical, morphological, and biological properties, as well as the chemical composition of substrates to achieve the desired characteristics for a specific application [72] [73]. These modifications can entail improved biocompatibility, diminished immunological reactions, and the capacity for localized drug administration, among various attributes [74]. Standard techniques utilized for surface enhancement encompass covalent grafting, streptavidin/biotin adhesion, and non-covalent bonding approaches, such as the layer-by-layer process.

## 1.5 Layer by layer assembly as a coating technique

The layer-by-layer (LbL) technique is a coating method utilized for the functionalization of substrates. It relies on the electrostatic interaction between layers with opposite charges, a process also known as electrostatic self-assembly (ESA) [74]. Layer-by-Layer (LbL) technology enables the creation of nanometer-scale coatings with customized characteristics and is adaptable to a variety of substrate materials, such as membranes and fibers, among others. It offers the capability to incorporate a diverse array of compounds [75], encompassing both small and large molecules, along with organic and inorganic materials [76], such as polymers, proteins, lipids, nucleic acids, nanoparticles, metal oxides, and more [77] [78] (as depicted in Figure 1.15).

The most important advantages of the Layer by Layer technique are:

- The ability to precisely control the properties of the coating [79]
- the characteristics of the substrate remain unaffected by the thickness of the coating [78];"
- the mild conditions of the process, which allow to maintain intact the properties of the biomolecules incorporated [76];
- the low cost and environmental-friendly process [79].

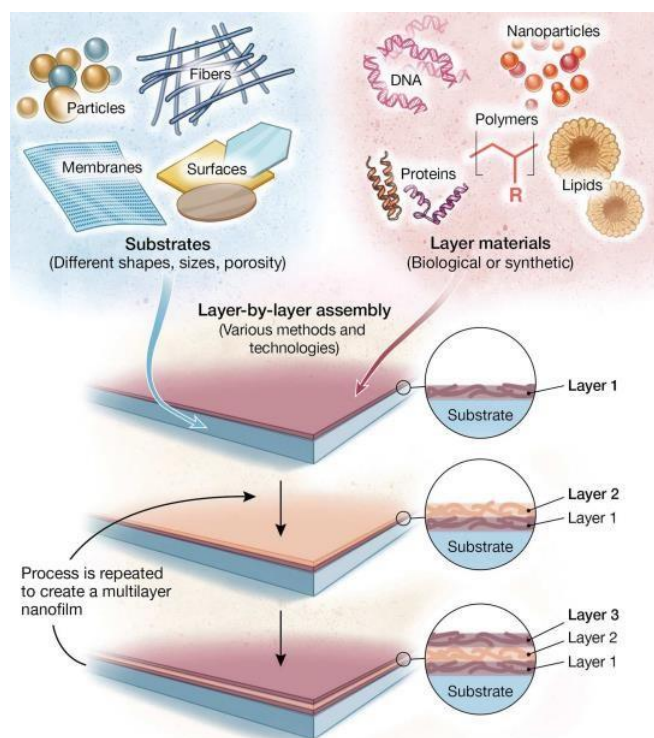


**Figure 1.15** Schematic representation of the assembled coating onto the substrate.

*Different types of substrates and coating materials are also shown [78].*

The procedure involves depositing a charged material onto a substrate that has been pre-modified to have a surface charge. Subsequently, after a washing step, a compound with an opposite charge is deposited on top of the initial layer. This results in the formation of the initial bilayer with a nanometric thickness. The process can be iterated in cycles to build a multilayer coating of the desired thickness [78]. It's possible to incorporate more than two components in the layers; the primary guideline is to ensure an appropriate alternation of positive and negative charges [80]. While electrostatic interactions are the primary driving force in the LbL technique, other types of interactions may also participate in the process, such as hydrogen bonds, van der Waals forces, covalent bonds, host-guest interactions, and biospecific interactions [81] [75] [82].

Various assembly strategies have been employed for the LbL technique, including immersive, spin, spray, electromagnetic, and fluidic methods (see Figure 1.16).

The most utilized method is the immersive (dip) assembly technique. This approach involves the manual dipping of the flat substrate into both cationic and anionic solutions of the desired materials, with intermittent washing steps (using water or a buffer solution) to eliminate excess material and prevent cross-contamination of the solutions, as described in references [78], [81], and [83]. Now, let's consider a hypothetical scenario where the substrate carries a negative charge. When it is immersed in a cationic solution, polycationic molecules are introduced through a diffusion mechanism in the solution, and when they come in close proximity, they are attracted by the electric field generated by the surface. This process completely covers the surface with a new layer of molecules, reversing the surface's polarity to become positive. At this point, the sample can be used to attract negatively charged molecules [74]. The immersive assembly technique can also be utilized for covering particulate substrates. However, in this scenario, centrifugation steps must be incorporated after each phase to gather the sediment [78]. This approach is favored when a uniform coating is essential, especially for attaining thin layers, in contrast to other non-LbL methods. The primary constraints pertain to the deposition time, which relies on the diffusion kinetics within the solution, and the manual character of the procedure [78]. However, some automated devices have emerged recently, such as the one developed at Newcastle University for automated dipping and spray deposition. The immersive technique leads to an interpenetrated layer structure, while the subsequent techniques generate a stratified structure with more distinct layers [78].

The spin assembly involves applying the coating onto a rotating substrate. Films that are more uniform, smooth, and thinner can be achieved with the assistance of other forces within the process, such as centrifugal force, viscous forces, air shear force, and more [78] [81]. Nevertheless, this technique has a significant limitation, as it can only be used to coat flat substrates [78].

The spray assembly method involves a two-step process: first, nebulizing the solutions, and then spraying them onto the substrate, as outlined in references [81] and [78]. It is a very fast process; One drawback of this method is the potential for creating a non-uniform coating, which can be attributed to the influence of gravity draining. This issue can be partially mitigated by employing rotating systems, where a higher quantity of coating is deposited onto the surface, resulting in increased uniformity, as discussed in reference [78].

Electromagnetic assembly, also known as electrodeposition, capitalizes on the application of electric or magnetic fields to create layers [78]. The basic setup involves two electrodes submerged in a solution. An electric field is employed between these electrodes to facilitate the deposition of the first layer. Subsequently, a rinsing phase is executed, followed by the immersion of the electrodes in a solution with an opposing charge, and a voltage is applied with an inverted polarity [78]. An alternative setup entails the insertion of a substrate between the two electrodes [78]. The thickness of the deposited layer hinges on the voltage administered; nonetheless, it is recommended not to escalate it excessively, as this can lead to repulsion from the preceding layer [78]. This approach necessitates specialized apparatus and adept operators, and it is neither more economical nor swifter when juxtaposed with other assembly techniques [81].

Fluidic assembly utilizes fluidic channels to generate the layers. This method permits the coating of either the channels themselves or a substrate positioned within them. The driving forces employed are pressure and vacuum, which are used to transport the solutions and carry out washing processes through the channels. The setup and equipment can be intricate, but the advantages include the ability to produce multilayer coatings on surfaces that are challenging to access with other techniques, along with the provision of new

methods for region-specific patterning [78].

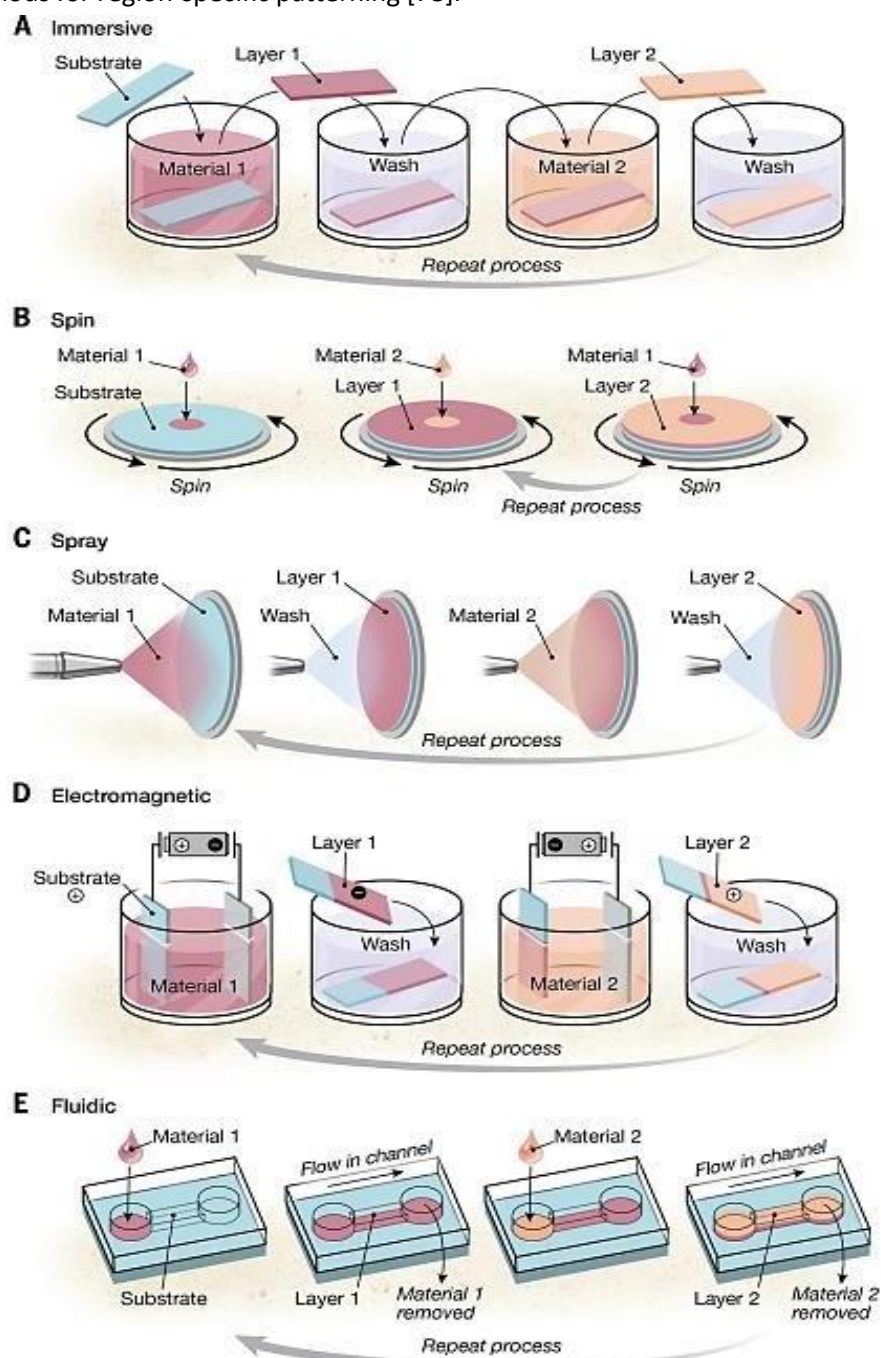


Figure 1.16 Schematic representation of the LbL assembly techniques: A) immersive, B) spin, C) spray, D) electromagnetic and E) fluidic [81].

### 1.5.1 Layer by Layer for biomedical applications

Layer by Layer functionalization has found applications in various sectors, spanning energy, optics, catalysis, and biomedicine [78]. This section will specifically address its biomedical applications, encompassing areas such as implanted devices, tissue engineering, and drug delivery.

#### ➤ **Implanted Devices**

Surface modification of implanted devices using LbL assembly is a potent approach to enhance their biocompatibility. The surface charge and hydrophobicity of the material play a critical role in regulating the adhesion of proteins and cells [85]. By customizing and modifying these properties, the desired outcomes can be achieved. For instance, one can enhance cell adhesion in the case of bone implants or deter it in cardiovascular stents. Additionally, therapeutics can be incorporated to prevent infections or enable the in-situ release of drugs.

*Cardiovascular implants* often lead to surface-induced thrombosis and in-stent restenosis, which can result in implant failure. To address these issues, one approach is to graft biomolecules onto the implant surface using the LbL technique [79]. For instance, Stainless Steel, a commonly used material for stent production but with low hemocompatibility, can be functionalized with layers of hyaluronic acid (HA) and heparin (HEP) loaded with Sirolimus (a drug). This approach allows for the development of a drug-eluting stent with anticoagulant properties [86] (see Figure 1.17 A).

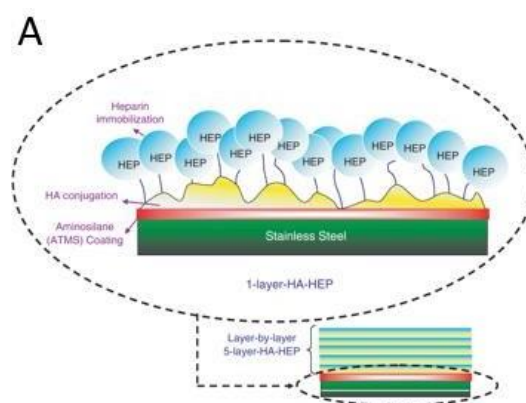


**Figure 1.17** Example of LbL coatings with application in Cardiovascular Implants [86].

## ➤ Tissue Engineering

To enhance bone regeneration using grafts, implantable materials engineered to stimulate bone healing and growth are commonly known as bone grafts. The Layer-by-Layer (LbL) technology can be employed to enhance the bioactive attributes of these materials [79], thereby amplifying the processes associated with osteogenesis, osteoinduction, and osteoconduction. As an illustration, consider a scenario in which a polycaprolactone/ $\beta$ -tricalcium phosphate (PCL/ $\beta$ -TCP) scaffold is introduced in rats to induce ectopic bone formation. In this instance, these scaffolds were coated with BMP-2 and VEGF, with the aim of fostering both bone formation and concurrent blood vessel development. Another variation of this study involved the incorporation of hydroxyapatite (HAP) and BMP-2 [90].

*Wound Healing Dressings* is the argument threaded in this thesis work.

## ➤ Drug Delivery

Drug delivery has ushered in a revolution in the treatment of various health conditions [82]. This innovation is primarily attributed to its ability to reduce therapeutic doses, achieve controlled release, target specific tissues, and surmount cellular barriers [79].

Various arrangements are viable: in the core-shell structure, Layer-by-Layer assembly can envelop a solid drug core (refer to figure 1.18) [91], or it can be assembled atop a nanoparticle, which is subsequently eliminated to form an empty core for drug insertion [79]. Alternatively, the cargo (therapeutic agents) can be incorporated into the layers through covalent attachments, adsorption, or in combination with a secondary carrier incorporated within the film [82].

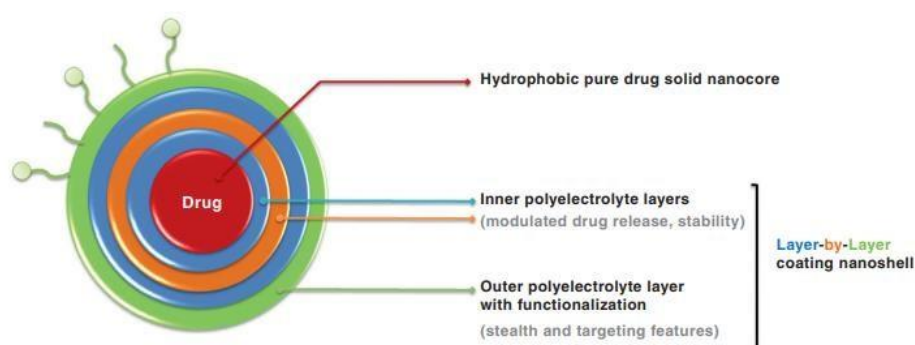


**Figure 1.18** Example of nanoparticle for drug delivery: drug solid core surrounded by the LbL coating [91].

Additionally, the cargo can be encapsulated either during or after the assembly process [82]. These layers not only encapsulate the cargo but also serve to provide stability, protect the drug from degradation, regulate its release, and aid in targeting [91].



## 1.6 Nanoemulsions

Nanoemulsions refer to emulsions with droplets in the sub-micron range, characterized by a mean droplet diameter of less than 500 nanometers [93]. In nanoemulsions, two immiscible liquids are blended and unified into a single phase, with the assistance of an emulsifying agent possessing amphiphilic properties, commonly known as a surfactant. This process is elaborated in references [93] and [94]. These coatings can be classified as 'oil in water' (O/W), 'water in oil' (W/O), or bi-continuous (W/O/W) compositions [93] [95] (refer to Figure 1.19). The selection of the formulation primarily hinges on the quantities of the components, with the one present in a larger volume serving as the outer continuous phase, while the other assumes the role of the inner dispersed phase [93].

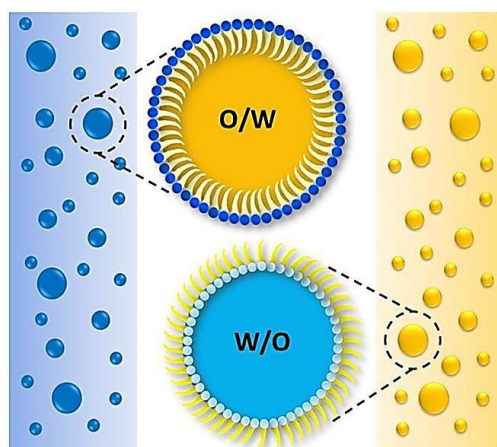


Figure 1.19 Schematic representation of oil-in-water and water-in-oil nanoemulsions [93].

Manufacturing techniques for nanoemulsions can be broadly classified into two primary categories: low-energy emulsification and high-energy emulsification [45] [93] [96]. Low-energy techniques encompass the phase-inversion method and spontaneous emulsification, while high-energy methods involve ultrasonication, high-pressure homogenization, and microfluidization [45] [93] [96]. Irrespective of the method employed, the primary objective is to produce droplets of the desired size with a monomodal distribution, ensuring uniformity in the properties of the nanoemulsion [93]. Best advantages of nanoemulsions, are [95] [96] [94]:

1. Enhanced bioavailability of therapeutic agents.
2. Increased surface area due to their small size, resulting in improved absorption.
3. Lower required doses, which can lead to reduced side effects.
4. Improved uptake in cell culture technology, facilitating toxicity studies on the nanoemulsions.

## 1.7 Antibacterial properties of natural compounds

Antimicrobial resistance (AMR) has become an increasingly challenging issue, prompting renewed interest in natural products known for their antibacterial and antimicrobial properties. In this study, chitosan, Manuka honey, and essential oils were investigated and utilized.

### 1.7.1 Chitosan

Chitin is a polysaccharide that is abundantly distributed in nature and can be extracted from the exoskeletons of insects and crustaceans, as indicated in reference [97]. Chitosan is derived from chitin through a deacetylation reaction using sodium hydroxide (NaOH) (see Figure 1.20). This process enhances the antibacterial properties of the material and its solubility in acidic environments [97].

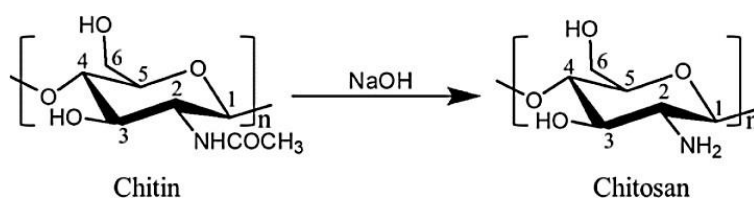
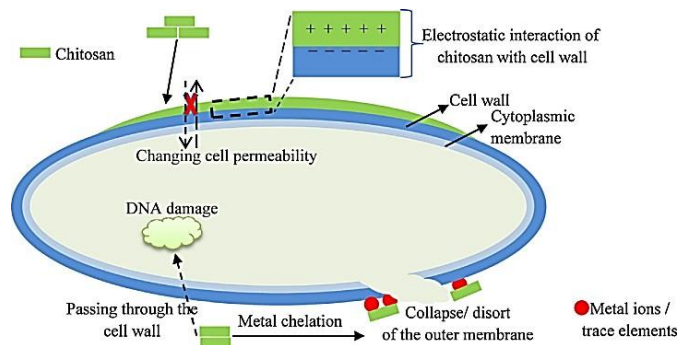


Figure 1.20 Structure of Chitin and Chitosan [97].

Chitosan is renowned for its antimicrobial properties, effectively targeting both gram-positive and gram-negative bacteria, as well as yeast and fungi [98] [97]. The effectiveness of these properties is subject to several influential factors, with the most critical ones including the degree of deacetylation (DD), pH levels, molecular weight, chitosan concentration, and the specific type of microorganism [97] [99]. The operating principle of antibacterial activity is illustrated in Figure 1.21. The positively charged chitosan, resulting from the protonation of amino groups and forming NH<sup>+</sup>, interacts with the negatively charged bacterial cell wall. This interaction compromises the integrity of the cell membrane, ultimately resulting in the leakage of intracellular substances. Furthermore, should the chitosan chains successfully penetrate the cell, they have the potential to interact with DNA, leading to a disruption of DNA expression and replication, ultimately culminating in cell death [97] [99] [100].



**Figure 1.21** Mechanism of action of Chitosan on bacteria cells [100].

Chitosan has a wide array of applications spanning various fields, including pharmaceuticals, food packaging, industry, textiles, chemicals, and, notably, the biomedical sector, as highlighted in reference [101]. Within the biomedical domain, chitosan is employed not only for its antibacterial properties but also for its biocompatibility, excellent biodegradability, non-toxic nature, and favorable physical and chemical characteristics, as discussed in reference [97].

### 1.7.2 Manuka Honey

Manuka honey (MH) is sourced from the manuka tree found in New Zealand and Australia [102] [103]. It is renowned for its antimicrobial, antifungal, antioxidant, and anticancer properties [104] [102]. Common compounds found in honey include vitamins, sugars, , enzymes, minerals, aminoacids, flavonoids, antioxidants and phenolic acids [104]. In non-Manuka honey varieties, the primary antimicrobial effect is attributed to hydrogen peroxide (H<sub>2</sub>O<sub>2</sub>). This effect is reinforced by factors such as high osmotic pressure, low pH levels, and the presence of immune-modulatory molecules like bee defensin-1, flavonoids, and phenolic complexes [102] [104] [105]. In contrast, Manuka Honey exhibits additional antibacterial properties, often referred to as 'non-peroxidase activity' (NPA). These properties persist even after the neutralization of hydrogen peroxide by catalase. The key contributor to these additional antibacterial properties is the compound methylglyoxal (MGO) (see Figure 1.22). This extra antibacterial activity is also denoted as the 'Unique Manuka Factor' (UMF) [104] [105].

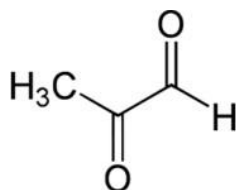


Figure 1.22 Chemical structure of methylglyoxal (MGO) [103].

Methylglyoxal (MGO) is produced through the non-enzymatic dehydration of dihydroxyacetone (DHA) [106], and its concentration in honey is associated with its antibacterial performance [102].

The antibacterial mechanisms of action of Manuka honey have been studied on both Gram-Positive bacterium *Staphylococcus Aureus* and Gram-Negative bacterium *Pseudomonas aeruginosa*. In the case of *S. aureus*, Manuka honey targets the later stages of cell division by inhibiting the activity of peptidoglycan (murein) hydrolase, which is responsible for the degradation of the septum between the two newly formed cells. This leads to impaired division and subsequent cell death [104] [107].

The mechanism is shown in figure 1.23.

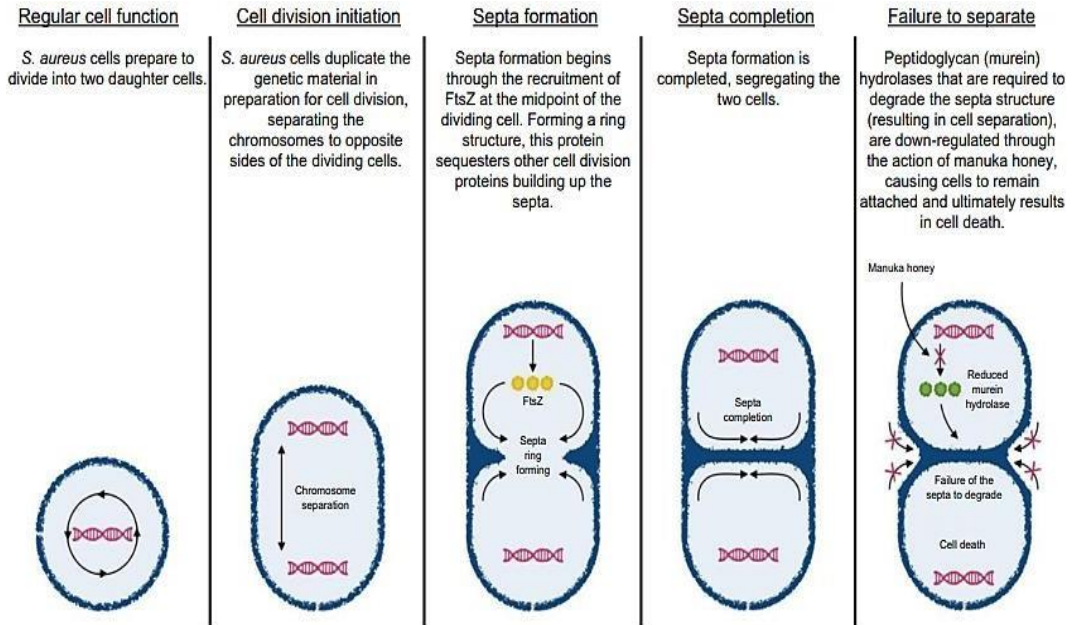


Figure 1.23 Mechanism of action of Manuka Honey against *Staphylococcus aureus* [104].

Manuka honey has demonstrated effectiveness against both Gram-Positive and Gram-Negative bacteria, including antibiotic-resistant strains and biofilms. Furthermore, no resistance to Manuka honey has been documented thus far [104] [109].

### 1.7.3 Essential Oils

Essential oils (EOs) are highly volatile natural compounds extracted from aromatic plants using various methods, including steam/hydro distillation, solvent extraction, or cold pressing, as detailed in references [110], [111], and [112]. Essential oils (EOs) find extensive application in various sectors, including pharmaceuticals, antiviral treatments, food preservation, and cosmetics. Their antibacterial, antidiabetic, and antioxidant properties make them particularly appealing for biomedical applications. EOs consist of a multitude of constituents with low molecular weight, including phenols, alcohols, oxides, aldehydes, ethers, esters, amines, ketones, amides, and predominantly phenylpropenes, terpenes, and terpenoids [111] [112] [113] [114].

Terpenes, which are hydrocarbons resulting from the bonding of multiple isoprene (C<sub>5</sub>H<sub>8</sub>) units in a head-to-tail fashion, can exhibit either linear or cyclic aromatic structures [114] [115]. The most prevalent terpenes include monoterpenes (C<sub>10</sub>H<sub>16</sub>) and sesquiterpenes (C<sub>15</sub>H<sub>24</sub>), exemplified by substances such as limonene, p-cymene, and terpinene. Terpenoids, on the other hand, are terpenes subject to alterations involving the introduction of oxygen molecules or the repositioning or elimination of methyl groups. Instances of terpenoids encompass thymol, linalool, and geraniol [112] [113] [114]. Phenylpropenes, characterized by a six-carbon aromatic phenol group and a three-carbon propene tail, are typified by eugenol, cinnamaldehyde, safrole, and vanillin [112] [114].

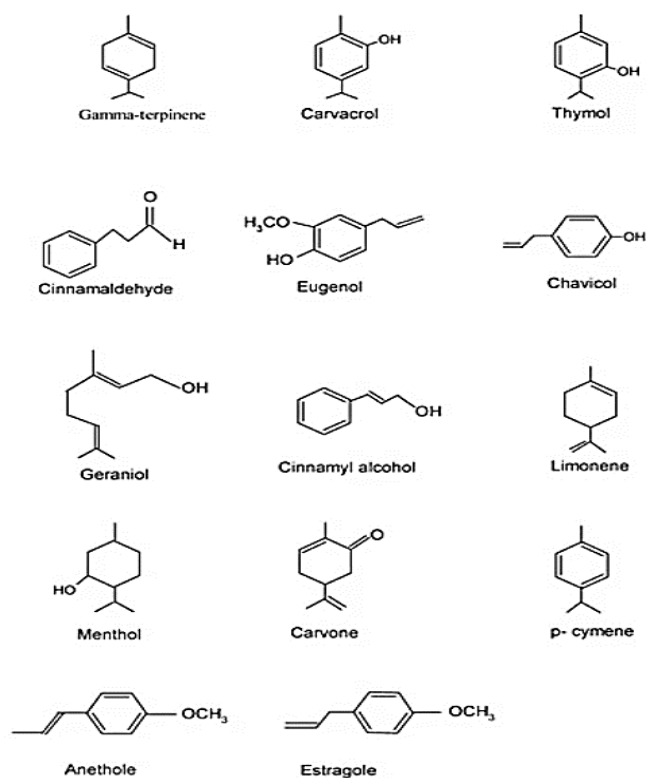


Figure 1.25 Compounds contained into Essential Oils possessing biological properties – Terpenes, Terpenoids and phenylpropenes [112].

These chemical compounds possess significant biological properties, with some of their effects being elucidated in Figure 1.25..

The antimicrobial activity of essential oils (EOs) is contingent upon their specific composition. Given the diverse array of constituents present in EOs, it is believed that EOs lack a singular cellular target, instead relying on multiple mechanisms that affect either the bacterial membrane or the cytoplasm, as discussed in references [111] and [114].

Due to their lipophilic nature, EOs have a propensity to bind to the bacterial cell membrane, resulting in several cytotoxic consequences. These include the disruption of the cell wall, which leads to the leakage of cellular contents, alterations in membrane transport, and impairments in energy production and control, as detailed in references [111], [113], and [114]. Additionally, events like cytoplasm coagulation and interference with quorum sensing activities occur, as highlighted in references [111], [113], and [114]. Collectively, these processes culminate in cell lysis and bacterial death, involving mechanisms such as apoptosis and necrosis, as depicted schematically in Figure 1.26.

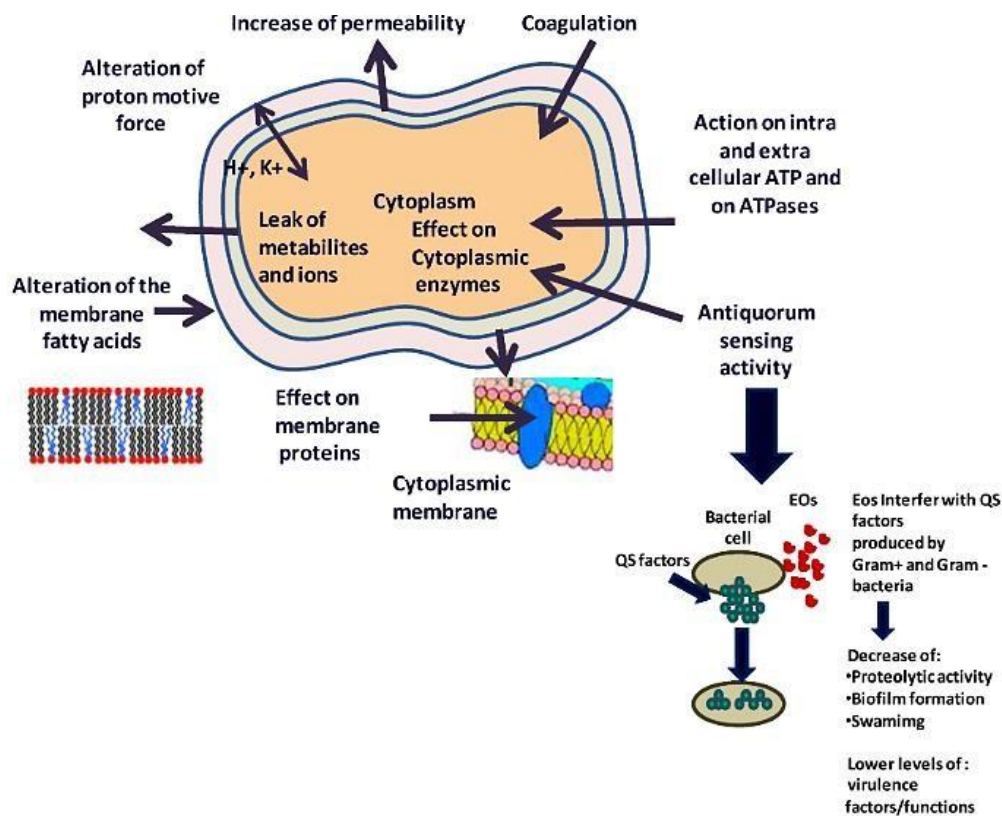


Figure 1.26 Effect of Essential Oils on bacteria cells [114].

The Food and Drug Administration (FDA) has classified the primary components found in essential oils as 'Generally Regarded as Safe' (GRAS) when used at low concentrations, signifying their safety for human health. However, it is essential to note that these components can exhibit toxic effects on eukaryotic cells when employed at high concentrations, potentially reaching lethal doses. Therefore, further research and investigation are required to comprehensively understand the toxicity profile of essential oils, as mentioned in reference [116].

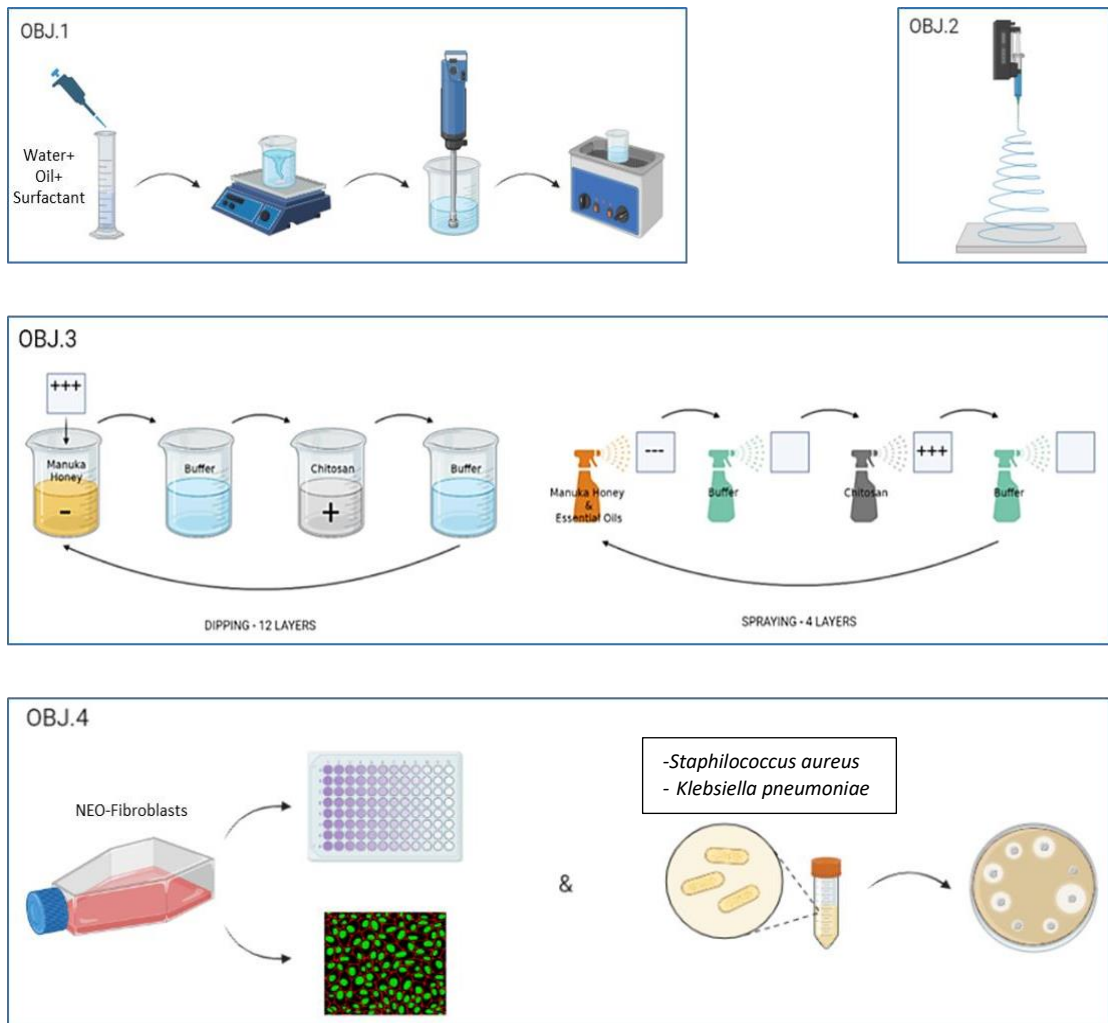


Figure 1.27 Main objectives of the thesis.

In this thesis work, Tea Tree essential oil (TTO) and Eucalyptus essential oil (EO) have been employed.

## 1.1 Aim of the work

The focus of this project revolves around creating antibacterial coatings through the layer-by-layer technique. The primary goal of this endeavor is to develop and produce membranes for wound healing applications that incorporate natural compounds, such as chitosan, manuka honey, and essential oils (tea tree oil and eucalyptus oil), with antibacterial properties. These membranes will be tested for their impact on fibroblast cells and various bacterial strains. The key objectives (OBJs) of the project are outlined in Figure 1.27 and include:

### **OBJ1. Nanoemulsions assembly:**

Nanoemulsions of essential oils have been obtained through sonication and through a specific machine it was investigated their  $\zeta$ -potential.

### **OBJ2. Membranes production:**

Through Electrospinning method, it was a random structure PCL, setting the machine on specific values, so as to optimize the process and obtain nanometric, homogeneous and defect-free fibres.

### **OBJ3. Layer-by-Layer Coating:**

Through LbL functionalization, it was obtained membranes with a 14-layers coating. This process involved both dipping and spraying methods and incorporated natural compounds within the layers. The growth of these layers, was confirmed using various techniques, including SEM and FTIR-ATM analysis (conducted at Newcastle University) and XPS analysis.

### **OBJ4. Biological evaluation:**

Cellular tests were conducted using Neo-Fibroblast cells to assess cell viability and metabolic activity when in direct contact with the membranes. Various assays like PrestoBlue®, Live/Dead was employed for these evaluations. Additionally, bacterial tests were performed on strains of *Klasiella Pneumonia* and *Staphylococcus aureus* to assess the antibacterial activity of the membranes.

## Chapter 2: Materials and Methods

### 2.1 Materials

Tea Tree Oil (TTO) and Eucalyptus Oil (EEO), Tween80 (Sigma Aldrich) and distilled water were used for the nanoemulsions. Polycaprolactone (Medium Mw 80kDa, Sigma Aldrich), Acetic Acid Glacial (Sigma Aldrich), Formic Acid  $\geq 95\%$  (Sigma Aldrich) were used for the electrospinning, while the hexamethylenediamine 98% (Sigma Aldrich) and distilled water were used for the aminolysis solution. Manuka Honey (MG 550+, Manuka Health), Chitosan (Mw 50 kDa, Sigma Aldrich), Sodium Acetate (Sigma Aldrich), Acetic Acid Glacial (Sigma Aldrich) were used for the polyelectrolyte solutions for the Layer-by-Layer assembly.

In the experimental procedures, Neo-Fibroblasts were cultivated using Dulbecco's Modified Eagle Medium (supplied by Gibco, a division of Thermo Fisher), supplemented with Fetal Bovine Serum, L-glutamine, and Penicillin-Streptomycin. In addition, various reagents and kits were employed for cell culture and testing purposes, including the Live/Dead<sup>®</sup> Cell Double Staining Kit (provided by Sigma Aldrich), Sudan Black (also from Sigma Aldrich), PrestoBlue<sup>®</sup> (from Invitrogen, a division of Thermo Fisher Scientific), DAPI (4',6-diamidino-2-phenylindole ActinRed<sup>™</sup> obtained from Sigma Aldrich). The cells were preserved in a phosphate-buffered saline (PBS) solution (provided by Sigma Aldrich), and fixation was accomplished using a 4% Paraformaldehyde solution (manufactured by Thermo Fisher Scientific).

For the bacterial cultivation and testing procedures, Staphylococcus aureus NCTC 6571 and Klebsiella Pneumonia strains were employed, along with PBS, Lugol's Iodine, Safranin, Nutrient broth, BHYE broth, Nutrient Broth Powder (supplied by Sigma Aldrich), Tryptic Soy Broth Powder (also provided by Sigma Aldrich), and Agar powder (likewise sourced from Sigma Aldrich).

### 2.2 Manufacturing Methods

#### 2.2.1 Preparation of nanoemulsions

The oil-in-water emulsions were created following the procedure outlined in the study by Zhang and colleagues [117], the essential oils (TTO and EO) were mixed at specific weight ratios (expressed as a percentage by weight) with the surfactant Tween80, with a corresponding ratio of 66.7% Tween80 to Essential Oil. This mixture was

then added to distilled water to achieve the desired final volume. The solutions were stirred at 600 rpm for a duration of 12 minutes using an IKA magnetic hotplate. Subsequently, they underwent a homogenization phase using an IKA® T25 digital ULTRA-TURRAX® homogenizer for 10 minutes. Lastly, the solutions were sonicated in an ultrasonic bath operating at 140W and 50kHz (Labsonic, FALC Instruments). The entire procedure is illustrated in Figure 2.1.

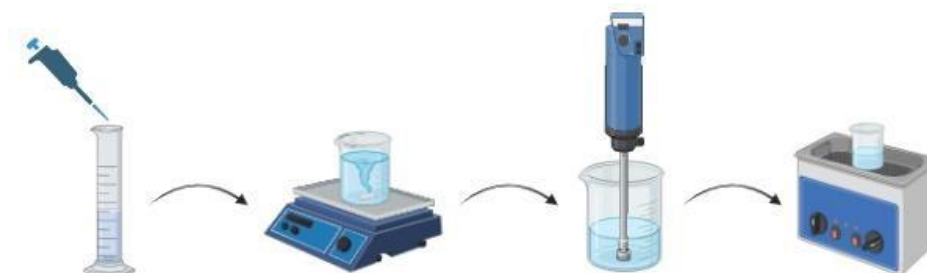


**Figure 2.1** Sequential procedure for the formulation of nanoemulsions involves: blending water, oil, and surfactant; agitating the mixture; subjecting it to homogenization; and applying sonication.

#### Manufacture of electrospun membranes

The membranes were fabricated using the electrospinning technique (Section 1.4). Initially, PCL pellets were dissolved in a mixture of acetic acid and formic acid (in a 1:1 volume ratio), and the solution was stirred overnight at 300 rpm on an IKA magnetic hotplate. The resulting PCL solution was processed using an electrospinning apparatus (Spinbox, Bioinicia, Spain) to produce porous membranes composed of nanoscale fibers.

To optimize the process, a series of trials were conducted. Various processing parameters were explored to achieve the thinnest possible fibers (measuring in the range of a few hundred nanometers) without defects like beads or ribbons. Fiber quality was assessed via scanning electron microscopy (SEM), with detailed characterization methods described later. Fiber diameter measurements were performed using ImageJ software.

The parameters subjected to testing included polymer concentration (15%, 17.5%, and 20%), needle-to-collector distance (10 cm, 12 cm, and 14 cm), flow rate (400  $\mu$ l/h, 600  $\mu$ l/h, and 800  $\mu$ l/h), and voltage (14 kV, 16 kV, and 20 kV).

#### 2.2.2 Aminolysis of the membranes

The membranes underwent aminolysis as a preparatory step for the subsequent layer-by-layer functionalization process. This step was essential to introduce a positive surface

charge through NH<sub>2</sub> groups. The aminolysis procedure was carried out following the method described by Mancuso et al. [118]. A solution of ED (0.06 g/ml) in distilled water was prepared and then applied to the membranes for 10 minutes. The membranes were subsequently thoroughly rinsed with distilled water.

### 2.2.3 Coating of the membranes – Layer by Layer technique

The layer-by-layer (LbL) functionalization of the membranes was performed using an automatic device developed at Newcastle University (WO 2021079106A1), which combined both the Dipping and Spray modalities. The process involved alternating the immersion of the membranes in polyelectrolyte solutions with subsequent washing steps. Here's a step-by-step description of the LbL process:

Preparation of Polyelectrolyte Solutions:

Manuka Honey (MH) solution: MH was dissolved in a sodium acetate buffer at a concentration of 20% w/v.

Chitosan solution: Chitosan was dissolved in a sodium acetate buffer at a concentration of 1% w/v.

Initial Dipping Process: The membranes were initially dipped into the MH solution for 10 minutes. MH served as the polyanion and interacted with the positively charged surface of the membranes created during aminolysis.

After the dipping step, the membranes were washed with the sodium acetate buffer for 5 minutes.

Alternating Dipping Process: The next step involved dipping the membranes into the chitosan solution for 10 minutes. Chitosan served as the polycation.

Following this, the membranes were washed again with the sodium acetate buffer for 5 minutes.

Steps 2 and 3 were repeated six times to create a total of 12 layers on the membranes.

Spray Modality for Additional Layers: After the initial 12 layers were deposited, an additional four layers were added using the spray modality.

The nano-emulsions of essential oils (EOs) were prepared according to optimized parameters and adjusted to pH 5.

The EO-MH solution, with a negative charge, was used as the polyanion in this step.

Chitosan remained the polycation.

The polyelectrolytes (EO-MH and chitosan) were sprayed onto the membranes for 18 seconds.

Subsequently, a washing solution was sprayed onto the membranes for 6 seconds.

This layering process, combining dipping and spraying modalities and incorporating EO nanoemulsions, is schematically illustrated in figure 2.2.

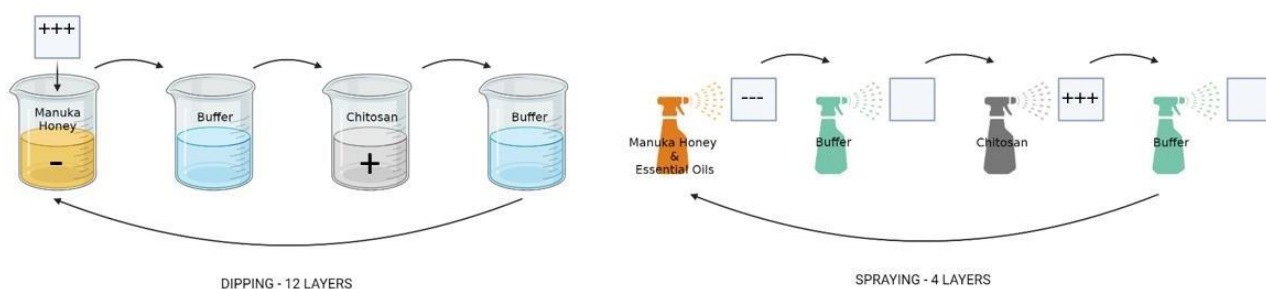


**Figure 2.2** Dipping and Spray modality in layer by layer

Upon completion of the process, the membranes were coated with 14 layers, resulting in a coating of nanometric scale thickness. Following the coating, the membranes were allowed to air-dry overnight and were subsequently stored at a temperature of 4°C before further use.

## 2.3 Characterization methods

### 2.3.1 Nanoemulsions

#### 2.3.1.1 *Dynamic Light Scattering and Zeta-Potential*

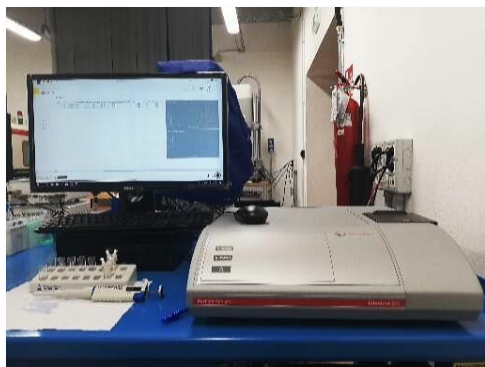


**Figure 2.3** DLS Litesizer 500 device.

Particle size and zeta-potential analyses were carried out using the Anton Paar Litesizer 500 instrument (please see Figure 2.3 for reference). The measurements were executed in 1 mL cuvettes for particle size evaluation and omega cuvettes for zeta-potential assessment. The specified parameters encompassed a 120-second equilibration duration, 15 runs conducted at room temperature (25°C), and a scattering angle of 173°. To guarantee precision and uniformity, each measurement was repeated three times. *Transmission Electron Microscopy (TEM)*

The morphology of the nanoemulsions was examined using transmission electron microscopy (TEM). Here's a description of the TEM sample preparation and imaging parameters:

#### Sample Preparation:

A small drop of the nanoemulsion solutions was placed onto a copper grid.

Excess liquid was carefully removed using a filter paper to leave a thin film of the sample on the grid.

#### TEM Instrumentation:

The prepared samples were observed using a Philips CM 100 Compustage FEI transmission

electron microscope.

The microscope was operated at a high voltage (HV) of 100.0 kV.

Imaging:

Digital images of the samples were captured using an AMT CCD camera (Deben) attached to the TEM.

The camera allowed for a range of magnifications, with the capability to achieve magnifications of up to 130,000x.

This TEM analysis allowed for the visualization and examination of the nanoemulsion's morphology at high magnification, providing insights into the structure and characteristics of the emulsions.

## 2.3.2 Membranes

### 2.3.2.1 Scansion Electron Microscopy (SEM)

The Scanning Electron Microscope (SEM) was utilized in two main aspects of your study:

#### 1. Optimization of Electrospinning Process:

SEM was employed to optimize the electrospinning process by evaluating parameters such as fiber diameters and the presence of structural defects.

The analysis was conducted using a Scanning Electron Microscope, specifically the Jeol JSM-5600LV model (refer to figure 2.4).

#### 2. Coating Presence and Thickness Assessment:

SEM was also employed to determine the presence and thickness of coatings on the membranes.

Sample preparation involved cutting the membranes into square pieces measuring 5x5 mm<sup>2</sup>.

These samples were then affixed to carbon conductive tabs and secured on pin stabs.

Before SEM analysis, the samples underwent a gold sputter coating process using the Sputter Coater from BIO-RAD Microscience Division.

SEM analysis was performed using an electron beam voltage of 20kV, a working distance of 20mm, a spot size of 24 n° units, and various magnification levels.

The acquired SEM images were subsequently analyzed using ImageJ software.

In summary, SEM analysis played a crucial role in optimizing the electrospinning process and assessing the presence, as well as the thickness, of coatings on the membranes. This provided valuable data on fiber diameters, structural defects, and the quality of the applied coatings.



Figure 2.4 SEM machine

#### 2.3.2.2 Methylglyoxal (MG) Assay Test

Since we are interested in knowing how much methylglyoxal is released from our membranes when it is immersed in a physiologic-like solution, we went about doing this from an absorbance test, the methylglyoxal assay kit (ab241006) that enables the detection of MG, using a set of engineered enzymes and a chromophore, the final product of the assay, that can produce a stable signal, which can be easily quantified at 450 nm, using a microplate reader and its signal is directly proportional to the amount of MG in samples.

The assay is simple, specific, reproducible, and can detect as low as 0.5 nmol/well of MG in a 100  $\mu$ L reaction.

Material supplied, and Storage and stability:

Is stored the kit at  $-20^{\circ}\text{C}$  in the dark, and aliquot components in working volumes before storing at the recommended temperature.

Briefly centrifugate small vials prior to opening.

<b>Item</b>	<b>Quantity</b>	<b>Storage condition</b>
MG Assay Buffer	25 mL	4°C or -20°C
Substrate Mix A 1 vial -20°C	1 vial	-20°C
Substrate Mix B 1 vial -20°C	1 vial	-20°C
Enzyme Mix A 22 µL -20°C	22 µL	-20°C
Enzyme Mix B 120 µL -20°C	120 µL	-20°C
Enzyme Mix C 1vial -20°C	1 vial	-20°C

Material required but not supplied:

- Microplate reader capable of absorbance measurement
- 96-well clear plate with flat bottom
- Distilled or deionized water
- Syringe filter: pore size 0.22µm

Reagent Preparation:

Before using the kit, spin tubes and bring down all components to the bottom of tubes. Prepare only as much reagent as is needed on the day of the experiment.

**MG Assay Buffer:**

Store at either 4 °C or -20 °C. Bring to room temperature before use.

**Substrate Mix A:**

Reconstitute in 65 µL dH<sub>2</sub>O, store at -20 °C. Use within two months.

**Substrate Mix B:**

Reconstitute with 220 µL of MG Assay Buffer and mix thoroughly. Store at -20 °C.

**Enzyme Mix A:**

Ready for use, store at -20 °C, use on ice.

**Enzyme Mix B:**

Ready for use, store at -20 °C, use on ice.

**Enzyme Mix C:**

Dissolve in 220 µL MG Assay Buffer. Pipette up and down to completely dissolve.

### Sample Preparation:

For liquid samples (Manuka Honey):

Manuka Honey (weight: ~200-500 mg) in a centrifuge tube, dilute samples 1:10 (v/v) in dH<sub>2</sub>O, mix well.

- Centrifuge samples at 10,000 x g at room temperature for 10 min. Collect the supernatant and filter through 0.22 µM filter.
- Dilute supernatant samples (1:2 to 1:10), if necessary, using dH<sub>2</sub>O.
- Sample(s): Add 2-20 µL of (diluted) samples onto desired well(s) in a clear 96-well plate.
- Sample Background Control: Prepare duplicate sample well(s). Adjust the volume of Sample(s) and Sample Background Controls to 20 µL/well with dH<sub>2</sub>O.

### Assay Procedure

- Prepare a 10-fold Dilution of Substrate Mix A (i.e. Dilute 2 µL of Substrate Mix A stock solution with 18 µL MG Assay Buffer), mix well and keep on ice.
- Prepare a 10-fold Dilution of Enzyme Mix A (i.e. Dilute 2 µL of Enzyme Mix A stock solution with 18 µL MG Assay Buffer), mix well and keep on ice.
- Mix enough reagents for the number of assays to be performed. For each well, prepare a total 80 µL Mix containing the following components. Mix well before use:

	Reaction Mix	Background Mix
MG Assay Buffer	67 µL	69 µL
Diluted Substrate Mix A	6 µL	6 µL
Diluted Enzyme Mix A	2 µL	
Enzyme Mix B	1 µL	1 µL
Enzyme Mix C	2 µL	2 µL
Substrate Mix B	2 µL	2 µL

- Add 80 µL of the Reaction Mix to each well containing the MG Standard(s), Sample(s); Add 80 µL of Background Mix to well(s) containing Sample Background Control.
- Measurement: Measure absorbance at 450 nm in end-point mode.

Sample preparation :

Six different types of samples were tested, for each of which three squares of membrane, measuring 1cm x 1cm, were cut out and put it into an Eppendorf, with 500  $\mu$ L of PBS not sterile.

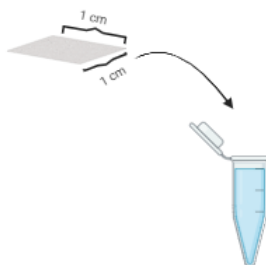


Figure 2.5 - 1 x 1 membrane insert in an Eppendorf with with 500  $\mu$ L of PBS not sterile

All samples were placed in an incubator at 37°C.

Once the various time points have been chosen, an amount of PBS, in which the membrane will have released MGO, equal to 20  $\mu$ L, will be taken for each of them and placed in a 96-well plate and then, will be refilled with non-sterile PBS, of the same amount taken and placed to rest in the incubator.

The chose timepoint are: 60 min, 2h, 8h, 24h and 7 days, while the chosen different type of membranes are:

8L MH, 10L MH, 8L MH + 4L TT, 10L MH + 4L TT, 8L MH + 4L EU, 10L MH + 4L EU.

#### 2.3.2.2 *Fourier Transformed Infrared Spectroscopy with attenuated total reflectance (FTIR-ATR)*

To examine the surface functional groups of the samples and identify variations resulting from the presence of essential oils, FTIR-ATR analysis was performed. The measurements were carried out using a Spectrum Two PE instrument, which was equipped with a horizontal attenuated total reflectance (ATR) diamond crystal, manufactured by PerkinElmer Inc. (USA). Data acquisition was conducted in Absorbance mode, spanning wavenumber values from 4000  $\text{cm}^{-1}$  to 550  $\text{cm}^{-1}$ .

#### 2.3.2.3 *X-Ray photoelectron spectroscopy (XPS)*

X-ray photoelectron spectroscopy (XPS) is a quantitative analytical technique that enables the measurement of the elemental composition on the surface of a material and facilitates the determination of binding states between specific elements, such as carbon (C), nitrogen (N), and oxygen (O). The examination of the samples was conducted using a scanning microprobe Kratos Axis Ultra-DLD XPS spectrometer, which was located at the

EPSRC Harwell XPS Service in Cardiff, UK. This spectrometer was equipped with a monochromatized AlK $\alpha$  X-ray radiation source, ensuring precise analysis. The base pressure within the analysis chamber was maintained at 10<sup>-9</sup> mbar.

The analysis was performed in High Power mode with an X-ray take-off angle of 45°, covering a scanned area of approximately 1400 × 200  $\mu$ m. For each specimen, survey scans were carried out in Fixed Analyser Transmission mode, covering a binding energy (BE) range from 0 to 1200 eV, with a pass energy of 117.4 eV. Furthermore, high-resolution spectra were acquired for the C1s element in FAT mode with a pass energy of 29.35 eV.

To ascertain the atomic concentration (At.%) from the survey scans, the integrated CasaXPS software package was employed. Following this, to pinpoint the Binding Energy (BE) associated with the chemical bonding states of the elements present in the films, the XPS spectra derived from the films were subjected to peak deconvolution using the identical software.

## 2.4 Biological evaluation

### 2.4.1 Cellular Tests

Cell tests were conducted to evaluate the biocompatibility of the coated membranes. In passage 8 in Dulbecco's Modified Eagle Medium, were cultured up Neo-fibroblast with the addition of 1% v/v L-glutamine, 10% v/v Fetal Bovine Serum (FBS), and a 1% v/v mixture of Penicillin-Streptomycin.

All cell culture and tests, were conducted under sterile conditions, with cells maintained at 37°C in a controlled atmosphere with saturated humidity and 5% CO<sub>2</sub>.

The samples were prepared by securely affixing the membranes to the cell crown inserts, which were then placed within a 48-well plate. In preparation for the staining assays, the membranes were treated in advance with a Sudan Black solution. This treatment was employed to prevent autofluorescence caused by the presence of Manuka Honey and essential oils (EOs) (see section 3.3.3). Specifically, a solution of Sudan Black at 0.3% w/v was prepared using 70% ethanol and applied to the membranes. Subsequently, the membranes were rinsed with phosphate-buffered saline (PBS). To ensure sterility, the plates were subjected to 30 minutes of UV light sterilization.

Cells were then seeded into the wells at a density of 50,000 cells per well and cultured for the specified time points. These samples were compared to a control group, which consisted of cells seeded onto Tissue Culture Plates without the treated membranes.

#### 2.4.1.1 PrestoBlue® Assay

The PrestoBlue assay was employed to evaluate cell viability and proliferation. This assay relies on a color change triggered by the metabolic activity of cells, ultimately rendering the solution fluorescent. The assessments were conducted at the 24-hour, 72-hour, and 7-day time points. To prepare the PrestoBlue (PB) solution, filtered PB was combined with DMEM media at a ratio of 1:10 (v/v) and thoroughly vortexed.

The procedure involved removing the media from the wells, followed by a sterile PBS wash. Subsequently, the PB solution was added to the wells. For calibration purposes, a control containing only the PB solution was included to serve as a blank reference for the measurement instrument. The multi-well plates were then incubated at 37°C for 2 hours, covered with foil, ensuring uniform conditions. Triplicate measurements were taken for each sample and at each designated time point. The results were analyzed using the FLUOstar Omega MicroPlate Reader from BMG Labtech, with fluorescence measured at 560 nm excitation and 590 nm emission wavelengths.

After the measurements, the PB solution was completely aspirated from the wells, followed by two washes with PBS. Fresh media was then added, and the cell culture was continued until the subsequent time point.

#### 2.4.1.2 Live / Dead Assay

The Live/Dead® Assays were conducted at the 7-day time point to differentiate between viable and non-viable cells simultaneously. This assay involves staining viable cells in blue and dead cells in green. The staining solution was prepared following the manufacturer's instructions.

In summary, a solution was prepared by adding 10µL of calcein-AM (acetoxymethyl) solution and 5µL of propidium iodide solution into 5mL of PBS, followed by thorough vortexing. The resulting solution was then applied to the wells in a thin layer. The wells were subsequently incubated for 30 minutes, after which the results were examined using a fluorescence microscope (EVOS M5000, Thermo Fisher).

#### Bacterial Tests

The bacteria used in this study were *Klebsiella pneumoniae* (Gram-) and *Staphylococcus Aureus* (Gram+).

To begin, extract a colony from the specific bacteria and place it into a sterile tube containing 10 mL of Mueller-Hinton Broth (MHB). Afterward, incubate the tube at a

temperature of 37 degrees Celsius for a duration of 24 hours.

#### *2.4.1.3 Bacterial suspension preparation*

Begin by transferring 1 ml of the activated culture into a sterile 1.5 ml tube. Next, subject the tube to centrifugation at 5G for a duration of 5 minutes. Carefully remove the supernatant, and then resuspend the remaining material in 1 ml of Mueller-Hinton Broth (MHB).

Following this, it's time to prepare the serial dilution. Afterward, take 100µl from each dilution (10<sup>-5</sup>, 10<sup>-6</sup>, 10<sup>-7</sup>) and evenly spread it onto Brain Heart Infusion Agar (BHIA) plates, ensuring you have two duplicate plates for each dilution.

Now, place the plates in an incubator set at a temperature of 37 degrees Celsius and allow them to incubate for 24 hours. After the incubation period, proceed to enumerate the surviving colonies on each plate.

#### *2.4.1.4 Bacteria inoculation and enumeration*

Start by taking 10 µl of the suspended bacterial solution and inoculate it onto the surface. Allow the surface to air dry in a sterile environment. Next, carefully transfer the dried surface into a 15 ml tube, and then add 5 ml of Modified Rappaport-Vassiliadis (MRD) broth to the tube.

Subsequently, place the tubes in an ultrasound bath for a duration of 7.5 minutes to ensure thorough mixing.

From the 15 ml tube, create serial dilutions using a 1:9 ratio, which means mixing 1 part of the bacterial spension with 9 parts of MRD broth. Following this, plate 100 µl from each of the dilutions and then, place the plates in an incubator set at a temperature of 37 degrees Celsius, and let them incubate for a period of 24 hours.

Finally, after the incubation period, proceed to enumerate the surviving colonies on each plate.

## Chapter 3: Results and Discussion

### 3.1 Nanoemulsions

In the figure 3.1 we can observe a macro-image of the essential oil emulsions. Because of the presence of Tween80, a supernatant, they appear like turbid milky solutions, that has an aspect like that reported by Moradi & Barati [119].



**Figure 3.1** *Macroscopic view of the nanoemulsions.*

#### 3.1.2 Morphological Characterization - Transmission Electron Microscopy (TEM)

Transmission Electron Microscopy (TEM) analysis was conducted to provide a morphological characterization of the nanoemulsions containing essential oils, specifically focusing on their shape and size. Figure 3.2 displays the findings derived from the tea tree essential oil (EO) nanoemulsions. The particles exhibited a spherical morphology, with a noticeable variation in size. The average diameter of these particles was quantified using ImageJ software, ranging from 43 nm to 176 nm. Additionally, some agglomerates can be observed in the images.

For what concerns Eucalyptus EO, the images obtained are shown in figure 3.3. The medium diameter ranged from 77 nm to 153 nm, however, few particles were visible.

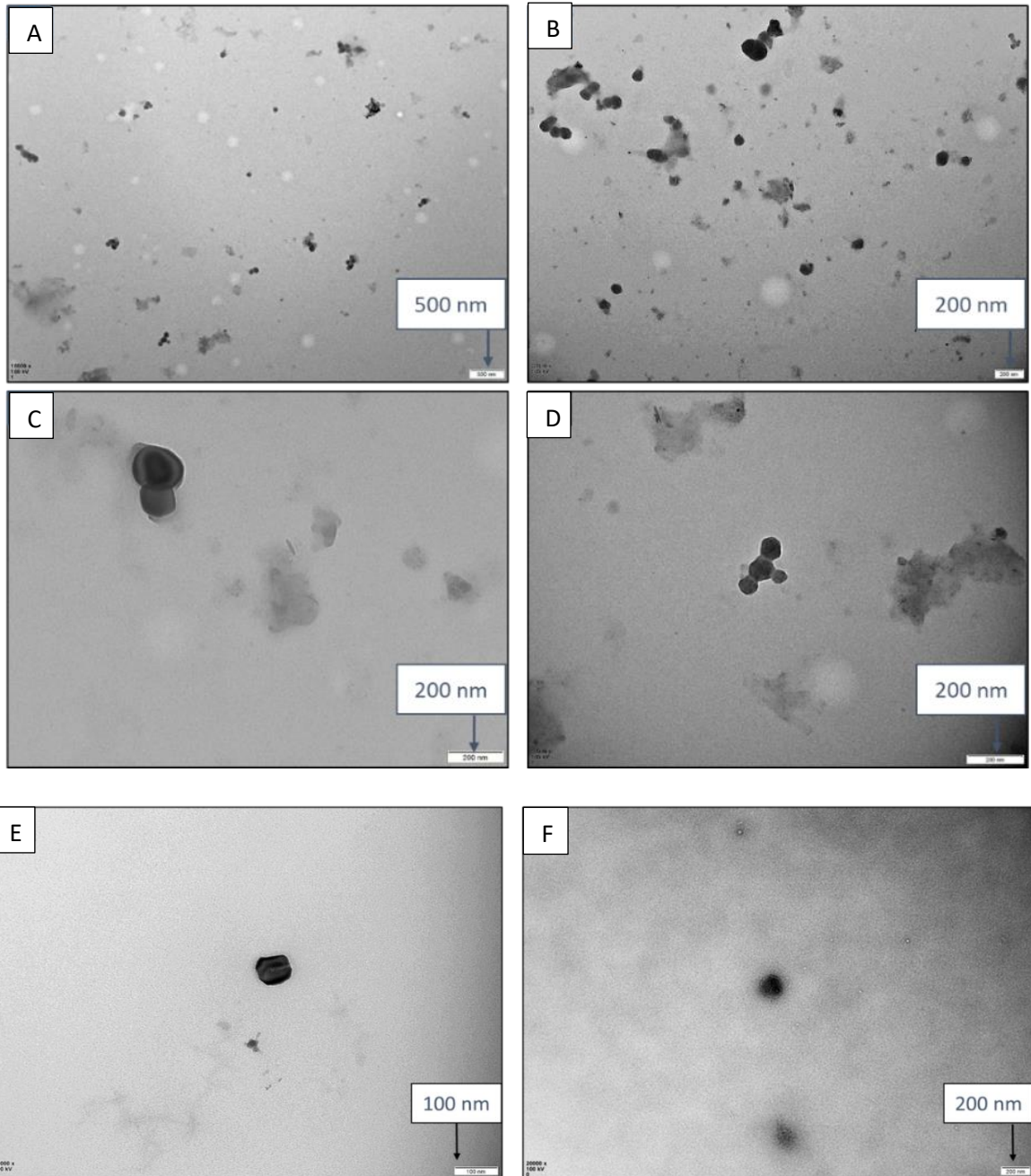


**Figure 3.2** TEM images of Tea Tree Oil NE.

**Figure 3.3** TEM images of Eucalyptus Oil NE

The challenge of achieving sufficient visibility of nanoemulsions in TEM analysis arises from the lack of adequate contrast between the particles and the background, as mentioned in reference [125]. To address this issue, it is advisable to employ staining techniques to enhance the visibility of the emulsions. Negative staining is a commonly used approach, which involves applying a staining agent to the samples after they have been placed on a copper grid. This staining agent typically targets and stains the background rather than the particles themselves. An example of such a negative stain is phosphotungstic acid, as illustrated in reference [119].

## 3.2 Morphological Characterization – Scansion Electron Microscopy (SEM)

### 3.2.1 Electrospun membrane

SEM imaging was performed on the samples prepared during the optimization phase (2.2.2). Many of these membranes exhibited filature defects such as beads and ribbons, suggesting that the combination of parameters used was not suitable. The best example demonstrating the optimal combination of these various parameters is depicted in Figure 3.4.

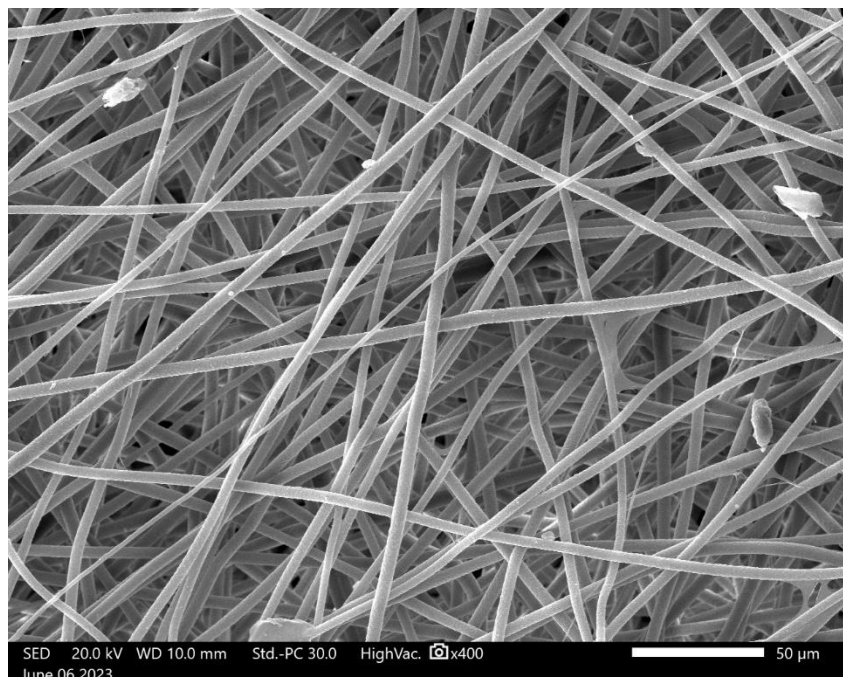


**Figure 3.4** SEM images of defective electrospun membranes. The parameters used in terms of PCL concentration, distance needle-collector, voltage and flow-rate were: 12% w/v - 14 cm - 600  $\mu$ l/h – 14kV

The optimal parameters selected from the optimization trial are listed in Table 3.4. These choices were made based on the absence of defects and the achievement of the thinnest nanofiber diameter.

**Table 3.4** Electrospinning parameters chosen after optimization .

PARAMETERS	VALUE
PCL concentration	12%
Flow-rate	600 $\mu$ l/h
Voltage	14 kV
Distance needle-collector	1a4 cm

The membranes produced under these specified parameters exhibited an absence of any imperfections (see Figure 3.5). The fibers displayed nanoscale dimensions, with an average diameter of  $207 \pm 73.6$  nanometers, as determined using ImageJ software. Moreover, these fibers exhibited a uniform distribution across the membrane.

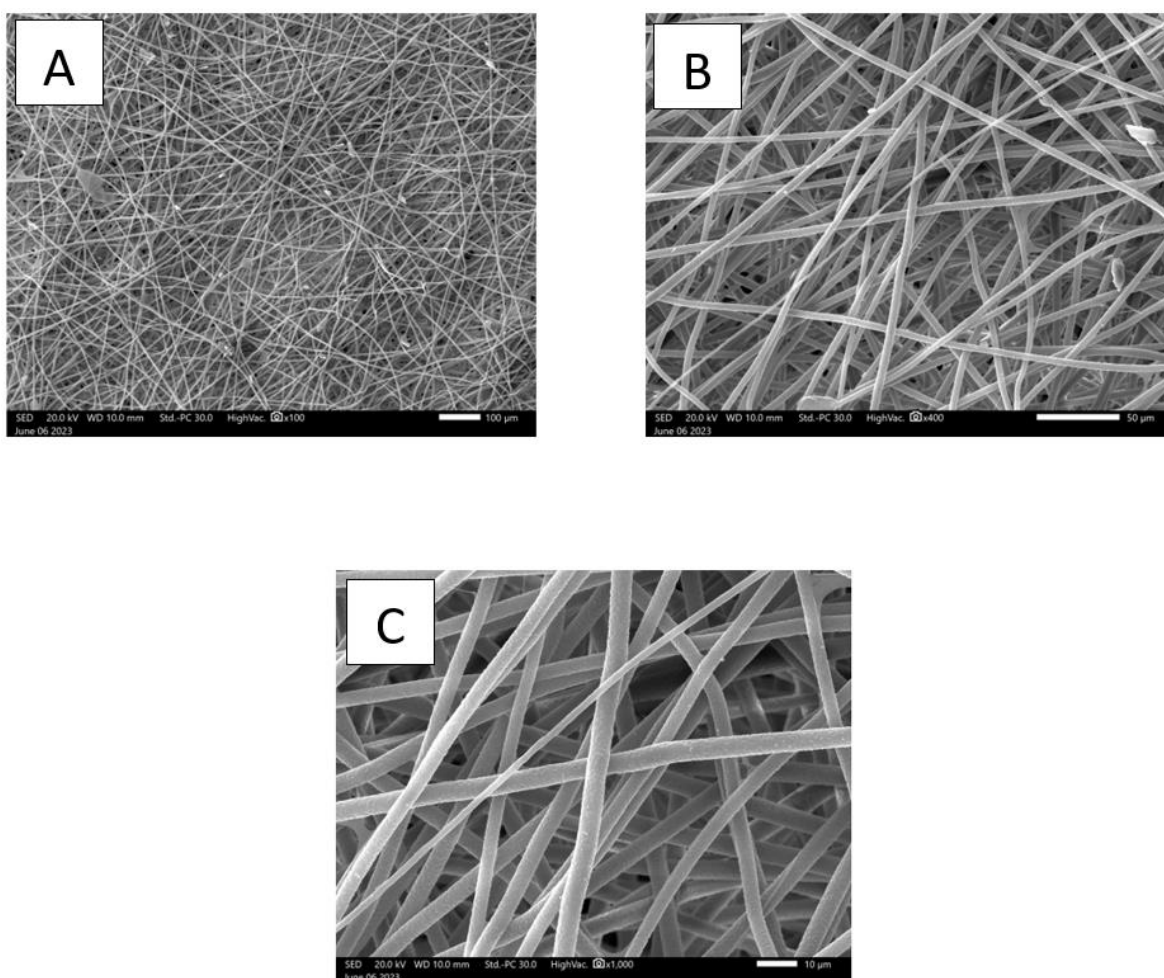


**Figure 3.5** Different magnifications of the nanofibers obtained with the optimized parameters. A) X2500 magnification; B) X13000 magnification; C) X25000 magnification.

A picture of the electrospun membrane at the macroscopic scale is shown in figure 3.6.

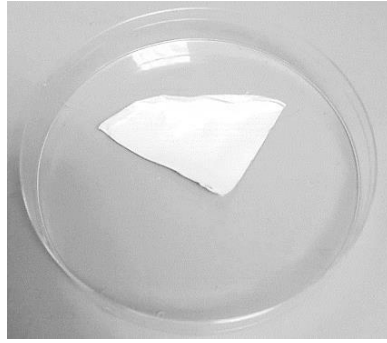


**Figure 3.6** *Macroscopic view of the electrospun membrane.*

### 3.3 Layer-by-layer coating

The overall appearance of the coated membrane can be observed in Figure 3.7. A noticeable distinction is the yellowish hue of the coated membrane, which contrasts with the brilliant white color of the uncoated membrane. This variation in color is attributed to the incorporation of Manuka honey.

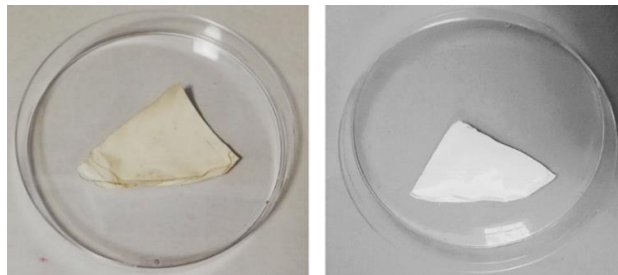


**Figure 3.7** *Coated membrane compared to the non-coated one*

**3.3.1 Morphological Characterization - Scansion Electron Microscopy (SEM)**  
 Scanning Electron Microscopy (SEM) analysis was conducted on the coated membranes to assess the presence of the coating and to examine its growth as the number of layers comprising the coating increased. This analysis is illustrated in Figure 3.8.

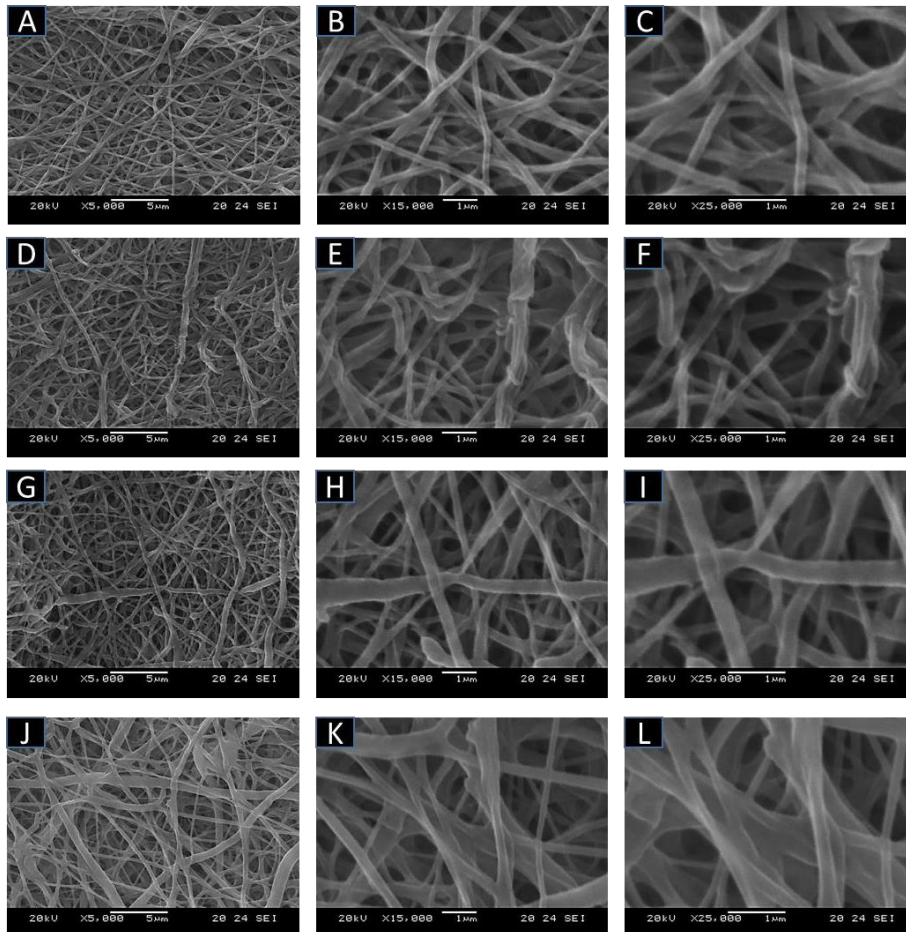


**Figure 3.8** SEM imaging of Layer-by-Layer coatings at various magnifications: A), B), C) 8-layer coating; D), E), F) 14-layer coating without essential oils; G), H), I) 14-layer coating with tea tree essential oil integrated into Manuka honey; J), K), L) 14-layer coating with Eucalyptus essential oil integrated into Manuka honey.

The diameters of the fibers on the coated membranes were evaluated with ImageJ Software, and the average diameter was determined for each specific condition. In the case of an eight-layer coating, the average diameter was found to be 287.7 nm, while for the fourteen-layer assembly, it measured 348 nm. This is in contrast to the 209 nm diameter recorded for the uncoated membrane, as detailed in section 3.2.1. These findings enable the establishment of a linear relationship between the number of layers and the thickness of the coated fibers. Consequently, by applying straightforward mathematical calculations, the thickness of a single bilayer can be estimated at approximately 20 nm. These thickness values under various conditions are visually depicted in Figure 3.9.

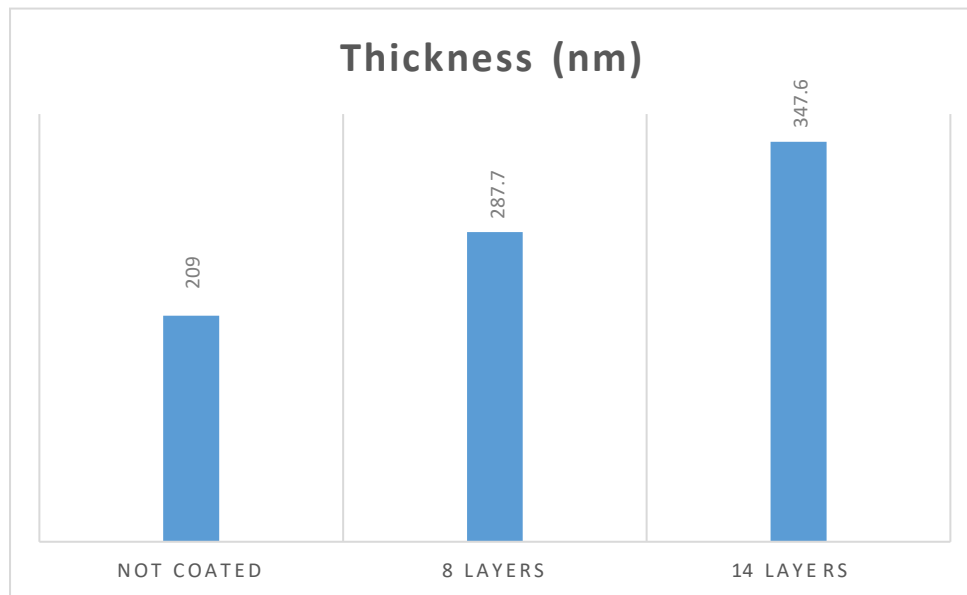


**Figure 3.9** Thickness of the membranes in three different conditions

Furthermore, the SEM images indicate that the presence of the coating does not exercise any discernible impact on the morphological characteristics of the membranes. It is evident that both the porosity and the nanostructure of the membranes remain intact and unaltered.

### 3.3.2 Physicochemical Characterization

#### 3.3.2.1 Fourier Transformed Infrared Spectroscopy with attenuated total reflectance (FTIR-ATR)

FTIR-ATR analysis was performed to investigate the surface's functional groups on the samples before and after the Layer-by-Layer assembly. The tested materials included aminolyzed PCL, an eight-layer coating, a fourteen-layer coating without essential oils, a fourteen-layer coating with essential oils (EO), and a fourteen-layer coating containing tea tree oil (TTO). The spectral data for these experiments is presented in Figure 3.9.

The spectrum of the uncoated membrane displayed typical wavelength bands indicative of pure PCL. An intense peak at 1727  $\text{cm}^{-1}$  corresponds to the carbonyl stretching ( $\text{C}=\text{O}$ ) within the polymer. Additionally, the peaks at 2866  $\text{cm}^{-1}$  and 2945  $\text{cm}^{-1}$  are characteristic of symmetric and asymmetric stretching of  $\text{CH}_2$  bonds, respectively [128] [129]. Furthermore, the presence of PCL-related peaks is evident, with a peak at 1240  $\text{cm}^{-1}$  representing asymmetric  $\text{C}-\text{O}-\text{C}$  stretching and another at 1170  $\text{cm}^{-1}$  indicating symmetric  $\text{O}-\text{C}-\text{O}$  stretching [128].

In the uncoated sample, a minor peak at 3460  $\text{cm}^{-1}$  (highlighted in the figure) can be attributed to the  $\text{N}-\text{H}$  stretching of amines [130]. Furthermore, a peak at 1246  $\text{cm}^{-1}$  corresponds to the stretching of the  $\text{C}-\text{N}$  bond of amines [131]. These observations are consistent with the aminolysis of the membrane using hexamethylenediamine to expose  $\text{NH}_2$  groups as an initial step for the layer-by-layer process.

In the spectrum of the sample with eight layers, new peaks emerge in the 1700 - 1500  $\text{cm}^{-1}$  range. Specifically, peaks at 1690  $\text{cm}^{-1}$  (indicative of  $\text{C}=\text{O}$  stretching) and 1641  $\text{cm}^{-1}$  (associated with  $\text{OH}$  deformation) suggest the presence of Manuka honey [132]. Additionally, in the same region, there is a peak at approximately 1570  $\text{cm}^{-1}$ , which is linked to  $\text{N}-\text{H}$  bending vibrations, indicating the presence of chitosan [133]. These observations are consistent with the sample coated with 14 layers, excluding the incorporation of essential oils, as it replicates the peaks observed in the eight-layer coating. The sample related to the 14 layers coating incorporating EO showed interesting differences. The 'fingerprint' of EO is contained in the range 1800 – 600  $\text{cm}^{-1}$  [The combination of ATR-FTIR and chemometrics for rapid analysis of essential oil from Myrtaceae plants – A review]. Nevertheless, in this case, its identification is more challenging due to a significant overlap with the peaks of other compounds. This phenomenon was observed at approximately 1570  $\text{cm}^{-1}$ , corresponding to the  $\text{C}=\text{C}$

bonding in aromatic molecules [134], which overlaps with the N-H group of chitosan, as mentioned earlier. Another distinctive peak in essential oils (EO) is located at 1150  $\text{cm}^{-1}$  (corresponding to C-O-C) [135]; however, in this case, it shifted due to overlapping with the peak at 1170  $\text{cm}^{-1}$  of PCL. The observed spectral changes can be attributed to various molecular interactions and functional groups within the samples:

1. The increase in the peak at approximately 1055  $\text{cm}^{-1}$  can be attributed to the presence of C-O stretching in alcohols [131].
2. A new peak at 1646  $\text{cm}^{-1}$  is noteworthy, indicative of C=C stretching within the benzene ring [135].
3. The broad peak spanning the range 3600–3000  $\text{cm}^{-1}$ , centered at 3300  $\text{cm}^{-1}$ , is associated with OH groups present in phenols within the oil [136].
4. The peak at 748  $\text{cm}^{-1}$  is a distinctive feature of the =CH vibration absorption of benzene rings [134].
5. Notably, the sample containing TTO exhibited a peak centered at 3450  $\text{cm}^{-1}$ , linked to the presence of -OH groups. This peak is similar to the one observed in the previous sample but appears smoother [137].
6. Zooming in on the graph reveals the presence of a 'flat region' in comparison to other samples, which typically exhibit distinct peaks. This flat region may be attributed to the presence of a broad band associated with C=C bond vibrations of alkene groups, ranging from 1690 to 1580  $\text{cm}^{-1}$  [137].
7. The characteristic peaks of CH<sub>2</sub> bonds within PCL appear smoother and less pronounced in comparison to other samples. This smoothing can be attributed to the presence of TTO-related peaks in the region ranging from 2961 to 2876  $\text{cm}^{-1}$ , stemming from symmetric and asymmetric stretching vibrations of -CH, -CH<sub>2</sub>, -CH(CH<sub>3</sub>), and -CH(CH<sub>2</sub>) groups [137].

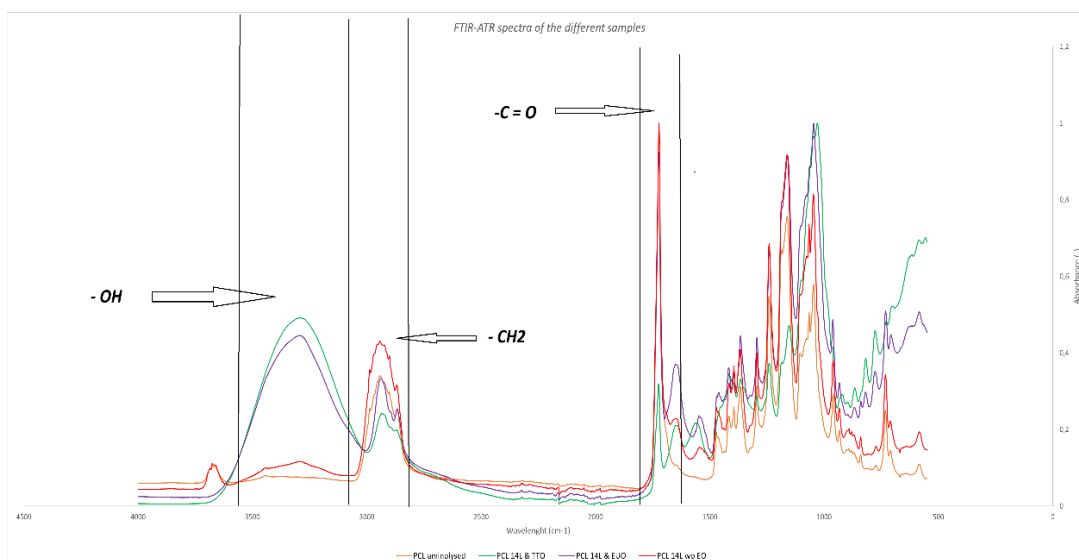


**Figure 3.9** FTIR-ATR spectra of the different samples. Inserts: magnification of the wavelength range where the main shifts or changes in peaks were observed.

The analysis provides confirmation of the successful formation of the coating. Given its nanometric thickness, there is still observable information about the chemical bonds of the PCL-substrate at the surface. However, the presence of other compounds is evident due to shifts in the peaks and the emergence of new ones. This suggests that the polyelectrolytes effectively bond together through electrostatic interactions.

### 3.3.2.2 X-Ray photoelectron Spectroscopy (XPS)

The surface chemical composition of the membranes was explored using X-Ray Photoelectron Spectroscopy (XPS). Figure 3.10 presents the survey spectra of the samples, and Table 3.6 summarizes the atomic percentages of the elements detected during the analysis.

Carbon (C 1s) at 285 eV and oxygen (O 1s) at 532 eV were consistently identified in all samples, which is expected as they are fundamental elements present in both the substrate and coating materials. In the case of the uncoated PCL sample, nitrogen (N 1s) at 399 eV was also detected. This presence can be attributed to the aminolysis treatment performed on the membranes for functionalization.

Subsequently, in the samples coated with two layers, the N 1s signal was not detected. This suggests the successful formation of the first layer with Manuka honey efficiently interacting with the substrate. Manuka honey itself does not inherently contain nitrogen atoms, and it's possible that the layer's thickness may have obscured the detection of aminolyzed groups, given that the analysis depth is approximately 5 nm. In contrast, chitosan does contain nitrogen atoms, and its absence in the second layer might indicate that the expected interaction did not occur as anticipated or that chitosan was entirely removed during the washing step. Starting from the eight-layer coating and onward, the nitrogen peak re-emerged prominently, affirming the presence of chitosan as a positively charged polyelectrolyte within these layers. Moreover, sodium (Na 1s), a significant component of the buffer solution used to dissolve the polyelectrolytes, was detected at 1070 eV. A minimal quantity of silicon (Si 2p) was observed at 102 eV, with the 1L sample exhibiting slightly higher levels, possibly due to contamination.

**Table 3.6** Atomic percentages of the elements detected by XPS analysis.

Sample	Atomic %			
	O 1s	C 1s	N 1s	Na 1s
Aminolysed PCL	28.57	68.05	1.63	n.d.
2L	18.16	80.76	n.d.	n.d.
8L	22.26	72.1	3.18	1.1
14L	22.49	71.44	2.97	1.47
8L & TTO	26.90	68.90	2.09	2.26
8L & EO	29.85	67.28	2.87	n.d.
14L & TTO	29.60	66.45	2.86	1.09
14L & EO	28.65	66.59	4.76	n.d.

Furthermore, to better investigate the increasing and decreasing trends of the atomic percentages, high resolution XPS was conducted on C 1s, and spectra deconvolution was performed.

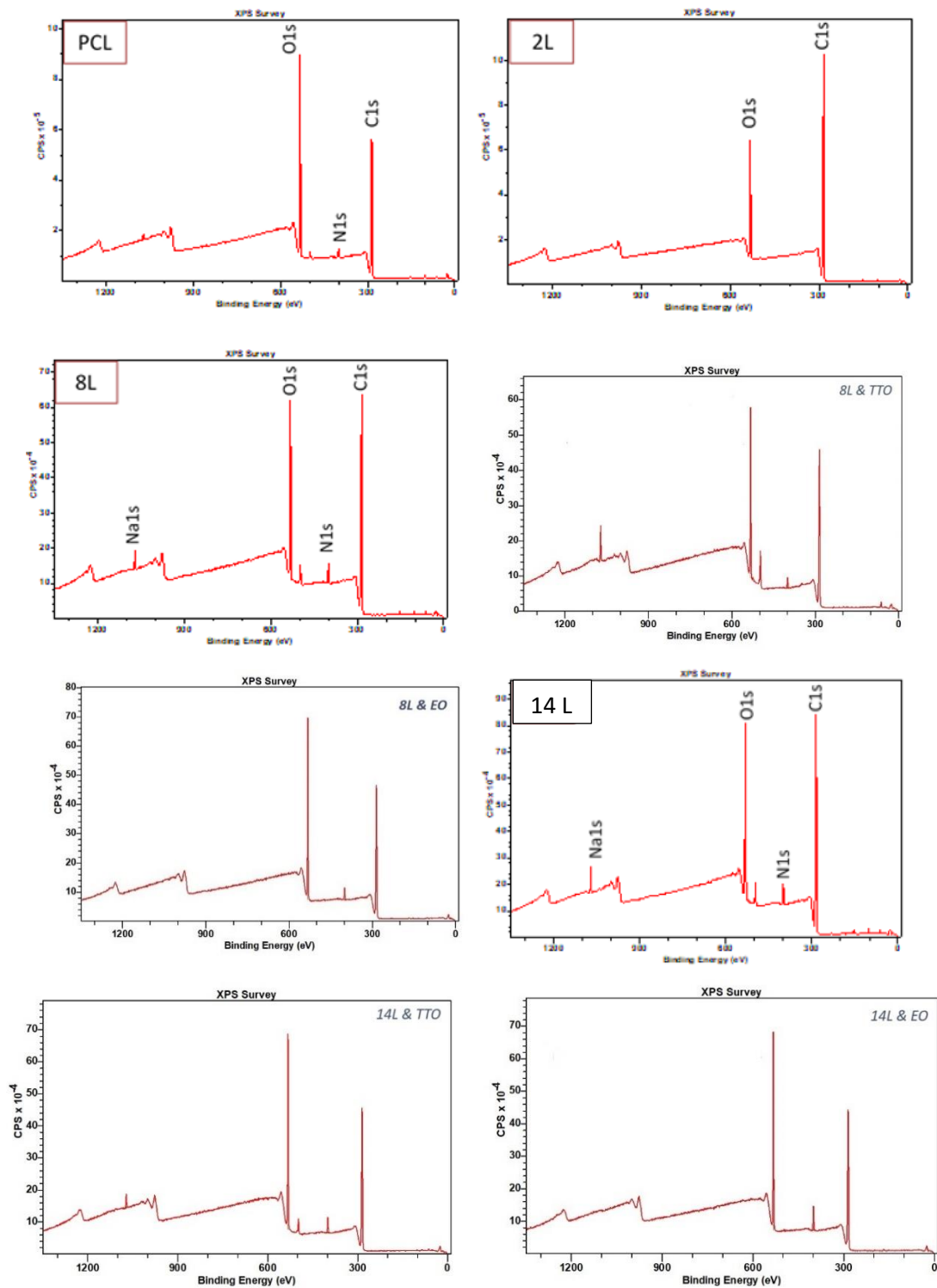


Figure 3.10 XPS survey spectra of the analysed samples: PCL, 2L, 8L, 8L & TTO, 8L & EO, 14L, 14L & TTO and 14L & EO.

- **Aminolysed PCL:** The deconvolution of the C 1s spectrum revealed two distinctive peaks associated with the C-N bond and electron density (ED) shifts, specifically occurring at 285.92 eV [138] and 286.11 eV [139]. In addition to these, there were other characteristic peaks indicative of the PCL (polycaprolactone) structure. These included a peak at 288.10 eV, corresponding to the C=O bond [140], and peaks at 284.60 eV [140] and 285.08 eV [141], which are associated with the C-C bond.

Detailed images illustrating these findings can be found in Figure 3.11

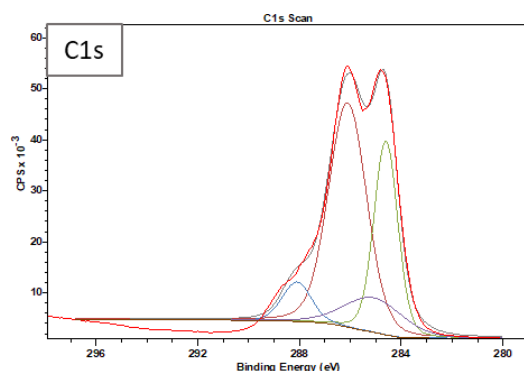


Figure 3.11 XPS high-resolution spectra of C of aminolysed PCL sample.

The percentages of atomic concentrations associated with each bond type are presented in Table 3.7. The notably high concentration of the C-N bond can be attributed to the aminolysis process, which exposes NH<sub>2</sub> groups at the surface of the material.

Table 3.7 Atomic concentration (%) for each bond typology of aminolysed PCL sample.

	<b>C-N</b>	<b>C=O</b>	<b>C-C</b>	<b>C-O</b>
<b>Atomic Conc (%)</b>	65.62	2.76	2.22	26.30

- **2 Layers:**

The deconvolution of the C 1s spectrum has provided further insights into the chemical composition of the material. Here are the key findings:

A peak at 284.81 eV indicative of aromatic groups was observed, suggesting that the previous layer containing Manuka honey is still detectable.

The peak at 288.83 eV is associated with carboxylate carbon (C=O/O=C-O) [150].

Another peak at 286.22 eV corresponds to a C-O bond [151], while 285.08 eV represents the C-C/C=C bond [141].

Detailed images illustrating these findings can be found in Figure 3.12.

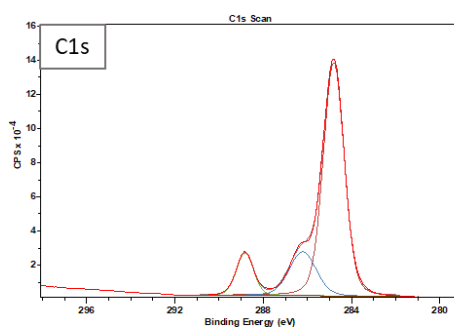


Figure 3.12 XPS high-resolution spectra of C of 2 layers sample.

The percentages of the atomic concentrations related to each bond typology are reported in table 3.8.

Table 3.8 Atomic concentration (%) for each bond typology of 2 layers sample.

	N-C=N	C=O/O=C-O	C-C/C=C	C-O	C-N-C	C-OH	-OH
<b>Atomic Conc (%)</b>	4.90	0.73	73.85	1.18	0.01	0.82	16.60

**8 Layers.** The deconvolution of the C 1s spectrum revealed the presence of several peaks and related chemical bonding, providing detailed insights into the material's composition:

A peak at 284.78 eV corresponds to C=C bonding [154]. At 286.14 eV, there is evidence of C-N bonding [155].

The peak at 288.59 eV is associated with C=O bonding [156]. Another C=C peak is observed at 287.34 eV [157]. A peak at 285.16 eV signifies C-C bonding [158].

These detailed deconvolutions are depicted in Figure 3.13, providing a comprehensive view of the chemical bonds and species present in the material.

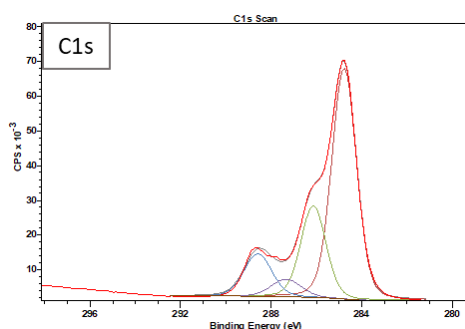


Figure 3.13 XPS high-resolution spectra of C of 8 layers sample.

The percentages of the atomic concentrations related to each bond typology are reported in table 3.9.

	C-N	C-N	C=C	C-O	C-C	-OH	-NH
<b>Atomic Conc %</b>	1.35	0.69	3.64	1.18	66.49	20.63	2.93

**Table 3.9** Atomic concentration (%) for each bond typology of 8 layers sample.

**14 Layers.** We can appreciate the presence of aromatic groups at 284.81 eV thanks to the deconvolution of C1 peaks, while at 286.30 and 285.60 eV indicated C–O bonding [166] [167], 288.71 eV carboxylate carbon -COO<sup>-</sup> [168], 287.74 eV C=O [169] and 285.18 C-C bonding.

The deconvolution is shown in figure 3.13.

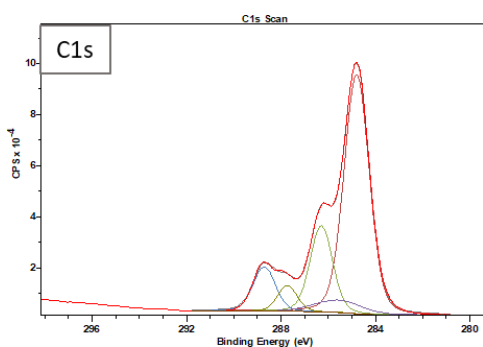


**Figure 3.13** XPS high-resolution spectra of C of 14 layers sample.

The percentages of the atomic concentrations related to each bond typology are reported in table 3.10.

**Table 3.10** Atomic concentration (%) for each bond typology of 14 layers sample.

	N-C=N	C=O	COO <sup>-</sup>	C-O	C-C	N-C=O	-NH
<b>Atomic Conc (%)</b>	3.57	20.97	0.59	1.5	65.67	0.22	2.73

**8 Layers & TTO.** The deconvolution of the C 1s spectrum in this analysis reveals similar peaks compared to the previous analysis which are at 284.82 eV representing the aromatic carbon and at 286.30 eV for the C-O bonding. Peaks at 287.44 eV indicated the presence of C=O [172]. Moreover, the peak at 285.31 eV corresponds to C-C bond.

The deconvolution are shown in figure 3.14.

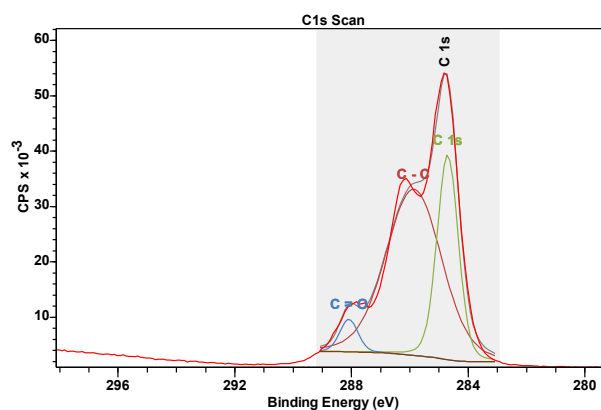


Figure 14 XPS high-resolution spectra of C of 8 layers sample with the last 4 incorporating TTO.

The percentages of the atomic concentrations related to each bond typology are reported in table 3.11.

Table 3.11 Atomic concentration (%) for each bond typology of 8 layers sample with the last 4 incorporating TTO.

	C-O	C-C	C-H
Atomic Conc (%)	4.19	65.14	30.67

**8 Layers & EUO.** Through the carbon deconvolution, we can discern that the aromatic peak reappeared at 284.81 eV. The peak at 286.32 eV corresponds to the O=C-N bond [178], while the peaks at 288.13 eV and 285.25 eV are associated with the C=O [179] and C-N [180] bonds, respectively. The deconvolution results are illustrated in Figure 3.15.

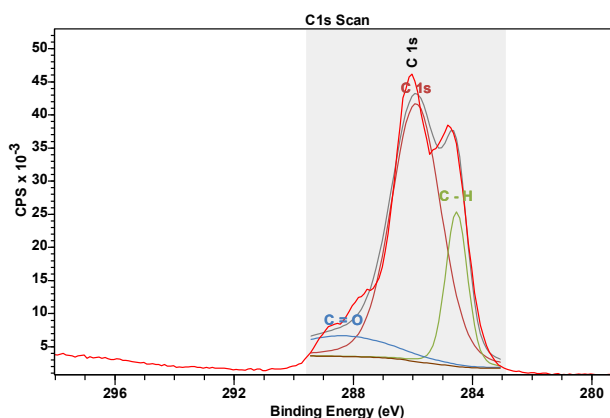


Figure 3.15 XPS high-resolution spectra of C of 8 layers sample with the last 4 incorporating CEO.

Table 3.12 Atomic concentration (%) for each bond typology of 8 layers sample with the last 4 incorporating CEO.

	N-C=N & O=C-N	C=O	C-N-C-	C-N
Atomic Conc (%)	5.14	23.38	0.17	67.67

**14 Layers & TTO.** The carbon peak with aromatic properties appears at 284.82 electronvolts (eV).

Additionally, at 286.25 eV, 287.97 eV, and 285.09 eV, peaks corresponding to C-O [188], C-N [189], and C-C [190] can be observed, respectively.

The deconvolution is shown in figure 3.16.

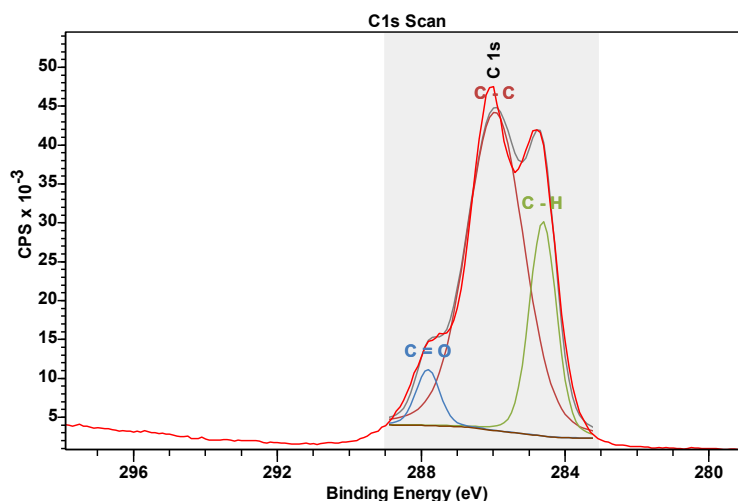


Figure 3.16 XPS high-resolution spectra of C of 14 layers sample with the last 4 incorporating TTO.

The percentages of the atomic concentrations related to each bond typology are reported in table 3.13.

Table 3.13 Atomic concentration (%) for each bond typology of 10 layers sample with the last 4 incorporating TTO.

	C-O/C=O	C-N	C-C
Atomic Conc (%)	21.46	0.06	67.81

**14 Layers & EUO.** Through the process of carbon deconvolution, it becomes evident that there are atoms within the aromatic ring groups at 284.78 electronvolts (eV), as well as carbon atoms involved in C-N/C-

O bonds at 286.30 eV [193]. Furthermore, peaks at 288.42 eV and 285.09 eV represent the presence of C=C [194] and C-C bonds, respectively.

The deconvolution is shown in figure 3.17.

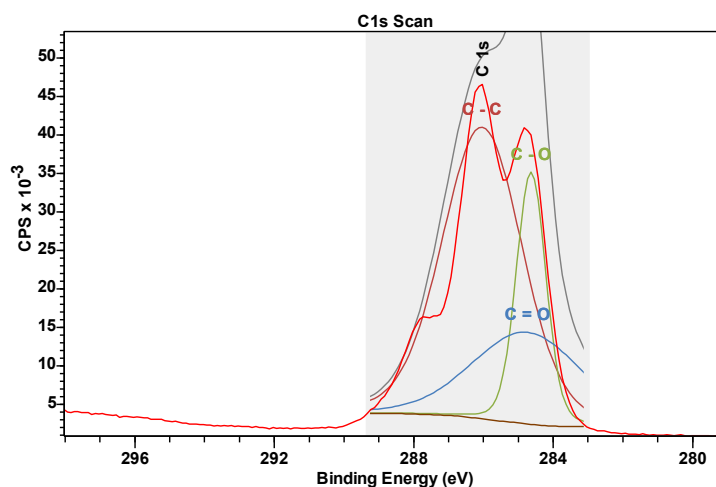


**Figure 3.17** XPS high-resolution spectra of C, of 10 layers sample with the last 4 incorporating EO.

The percentages of the atomic concentrations related to each bond typology are reported in table 3.14.

**Table 3.14** Atomic concentration (%) for each bond typology of 10 layers sample with the last 4 incorporating CEO.

	C-C	C=C	C-O	C-O/N-C
<b>Atomic Conc (%)</b>	66.62	0.75	20.93	3.25

X-ray Photoelectron Spectroscopy (XPS) analysis is an incredibly powerful tool, enabling the investigation of sample surfaces to detect chemical bonds and the atomic composition of the primary elements of interest. In this particular case, it has facilitated the identification of the polyelectrolytes used for coating. Specifically, the presence of aromatic groups in the initial layer indicates the utilization of Manuka honey (a negative polyelectrolyte - found in odd-numbered layers), while the presence of -NH<sub>2</sub> groups is indicative of chitosan (a positive polyelectrolyte - present in even-numbered layers). By comparing samples with 14 layers, one can discern the presence of essential oils by examining changes in the atomic concentration of aromatic carbon. Furthermore, the presence of (C-N-C) and (N-C=O) bonding confirms the occurrence of electrostatic interactions between the layers.

### 3.3.2.3 Methylglyoxal Assay Test

Thanks to MGO kit, we have obtained, for each chosen time point, an associated absorbance value, which once inserted into an equation defining a calibration line, instead of abscissas, allows us to obtain the concentration of MGO released from the membrane in that time interval.

The equation is:

$$f(x) = 1.6194x - 0.009$$

which goes to describe the calibration line (Fig 3.18)

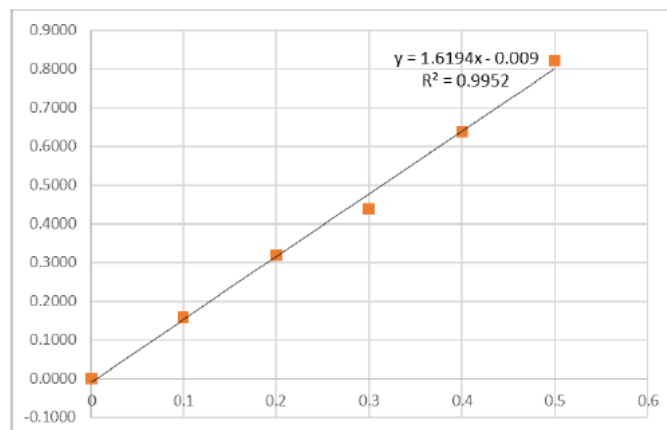
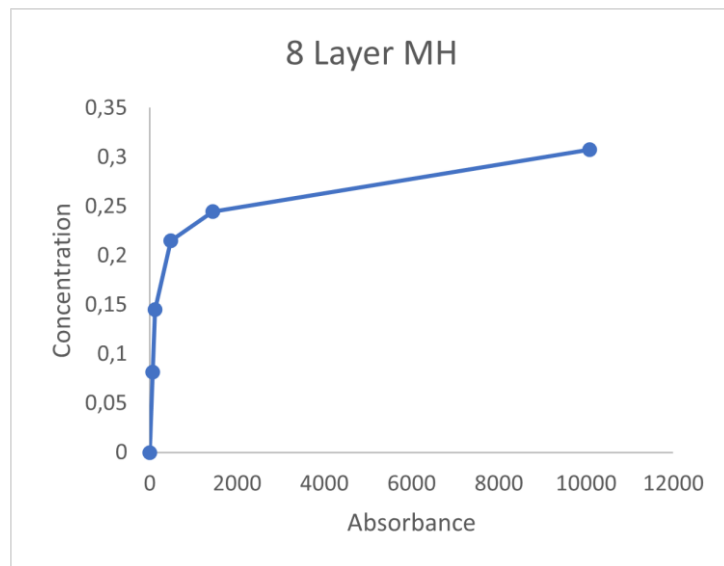


Figure 3.18 Calibration line

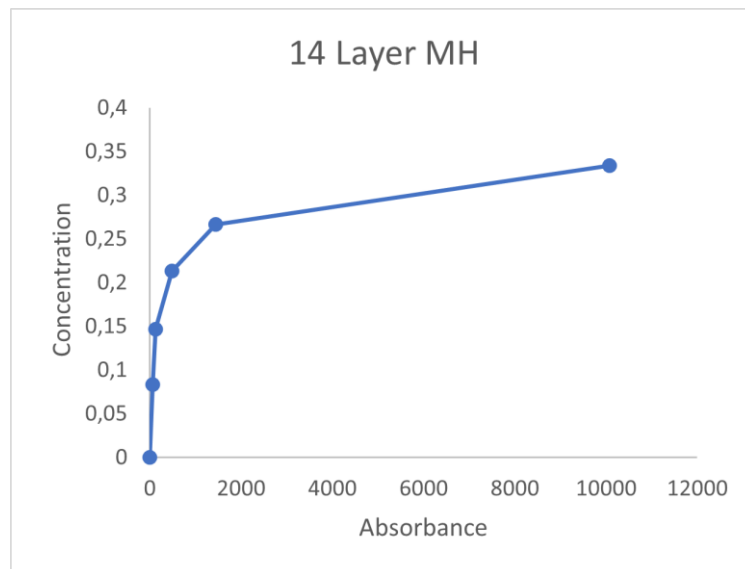
## 8 Layer MH

8 Layer MH			8 Layer MH	
Time step	Absorbance	Concentration	0	0
60 min	0,123	0,081511671	60	0,081511671
2 h	0,0935	0,063295048	120	0,144806719
8 h	0,1045	0,070087687	480	0,214894405
24 h	0,0395	0,029949364	1440	0,244843769
7 days	0,0925	0,062677535	10080	0,307521304



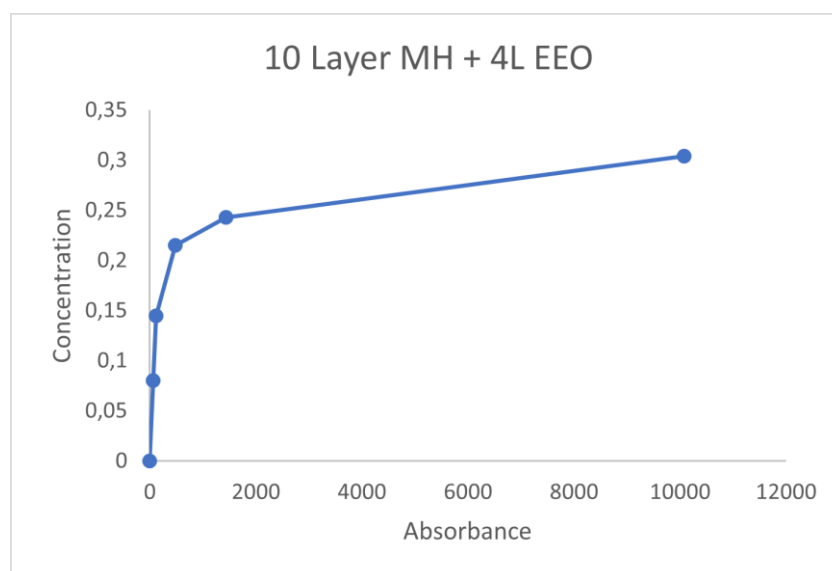
## 14 Layer MH

10 Layer MH			14 Layer MH	
Time step	Absorbance	Concentration	0	0
60 min	0,1265	0,083672965	60	0,083672965
2 h	0,0935	0,063295048	120	0,146968013
8 h	0,0985	0,066382611	480	0,213350624
24 h	0,077	0,053106089	1440	0,266456712
7 days	0,1	0,06730888	10080	0,333765592



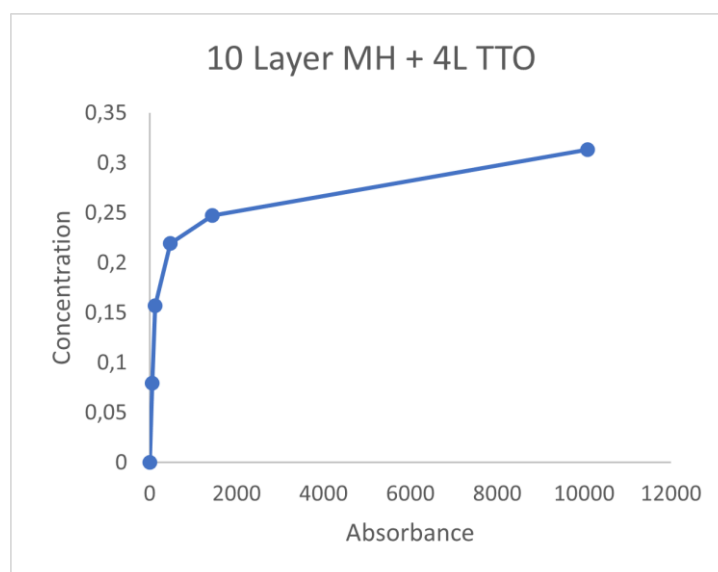
### 10 Layer MH + 4 Layer EEO

10 Layer MH + 4L EEO			10 Layer MH + 4L EEO	
Time step	Absorbance	Concentration		
60 min	0,121	0,080276646	0	0
2 h	0,095	0,064221317	60	0,080276646
8 h	0,1055	0,070705199	120	0,144497962
24 h	0,036	0,02778807	480	0,215203162
7 days	0,0895	0,060824997	1440	0,242991231
			10080	0,303816228



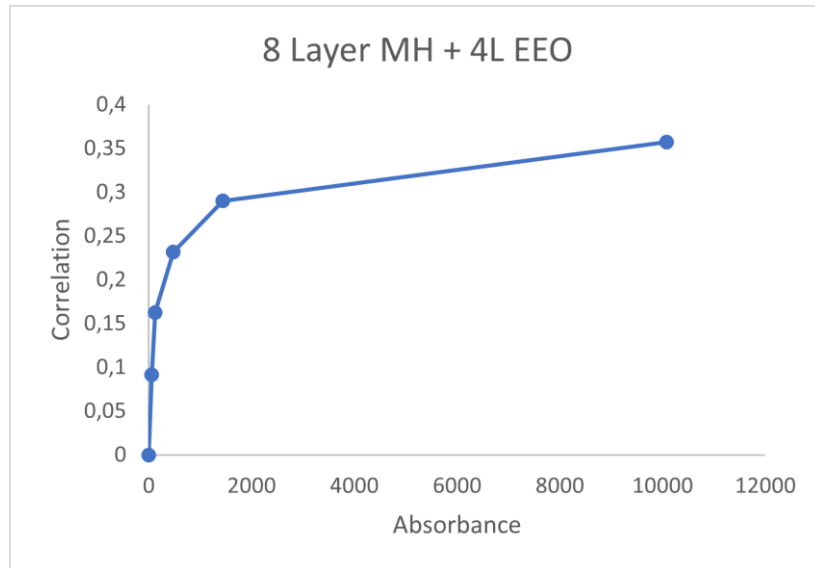
## 10 Layer MH + 4 Layer TTO

10 Layer MH + 4L TTO		10 Layer MH + 4L TTO		
0	0	Time step	Absorbance	Concentration
60	0,079659133	60 min	0,12	0,079659133
120	0,157054053	2 h	0,116333333	0,07739492
480	0,219628669	8 h	0,092333333	0,062574616
1440	0,247210901	24 h	0,035666667	0,027582232
10080	0,313078918	7 days	0,097666667	0,065868017



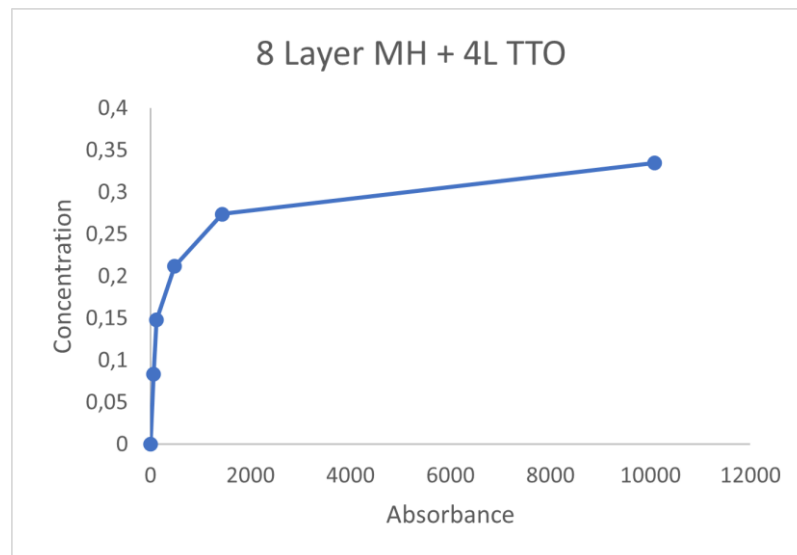
## 8 Layer MH + 4 Layer EEO

8 Layer MH + 4L EEO			8 Layer MH + 4L EEO	
Time step	Absorbance	Concentration	0	0
60 min	0,138666667	0,091186036	60	0,091186036
2 h	0,107	0,071631468	120	0,162817504
8 h	0,102333333	0,068749743	480	0,231567247
24 h	0,086	0,058663703	1440	0,29023095
7 days	0,099333333	0,066897205	10080	0,357128154



### 8 Layer MH + 4 Layer TTO

8 Layer MH + 4L TTO			8 Layer MH + 4L TTO	
Time step	Absorbance	Concentration	0	0
60 min	0,126666667	0,083775884	60	0,083775884
2 h	0,094666667	0,064015479	120	0,147791363
8 h	0,094666667	0,064015479	480	0,211806842
24 h	0,091666667	0,062162941	1440	0,273969783
7 days	0,089666667	0,060927916	10080	0,334897699



thanks to the concentration time plots, we can observe that , from the point of view of the release of MGO, the various samples assume the same behaviour, testimony to the fact that at each time point the amount of MGO released is the same.

## 3.4 Biological evaluation

### 3.4.1 Cellular Test

The Neo-Fibroblast cells used in this study and observed under an optical microscope are depicted in Figure 3.25



*Figure 3.25 View at the optical microscope of neo-fibroblast cells employed in the cellular tests.*

Cell tests were conducted following the procedures outlined in section 2.4.1. The samples subjected to testing included:

1. PCL membrane without any coating.
2. PCL membrane coated with 14 layers of MH+CH.
3. PCL membrane coated with 14 layers of MH+CH incorporating TTO (Tea Tree Oil).
4. PCL membrane coated with 14 layers of MH-CH incorporating EO (Essential Oils).

These samples were then compared to a control group that consisted solely of cells.

#### 3.3.4.2 PrestoBlue® Assay

PrestoBlue® Assay was carried out to examine the metabolic activity and, consequently, the viability of the cells that came into contact with the electrospun membranes coated with various materials (see Figure 3.26). The level of viability is directly linked to the intensity of fluorescence emission measured at 590 nm.

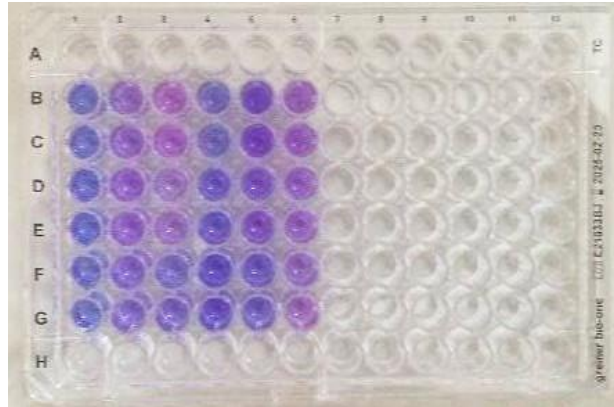


Figure 3.26 Multiwell Plate in which PrestoBlue assay

Histograms displaying the results obtained for various samples at the three time-point are illustrated in figure 3.27.

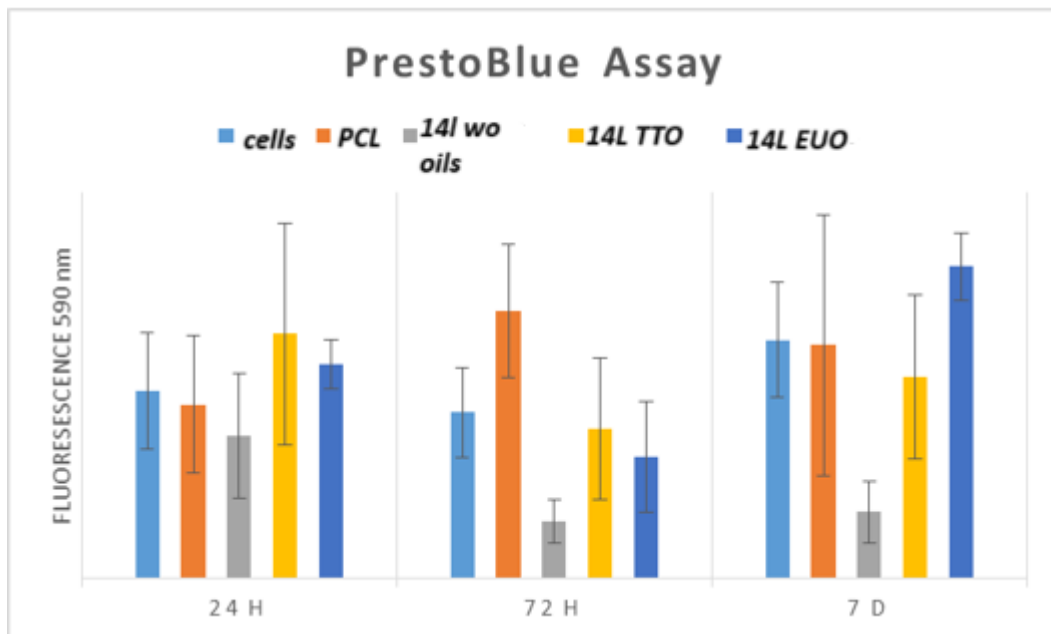


Figure 3.27 Histograms of PB results of the samples at different time points.

Statistical evaluation of variances in PrestoBlue® assay outcomes was accomplished through a one-way analysis of variance (ANOVA) considering the five samples and three distinct time-points. Subsequently, post hoc pairwise comparisons between two means were executed employing Tukey's test, with a predetermined level of statistical significance established at  $p < 0.05$  (\*).

Table 3.17 provides a legend detailing the samples and time-points for reference.

**Table 3.17** Legend of samples and time-points employed in the statistical analysis (ANOVA).

	<b>1</b>	<b>2</b>	<b>3</b>	<b>4</b>	<b>5</b>
<b>Sample</b>	CTRL Cells	PCL	14L	14L & TTO	14L & CEO
<b>Time-point</b>	24 h	72 h	7d	/	/

The analysis initially examined disparities for each sample type at various time points (24 hours, 72 hours, and 7 days). Subsequently, distinctions among the different samples at the same time point were also investigated.

Based on the statistical analysis, it can be inferred that there are no substantial variances at the initial time point (24 hours), signifying that cell viability is comparable across all sample types during this period. However, at the second time point (72 hours), differences emerged between samples 2-3, 2-4, 2-5, and 3-1, with a p-value of 0.000, indicating statistical significance. Finally, at 7 days, noteworthy differences were observed solely between sample 3 and samples 1, 2, and 5, with a p-value of 0.001.

To gain a deeper understanding of these differences, it is helpful to examine the statistical analysis for each type of sample over time. For samples 1, 2, and 4 (cells, PCL, and 14L & TTO), no significant differences in cell number were observed among the time points. Regarding sample 3 (14 layers without coating), time points 2 and 3 differed from 1 (but not from each other), indicating a decrease in cell viability over time (p-value 0.011). Time points related to sample 5 displayed differences as well.

It's intriguing to note that for sample 5, significant differences were observed between each of its time points (p-value 0.000). The cell viability trend for this sample is remarkable: there was an initial decrease in viability from 24 hours to 72 hours, succeeded by a rapid increase over the following 7 days, ultimately exceeding the viability value at 24 hours.

The percentage of cell viability can be calculated using the following equation:

$$\% \text{ cell viability} = \frac{\text{sample fluorescence}}{\text{control fluorescence}} \times 100$$

The control fluorescence measurement is associated with the scenario involving cells only, without the

presence of membranes, after a 24-hour period. A graphical representation of the observed trends is depicted in Figure 3.28.

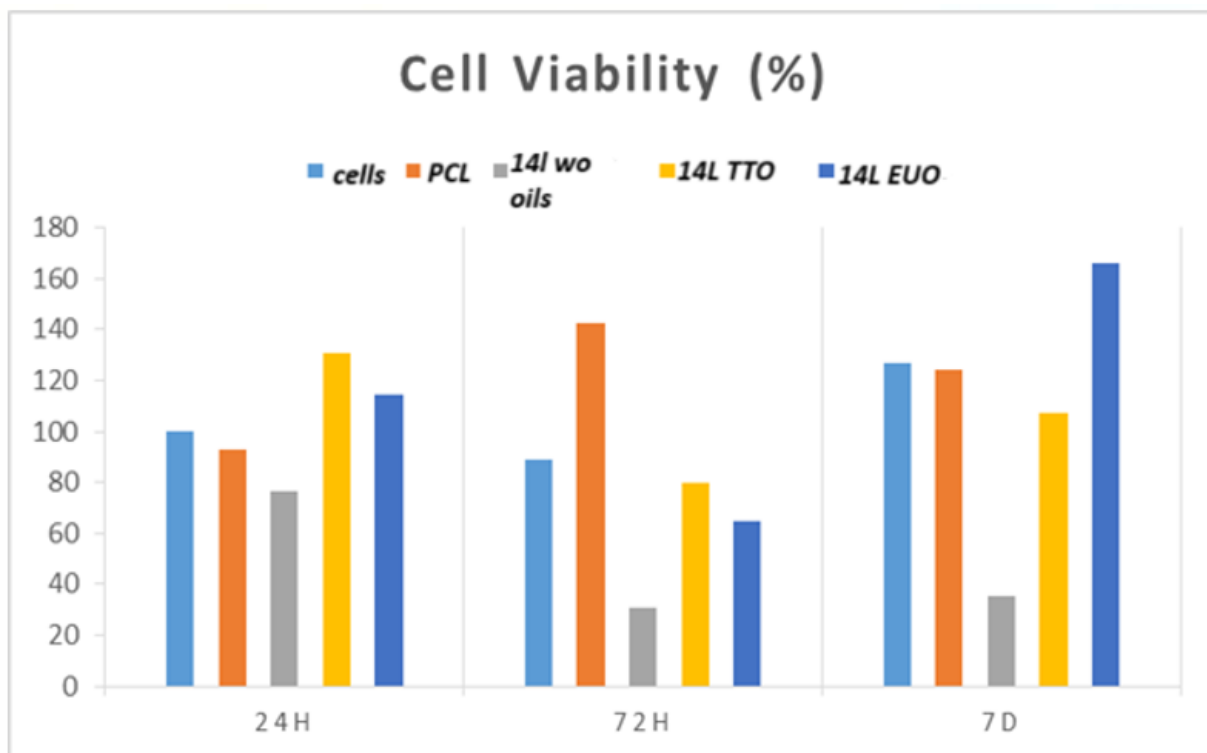


Figure 3.28 Histogram chart representing the viability (%) of the cells in contact with the samples at the different time-points.

These findings indicate that the viability of the neo-fibroblasts remained largely intact when in contact with the membranes. Notably, the only exception was sample number 3, which had 14 layers without essential oils, resulting in a roughly 50% decrease in viability while still maintaining some level of viability. The increased viability of fibroblasts in contact with the membrane containing Chief Executive Officer (CEO) is intriguing and unexpected. Given the absence of relevant data in the existing literature, further investigation into the impact of CEO on human cells is warranted.

Additionally, the results obtained from the Live/Dead Assay images (3.4.1.2), conducted using a fluorescence microscope, corroborated the findings obtained from the previous Protein Binding (PB) assay.

### 3.4.2 Live/Dead Assay

Figure 3.29 display the Live/Dead fluorescence images captured at the 7-days time-points. In this images, viable cells are marked by blue fluorescence, while non-viable cells are identified by green fluorescence.

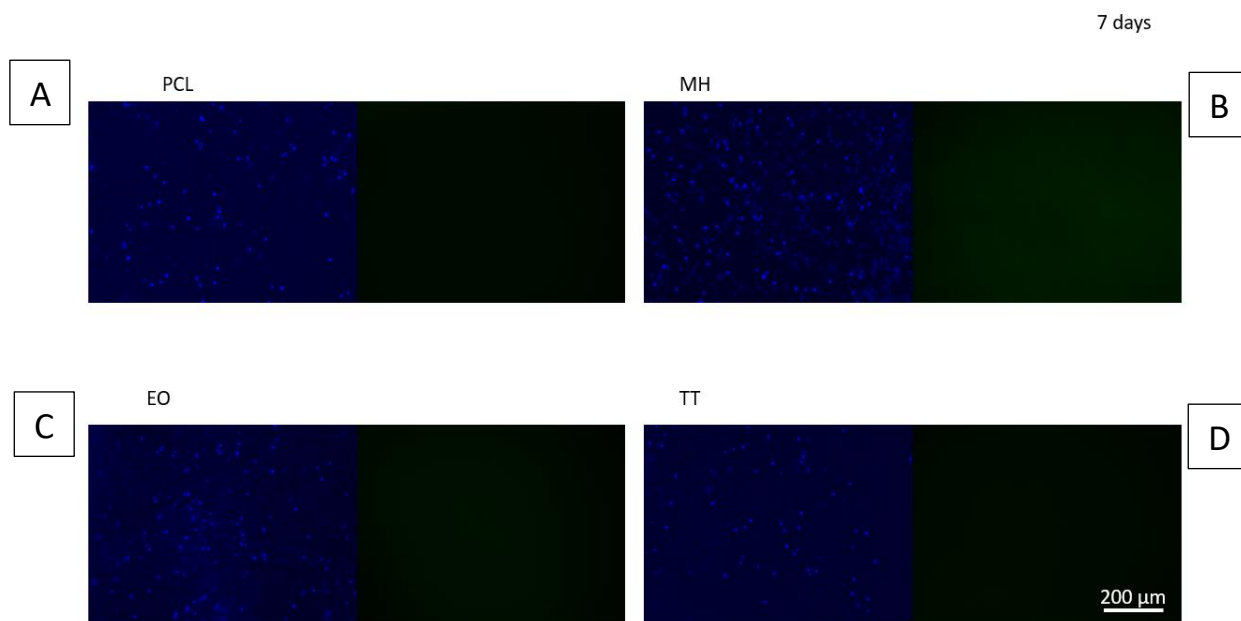


Figure 3.29 Live/Dead assay at 7-days. A) PCL, B) 14-layer wo oils, C) 14 layers & TTO, D) 14 layers & CEO. Bar 200  $\mu\text{m}$ .

At the 7-days mark, all cells exhibited complete viability. We can observe, by referring to the pictures in the figure 3.29, that the cells are alive, marked in blue, while in the quadrant that turns out to be completely black, we do not notice any green fluorescence, which would testify to the fact that some cells are dead. Furthermore, it can be seen that the number of live cells is much greater when analysing the membrane in figure B, consisting solely of 14 layers of MH without essential oils, and that in figure C, where the last layers are functionalised with eucalyptus essential oils, again referring to the control, figure A, membrane of aminolysed PCL only. In contrast, in the membrane functionalised with Tea Tree essential oils, figure D, fewer cells are observed.

### 3.4.3 Bacterial tests

The graphs in the Figure 30 and in the Figure 31 (*Staphylococcus aureus* and *Klebsiella pneumoniae* respectively) represent an estimate of the quantity of bacterial cells, respectively recruited on the different membranes, both functionalised and non-functionalised, taken into account.

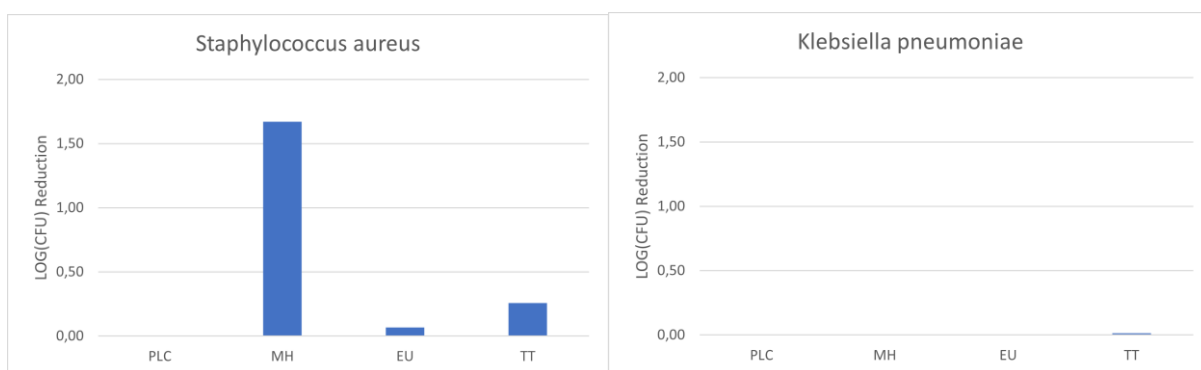


Figure 3.30 and 31 - quantity of bacterial cells (*Staphylococcus aureus* and *Klebsiella pneumoniae* respectively), respectively recruited on the different membranes

According to the results of the bacteriological tests, illustrated in the graphs above, we can see that, as far as *Staphylococcus* is concerned, the presence of MO in the layers covering the membrane does not constitute a pronounced antibacterial effect. Quite the opposite in the case of *Klebsiella*, where the effect of MH contributes to the bacteria not being deposited on the membrane. In both cases, on the other hand, the effect of the essential oils, eucalyptus and tea tree, is determining in the antibacterial action, more pronounced in the case of *Klebsiella* rather than the *Staphylococcus*.

## Chapter 4: Conclusions and future perspectives

Persistent wounds linked to antibiotic resistance represent a global health challenge, necessitating the immediate exploration of novel treatment approaches. In this research, we have developed and examined contemporary wound dressings coated with natural antimicrobial compounds. By utilizing electrospun membranes made of polycaprolactone, we have successfully emulated the structure and function of the extracellular matrix (ECM). The chosen coating method, involving layer-by-layer assembly, has effectively created a nanoscale coating without altering the substrate's nanostructure or porosity.

The analysis conducted confirms the successful formation of the coating: X-ray Photoelectron Spectroscopy (XPS) revealed the presence of chemical bonds between the layers, while Fourier Transform Infrared Spectroscopy with Attenuated Total Reflection (FTIR-ATR) enabled the differentiation of various coating compositions. Additionally, scanning electron microscopy (SEM) imaging indicated a nanoscale thickness of the coating (approximately 160 nm for a 14-layer coating).

A noteworthy innovation in this study is the exclusive use of natural compounds within the coating. The natural polyelectrolyte solutions forming the layers exhibited antibacterial properties, as demonstrated by bacterial tests. Chitosan (1% w/v) completely inhibited the bacterial strains, while manuka honey (20% w/v) showed partial susceptibility with the presence of some resistant colonies. Further exploration of different manuka honey concentrations is advisable to determine the minimum concentration required for complete antibacterial efficacy.

Regarding the nanoemulsions of essential oils (EOs) incorporated into manuka honey solutions, their long-term stability warrants additional investigation. Emulsion stability is correlated with  $\zeta$ -potential, which should be considered in experimental design for more reliable statistical predictions. Evaluating the cytotoxicity of higher EO concentrations (above the 4% w/v employed) on cells is also of interest, as excessive EO concentrations can be cytotoxic to human cells. Additionally, agar diffusion tests for the combination of manuka honey and EOs should be conducted.

In conclusion, these types of membranes are well-suited for dry or low-exuding wounds, with the layer composition optimized for immediate and sustained antibacterial action while minimizing cytotoxicity, allowing cell proliferation and tissue regeneration.

Future advancements in wound healing will likely involve 3D skin bioprinting technology. This approach combines bioprinting strategies, bioinks, and cells to create skin models with controlled architecture, mimicking physiological skin structure and function in a highly reproducible manner.

Finally, it may be advisable to consider the use of natural polymers, such as Gellan Gum, instead of synthetic PCL, with the aim of enhancing the membrane's biocompatibility and minimizing the potential

for rejection by the body.

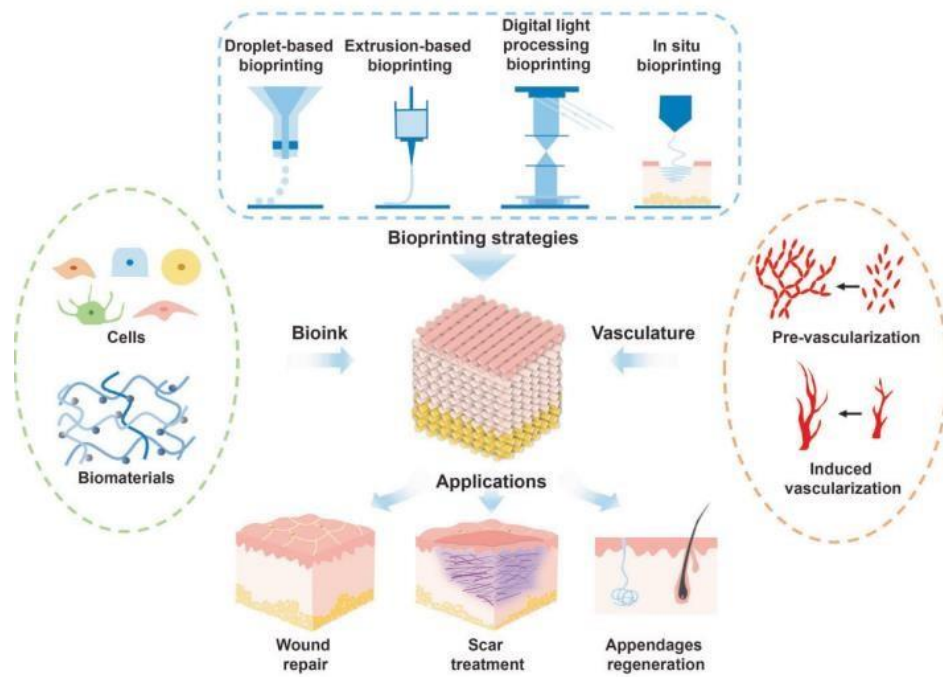


Figure 4.1 Representation of the elements involved in skin bioprinting [198].

## References

- [1] A. Ibrahim, N. Bagherani, B. Smoller e N. Bagherani, «Anatomy and Organization of Human Skin,» in *Atlas of Dermatology, Dermatopathology and Venereology*, Springer Nature Switzerland, 2022.
- [2] K. M. G. C. Kolarsick PAJ, «Anatomy and Physiology of the Skin,» *Journal of the Dermatology Nurses' Association*, 2011.
- [3] P. Kolarsick, M. Kolarsick e C. Goodwin, «Anatomy and Physiology of the Skin,» *Journal of the Dermatology Nurses' Association*, 2011.
- [4] J. Fenner e R. Clark, «Anatomy, Physiology, Hystology and Immunohistochemistry of Human Skin,» in *Skin Tissue Engineering and Regenerative Medicine*, Academic Press, 2016.
- [5] A. Ibrahim, N. Bagherani, B. Smoller, C. Reyes-Barron e N. Bagherani, «Functions of the Skin,» in *Atlas of Dermatology, Dermatopathology and Venereology*, Springer Nature Switzerland, 2022.
- [6] J. Abdo, N. Sopko e S. Milner, «The applied anatomy of human skin: A model for regeneration,» *Wound Medicine*, 2020.
- [7] C. DeBenedictis, S. Joubbeh, G. Zhang, M. Barria e R. Ghohestani, «Immune functions of the skin,» *Clinics in Dermatology*, 2001.
- [8] C. Bangert, P. Brunner e S. G., «Immune functions of the skin,» *Clinics in Dermatology*, 2011.
- [9] J. Quaresma, «Organization of the Skin Immune System and Compartmentalized Immune Responses in Infectious Diseases,» *ASM Journals*, 2019.
- [10] T. Velnar, T. Bailey e V. Smrkolj, «The Wound Healing Process: an Overview of the Cellular and Molecular Mechanisms,» *The Journal of International Medical Research*, 2009.
- [11] J. Reinke e H. Sorg, «Wound Repair and Regeneration,» *Eur Surg Res*, 2012.
- [12] F. Thiruvoth, D. Mohapatra, D. Sivakumar, R. Chittoria e V. Nandhagopal, «Current concepts in the physiology of adult wound healing,» *Plast Aesthet Res*, 2015.
- [13] S. Guo e L. DiPietro, «Factors Affecting Wound Healing,» *J Dent Res*, 2010.
- [14] K. Las Herasa, M. Igartuaa, E. Santos-Vizcaino e R. Hernandez, «Chronic wounds: Current status, available strategies and emerging therapeutic solutions,» *Journal of controlled release*, 2020.
- [15] A. Gonzalez, T. Costa, Z. Andrade e A. Medrado, «Wound healing - A literature review,» *An Bras Dermatol*, 2016.
- [16] N. Menke, K. Ward, T. Witten, D. Bonchev e R. Diegelmann, «Impaired wound healing,» *Clinics in dermatology*, 2007.
- [17] S. Gupta, S. Sagar, G. Maheshwari, T. Kisaka e S. Tripathi, «Chronic wounds: magnitude, socioeconomic burden and consequences,» *Wound Asia*, 2021.
- [18] K. Järbrink, G. Ni, H. Sönnergren, A. Schmidtchen, C. Pang, R. Bajpai e J. Car, «Prevalence and incidence of chronic wounds and related complications: a protocol for a systematic review,» *Systematic Reviews*, 2016.
- [19] A. Siddiqui e J. Bernstein, «Chronic wound infection: Facts and controversies,» *Clinics in dermatology*, 2010.
- [20] K. Järbrink, G. Ni, H. Sönnergren, A. Schmidtchen, C. Pang, R. Bajpai e J. Car, «The humanistic and economic burden of chronic wounds: a protocol for a systematic review,» *Systematic Reviews*, 2017.
- [21] J. Larouche, S. Sheoran, K. Maruyama e M. Martino, «Immune Regulation of Skin Wound Healing: Mechanisms and Novel Therapeutic Targets,» *Advances in Wound Care*, 2018.
- [22] B. J. Siddiqui AR, «Chronic wound infection: Facts and controversies,» *Clinics in Dermatology*, 2010.
- [23] «Fortune Business Insights,» [Online]. Available: <https://www.fortunebusinessinsights.com/industry-reports/chronic-wound-care-market-100222>.
- [24] R. Frykberg e J. Banks, «Challenges in the Treatment of Chronic Wounds,» *Mary Ann Liebert Inc publishers*, 2015.
- [25] S. Bowers e E. Franco, «Chronic Wounds: Evaluation and Management,» *Am Fam Physician*, 2020.
- [26] D. Pai e S. Madan, «Techniques in Chronic Wound Management: Review of the Literature and Recent Concepts,» *J Nov Physiother*, 2013.
- [27] K. Izadi e P. Ganchi, «Chronic Wounds,» *Clin Plastic Surg*, 2005.
- [28] P. Zarrintaj, A. Moghaddam e S. e. a. Manouchehri, «Can regenerative medicine and nanotechnology combine to heal wounds? The search for the ideal wound dressing,» *Nanomedicine*, 2017.
- [29] A. Andreassi, R. Bilenchi, M. Biagioli e C. D'Aniello, «Classification and pathophysiology of skin grafts,» *Clinics in Dermatology*, 2005.
- [30] L. Alrubaiy e A.-R. K.K., «Skin Substitutes: A Brief Review of Types and Clinical Applications,» *Oman Medical Journal*, pp. 4-6, 2009.
- [31] E. Ghomi, S. Khalili, S. Khorasani, R. Neisiany e S. Ramakrishna, «Wound dressings: Current advances and future directions,» *Journal of applied polymer science*, 2019.
- [32] S. Dhivya, V. Padma e E. Santhini, «Wound dressings - a review,» *Biomedicine*, 2015.
- [33] M. Farahani e A. Shafiee, «Wound Healing: From Passive to Smart Dressings,» *Advanced Healthcare Materials*, 2021.
- [34] R. Langer e V. J.P., «Tissue engineering,» *Science*, pp. 920-926, 1993.
- [35] D. Howard, L. Buttery, K. Shakesheff e S. Roberts, «Tissue engineering: strategies, stem cells and scaffolds,» *Journal of Anatomy*, p. 66–72, 2008.
- [36] L. Rodriguez Doblado, C. Martinez Ramos e M. Monleon Pradas, «Biomaterials for Neural Tissue Engineering,» *Frontiers in Nanotechnology*, 2021.
- [37] Y. Qin, «Advanced Wound Dressings,» *The Journal of the Textile Institute*, 2001.
- [38] R. Laurano, M. Boffito, G. Ciardelli e V. Chiono, «Wound dressing products: A translational investigation from the bench to the market,» *Engineered Regeneration*, pp. 182-200, 2022.

- [39] C. Shi, C. Wang, H. Liu e e. al., «Selection of Appropriate Wound Dressing for Various Wounds,» *Frontiers in Bioengineering and Biotechnology*, 2020.
- [40] K. Kus e E. Ruiz, «Wound Dressings - A Practical Review,» *Springer Science+Business Media*, 2020.
- [41] A. Gupta, M. Kowalczyk, W. Heaselgrave, S. Britland, C. Martin e I. Radecka, «The production and application of hydrogels for wound management: A review,» *European Polymer Journal*, 2018.
- [42] A. Stoica, C. Chircov e A. Grumezescu, «Nanomaterials for Wound Dressings: An Up-to-Date Overview,» *Molecules*, 2020.
- [43] C. Weller, V. Team e G. Sussman, «First-Line Interactive Wound Dressing Update: A Comprehensive Review of the Evidence,» *Frontiers in Pharmacology*, 2020.
- [44] R. Dong e G. B., «Smart wound dressings for wound healing,» *Nano Today*, 2021.
- [45] A. Kumar e A. Jacob, «Techniques in scaffold fabrication process for tissue engineering applications: A review,» *Journal of Applied Biology & Biotechnology*, pp. 163-176, 2022.
- [46] G. Devi, S. Anil e J. Venkatesan, «Biomaterials and Scaffold Fabrication Techniques for Tissue Engineering Applications,» *Engineering Materials for Stem Cell Regeneration*, p. 691–706, 2021.
- [47] N. Bhardwaj e S. Kundu, «Electrospinning: A fascinating fiber fabrication technique,» *Biotechnology Advances*, 2010.
- [48] A. Rogina, «Electrospinning process: Versatile preparation method for biodegradable and natural polymers and biocomposite systems applied in tissue engineering and drug delivery,» *Applied Surface Science*, 2014.
- [49] L. Villarreal-Gomez, J. Cornejo-Bravo, R. Vera-Graziano e D. Grande, «Electrospinning as a powerful technique for biomedical applications: a critically selected survey,» *Journal of Biomaterial Science, Polymer Edition*, pp. 157-176, 2016.
- [50] T. Subbiah, G. Bhat, R. Tock, S. Parameswaran e S. Ramkumar, «Electrospinning of Nanofibers,» *Journal of Applied Polymer Science*, pp. 557-569, 2005.
- [51] J. Xue, T. Wu, Y. Dai e Y. Xia, «Electrospinning and Electrospun Nanofibers: Methods, Materials, and Applications,» *Chemical Reviews*, pp. 5298-5415, 2019.
- [52] G. Rutledge e S. Fridrikh, «Formation of fibers by electrospinning,» *Advanced Drug Delivery Reviews*, pp. 1384-1391, 2007.
- [53] S. Suresh, A. Becker e B. Glasmacher, «Impact of Apparatus Orientation and Gravity in Electrospinning—A Review of Empirical Evidence,» *Polymers*, 2020.
- [54] G. Williams, B. Raimi-Abraham e C. Luo, «Electrospinning fundamentals,» in *Nanofibres in Drug Delivery*, UCL Press, 2018, pp. 24-59.
- [55] D. Lukas, A. Sarkar, L. Martinova, K. Vodsedalkova, D. Lubasova, J. Chaloupek, P. Pokorny, P. Mikes, J. Chvojka e M. Komarek, «Physical principles of electrospinning (Electrospinning as a nano-scale technology of the twenty-first century),» *Textile Progress*, pp. 59-140, 2009.
- [56] F. Davis, S. Mohan e M. Ibraheem, *Electrospinning: Principles, Practice and Possibilities*, The Royal Society of Chemistry, 2015.
- [57] P. Davoodi, E. Gill, W. Wang e Y. Huang, «Chapter Two - Advances and innovations in electrospinning technology,» in *Biomedical Application of Electrospinning and Electro spraying*, Woodhead Publishing Series in Biomaterials, 2021, pp. 45-81.
- [58] O. Suwanton, «Biomedical applications of electrospun polycaprolactone fiber mats,» *polymers advanced technologies*, pp. 1264-1273, 2016.
- [59] Z. Li e C. Wang, «Effects of Working Parameters on Electrospinning,» in *One-dimensional Nanostructures. Electrospinning Technique and Unique Nanofibers*, SpringerBriefs in Materials, 2013, pp. 15-28.
- [60] A. Haider, S. Haider e I. Kang, «A comprehensive review summarizing the effect of electrospinning parameters and potential applications of nanofibers in biomedical and biotechnology,» *Arabian Journal of Chemistry*, pp. 1165-1188, 2018.
- [61] Y. Sun, S. Cheng, W. Lu e Y. Wang, «Electrospun fibers and their application in drug controlled release, biological dressings, tissue repair, and enzyme immobilization,» *Royal Society of Chemistry Advances*, p. 25712–25729, 2019.
- [62] T. Sill e H. Von Recum, «Electrospinning: Applications in drug delivery and tissue engineering,» *Biomaterials*, pp. 1989-2006, 2008.
- [63] S. Habeeb, «Fabrication and Characterization of Tubular Polymeric Nano fibrous Composite,» *Thesis of PhD in chemical engineering - polymers nanotechnology*, 2018.
- [64] S. Lee, L. Yoo e A. Atala, «Biomaterials and Tissue Engineering,» *Clinical Regenerative Medicine in Urology*, p. 17–51, 2017.
- [65] J. Ding, J. Zhang, J. Li, D. Li, C. Xiao, H. Xiao, H. Yang, X. Zhuang e C. X. , «Electrospun polymer biomaterials,» *Progress in Polymer Science*, pp. 1-34, 2019.
- [66] D. Kai, S. Liow e X. Loh, «Biodegradable polymers for electrospinning: Towards biomedical applications,» *Materials Science and Engineering*, pp. 659-670, 2014.
- [67] D. Mondal, M. Griffith e S. Venkatraman, «Polycaprolactone-based biomaterials for tissue engineering and drug delivery: Current scenario and challenges,» *International Journal of Polymeric Materials and Polymeric Biomaterials*, pp. 255-265, 2016.
- [68] K. Aoki e N. Saito, «Biodegradable Polymers as Drug Delivery Systems for Bone Regeneration,» *Pharmaceutics*, 2020.
- [69] V. Guarino, G. Gentile, L. Sorrentino e L. Ambrosio, «Polycaprolactone: Synthesis, Properties, and Applications,» *Encyclopedia of Polymer Science and Technology*, pp. 1-36, 2017.
- [70] R. Dwivedi, S. Kumar, R. Pandey, A. Mahajan, D. Nandana, D. Katti e D. Mehrotra, «Polycaprolactone as biomaterial for bone scaffolds: Review of literature,» *Journal of Oral Biology and Craniofacial Research*, pp. 381-388, 2020.
- [71] M. Janmohammadi e M. Nourbakhsh, «Electrospun polycaprolactone scaffolds for tissue engineering: a review,» *International Journal of Polymeric Materials and Polymeric Biomaterials*, pp. 527-539, 2018.
- [72] M. Liu, X. Duan, Y. Li, D. Yang e Y. Long, «Electrospun Nanofibers for Wound Healing,» *Materials Science and Engineering*, 2017.
- [73] M. Abrigo, S. McArthur e P. Kingshott, «Electrospun Nanofibers as Dressings for Chronic Wound Care: Advances, Challenges, and Future Prospects,» *Macromolecular Bioscience*, 2014.
- [74] F. Hua e L. Y. , «Chapter 1 - Layer-by-layer assembly,» in *The New Frontiers of Organic and Composite Nanotechnology*, Elsevier, 2008, pp. 1-44.

- [75] A. Shukla e B. Almeida, «Advances in cellular and tissue engineering using layer-by-layer assembly,» *WIREs Nanomedicine and Nanobiotechnology*, pp. 411-421, 2014.
- [76] P. Hammond, «Building biomedical materials layer-by-layer,» *MaterialsToday*, pp. 196-206, 2012.
- [77] M. Matsusaki, H. Ajiro, T. Kida, T. Serizawa e M. Akashi, «Layer-by-Layer Assembly Through Weak Interactions and Their Biomedical Applications,» *Advanced Materials*, p. 454-474, 2012.
- [78] J. Richardson, M. Bjornmalm e F. Caruso, «Technology-driven layer-by-layer assembly of nanofilms,» *Science*, pp. 411-422, 2015.
- [79] P. Gentile, I. Carmagnola, T. Nardo e V. Chiono, «Layer-by-layer assembly for biomedical applications in the last decade,» *Nanotechnology*, 2015.
- [80] H. Ai, S. Jones e Y. Lvov, «Biomedical Applications of Electrostatic Layer-by-Layer Nano-Assembly of Polymers, Enzymes, and Nanoparticles,» *Cell Biochemistry and Biophysics*, pp. 23-43, 2003.
- [81] X. Zhang, Y. Xu, X. Zhang, H. Wu, J. Shen, R. Chen, Y. Xiong, J. Li e S. Guo, «Progress on the layer-by-layer assembly of multilayered polymer composites: Strategy, structural control and applications,» *Progress in Polymer Science*, pp. 76-107, 2018.
- [82] D. Alkheia, P. Hammond e A. Shukla, «Layer-by-Layer Biomaterials for Drug Delivery,» *Annual Reviews*, pp. 1-24, 2020.
- [83] J. Richardson, J. Cui, M. Bjornmalm, J. Braunger, H. Ejima e F. Caruso, «Innovation in Layer-by-Layer Assembly,» *Chemical Reviews*, p. 14828-14867, 2016.
- [84] «Google Patents,» [Online]. Available: <https://patents.google.com/patent/WO2021079106A1/en?q=WO+2021079106A1>.
- [85] Z. Zhang, J. Zeng, J. Groll e M. Matsusaki, «Layer-by-layer assembly methods and their biomedical applications,» *Biomaterials Science*, pp. 4077-4094, 2022.
- [86] L. Huang e M. Yang, «Hemocompatibility of Layer-by-Layer Hyaluronic Acid/Heparin Nanostructure Coating on Stainless Steel for Cardiovascular Stents and its Use for Drug Delivery,» *Journal of Nanoscience and Nanotechnology*, pp. 3163-3170, 2006.
- [87] E. De Avila, A. Castro, O. Tagit, B. Krom, D. Löwik, V. W. A., L. Bannenberg, C. Vergani e J. Van den Beucken, «Anti-bacterial efficacy via drug-delivery system from layer-by-layer coating for percutaneous dental implant components,» *Applied Surface Science*, pp. 194-204, 2019.
- [88] N. Shah, N. Hyder, J. Moskowitz, M. Quadir, S. Morton, H. Seeherman, R. Padera, M. Spector e P. Hammond, «Surface-Mediated Bone Tissue Morphogenesis from Tunable Nanolayered Implant Coatings,» *Science Translational Medicine*, 2013.
- [89] K. Cai, Y. Hu e K. Jandt, «Surface engineering of titanium thin films with silk fibroin via layer-by-layer technique and its effects on osteoblast growth behavior,» *Journal of Biomedical Material Research*, pp. 927-935, 2007.
- [90] S. Goodman, Z. Yao, M. Keeney e F. Yang, «The future of biologic coatings for orthopaedic implants,» *Biomaterials*, pp. 3174-3183, 2013.
- [91] A. Santos, M. Caldas, P. Pattekari, C. Ribeiro, A. Ribeiro, Y. Lvov e F. Veiga, «Chapter 16 - Layer-by-Layer coated drug-core nanoparticles as versatile delivery platforms,» in *Design and Development of New Nanocarriers*, Elsevier - William Andrew, 2018, pp. 595-635.
- [92] W. Men, P. Zhu, S. Dong, W. Liu, K. Zhou, Y. Bai, X. Liu, S. Gong e S. Zhang, «Layer-by-layer pH-sensitive nanoparticles for drug delivery and controlled release with improved therapeutic efficacy in vivo,» *Drug Delivery*, pp. 180-190, 2020.
- [93] Y. Singh, J. Meher, K. Raval, F. Khan, M. Chaurasia, N. Jain e M. Chourasia, «Nanoemulsion: Concepts, development and applications in drug delivery,» *Journal of Controlled Release*, pp. 28-49, 2017.
- [94] K. Gurpreet e S. Singh, «Review of Nanoemulsion Formulation and Characterization Techniques,» *Indian Journal of Pharmaceutical Science*, pp. 781-789, 2018.
- [95] P. Bhatt e S. Madhav, «A detailed review on nanoemulsion drug delivery system,» *International Journal of Pharmaceutical Sciences and Research*, pp. 2482-2489, 2011.
- [96] M. Jaiswal, R. Dudhe e P. Sharma, «Nanoemulsion: an advanced mode of drug delivery system,» *3 Biotech*, p. 123-127, 2015.
- [97] J. Li e S. Zhuang, «Antibacterial activity of chitosan and its derivatives and their interaction mechanism with bacteria: Current state and perspectives,» *European Polymer Journal*, 2020.
- [98] R. Goy, D. De Britto e O. Assis, «A Review of the Antimicrobial Activity of Chitosan,» *Polimeros*, pp. 241-247, 2009.
- [99] H. Yilmaz Atay, «Antibacterial Activity of Chitosan-Based Systems,» in *Functional Chitosan - Drug Delivery and Biomedical Applications*, Springer, 2019, pp. 457-489.
- [100] M. Hosseinnejad e S. Jafari, «Evaluation of different factors affecting antimicrobial properties of chitosan,» *International Journal of Biological Macromolecules*, pp. 467-475, 2016.
- [101] D. Perinelli, L. Fagioli, R. Campana, J. Lam, W. Baffone, G. Palmieri, L. Casettari e G. Bonacucina, «Chitosan-based nanosystems and their exploited antimicrobial activity,» *European Journal of Pharmaceutical Sciences*, pp. 8-20, 2018.
- [102] M. Johnston, M. McBride, D. Dahiya, R. Owusu-Apenten e P. Nigam, «Antibacterial activity of Manuka honey and its components: An overview,» *AIMS Microbiology*, pp. 655-664, 2018.
- [103] J.-M. Alvarez-Suarez, M. Gasparrini, T. Forbes-Hernandez, L. Mazzoni e F. Giampieri, «The Composition and Biological Activity of Honey: A Focus on Manuka Honey,» *Foods*, pp. 420-432, 2014.
- [104] A. Roberts, H. Brown e R. Jenkins, «On the antibacterial effects of manuka honey: mechanistic insights,» *Research and Reports in Biology*, p. 215-224, 2015.
- [105] N. Cokcetin, M. Pappalardo, L. Campbell, P. Brooks, D. Carter, S. Blair e E. Harry, «The Antibacterial Activity of Australian Leptospermum Honey Correlates with Methylglyoxal Levels,» *PLoS ONE*, 2016.
- [106] D. Carter, S. Blair, N. Cokcetin, D. Bouzo, P. Brooks, R. Schothauer e E. Harry, «Therapeutic Manuka Honey: No Longer So Alternative,» *Frontiers in Microbiology*, 2016.
- [107] A. Henriques, R. Jenkins, N. Burton e R. Cooper, «The intracellular effects of manuka honey on Staphylococcus aureus,» *European Journal of Clinical Microbiology & Infectious Diseases*, pp. 45-50, 2009.
- [108] A. Henriques, R. Jenkins, N. Burton e R. Cooper, «The effect of manuka honey on the structure of Pseudomonas aeruginosa,» *European Journal of Clinical Microbiology & Infectious Diseases*, pp. 167-171, 2010.

- [109] F. El-Senduny, N. Hegazi, G. Abd Elghani e M. Farag, «Manuka honey, a unique mono-floral honey. A comprehensive review of its bioactives, metabolism, action mechanisms, and therapeutic merits,» *Food Bioscience*, 2021.
- [110] M. Hanif, S. Nisar, G. Khan, Z. Mushtaq e M. Zubair, «Chapter 1: Essential Oils,» in *Essential Oil Research Trends in Biosynthesis, Analytics, Industrial Applications and Biotechnological Production*, Springer Nature Switzerland, 2019.
- [111] F. Bakkali, S. Averbeck, D. Averbeck e M. Idaomar, «Biological effects of essential oils – A review,» *Food and Chemical Toxicology*, p. 446–475, 2008.
- [112] S. Chouhan, K. Sharma e S. Guleria, «Antimicrobial Activity of Some Essential Oils—Present Status and Future Perspectives,» *Medicines*, 2017.
- [113] W. Dhifi, S. Bellili, S. Jazi, N. Bahloul e W. Mnif, «Essential Oils' Chemical Characterization and Investigation of Some Biological Activities: A Critical Review,» *Medicines*, 2016.
- [114] F. Nazzaro, F. Fratianni, L. De Martino, R. Coppola e V. De Feo, «Effect of Essential Oils on Pathogenic Bacteria,» *Pharmaceuticals*, pp. 1451-1474, 2013.
- [115] K. Hüsnü, C. Başer e F. Demirci, «4 Chemistry of Essential Oils,» in *Flavours and Fragrances. Chemistry, Bioprocessing and Sustainability*, Springer, 2007, p. 43–86.
- [116] J. Raut e S. Karuppaiyil, «A status review on the medicinal properties of essential oils,» *Industrial Crops and Products*, pp. 250-264, 2014.
- [117] X. Zhang, D. Liu, T. Jin, W. Chen, Q. He, Z. Zou, H. Zhao, X. Ye e M. Guo, «Preparation and characterization of gellan gum-chitosan polyelectrolyte complex films with the incorporation of thyme essential oil nanoemulsion,» *Food Hydrocolloids*, 2021.
- [118] E. Mancuso, C. Tonda-Turo, C. Ceresa, V. Pensabene, S. Connell, L. Fracchia e P. Gentile, «Potential of Manuka Honey as a Natural Polyelectrolyte to Develop Biomimetic Nanostructured Meshes With Antimicrobial Properties,» *Frontiers in Bioengineering and Biotechnology*, 2019.
- [119] S. Moradi e A. Barati, «Essential Oils Nanoemulsions: Preparation, Characterization and Study of Antibacterial Activity against Escherichia Coli,» *International Journal of Nanoscience and Nanotechnology*, pp. 199-210, 2019.
- [120] T. Laid, K. Abdelhamid, L. Eddine e B. Abderrhmane, «Optimizing the biosynthesis parameters of iron oxide nanoparticles using central composite design,» *Journal of Molecular Structure*, 2021.
- [121] D. M. Danaei, M. Dehghankhold, S. Ataei, F. Hasanzadeh Davarani, R. Javanmard, A. Dokhani, S. Khorasani e R. Mozafari, «Impact of Particle Size and Polydispersity Index on the Clinical Applications of Lipidic Nanocarrier Systems,» *Pharmaceutics*, 2018.
- [122] F. Pinto, D. De Barros, C. Reis e L. Fonseca, «Optimization of nanostructured lipid carriers loaded with retinoids by central composite design,» *Journal of Molecular Liquids*, 2019.
- [123] I. Roland, G. Piel, L. Delattre e B. Evrard, «Systematic characterization of oil-in-water emulsions for formulation design,» in *International Journal of Pharmaceutics*, 2003, pp. 85-94.
- [124] L. Pavoni, D. Perinelli, G. Bonacucina, M. Cespi e G. Palmieri, «An Overview of Micro- and Nanoemulsions as Vehicles for Essential Oils: Formulation, Preparation and Stability,» *Nanomaterials*, 2020.
- [125] «The Open University,» [Online]. Available: <http://www9.open.ac.uk/emsuite/services/negative-staining-tem>.
- [126] B. Scientific. [Online]. Available: <https://www.bioline.com/measurements/qcm-d#how-does-qcm-d-work>.
- [127] H. Deligoz e B. Tiede, «QCM-D study of layer-by-layer assembly of polyelectrolyte blend films and their drug loading-release behavior,» *Colloids and Surfaces A: Physicochemical and Engineering Aspects*, 2014.
- [128] T. Elzein e e. al., «FTIR study of polycaprolactone chain organization at interfaces,» *Journal of Colloid and Interface Science*, 2004.
- [129] R. Thomas, K. Soumya, J. Mathew e e. al., «Electrospun Polycaprolactone Membrane Incorporated with Biosynthesized Silver Nanoparticles as Effective Wound Dressing Material,» *Applied Biochemistry and Biotechnology*, 2015.
- [130] S. Tariq, L. Irusta, M. Fernandez e M. Paulis, «Kinetic study of crosslinking between acetoacetoxy and hexamethylene diamine functionalized waterborne latexes in two-pack systems,» *Progress in Organic Coatings*, 2022.
- [131] «IR Spectrum Table & Chart,» [Online]. Available: <https://www.sigmaaldrich.com/IT/en/technical-documents/technical-article/analytical-chemistry/photometry-and-reflectometry/ir-spectrum-table>.
- [132] E. Mancuso, C. Tonda-Turo, C. Ceresa, V. Pensabene, S. Connell, L. Fracchia e P. Gentile, «Potential of Manuka Honey as a Natural Polyelectrolyte to Develop Biomimetic Nanostructured Meshes With Antimicrobial Properties,» *Frontiers in Bioengineering and Biotechnology*, 2019.
- [133] G. Lawrie e e. al., «Interactions between Alginate and Chitosan Biopolymers Characterized Using FTIR and XPS,» *Biomacromolecules*, 2007.
- [134] Y. Li, D. Kong e H. Wu, «Analysis and evaluation of essential oil components of cinnamon barks using GC–MS and FTIR spectroscopy,» *Industrial Crops and Products*, 2013.
- [135] L. Lin, Y. Dai e H. Cui, «Antibacterial poly(ethylene oxide) electrospun nanofibers containing cinnamon essential oil/beta-cyclodextrin proteoliposomes,» *Carbohydrate Polymers*, 2017.
- [136] «Typical IR Absorption Frequencies For Common Functional Groups,» [Online]. Available: <https://www.niu.edu/clas/chembio/research/analytical-lab/ftir/ir-frequencies-table.shtml>.
- [137] D. Gallart-Mateu, C. Largo-Arango, T. Larkman, S. Garrigues e M. de la Guardia, «Fast authentication of tea tree oil through spectroscopy,» *Talanta*, 2018.
- [138] Y. Xiong e e. al., «Study on the bonding state for carbon–boron nitrogen with different ball milling time,» *Applied Surface Science*, 2006.
- [139] Q. Xu, P. Wang e e. al., «Aerosol self-assembly synthesis of g-C<sub>3</sub>N<sub>4</sub>/MXene/Ag<sub>3</sub>PO<sub>4</sub> heterostructure for enhanced photocatalytic degradation of tetracycline hydrochloride,» *Colloids and Surfaces A: Physicochemical and Engineering Aspects*, 2022.
- [140] C. Cheng, Z. Liye e R.-J. Zhan, «Surface modification of polymer fibre by the new atmospheric pressure cold plasma jet,» *Surface and Coatings Technology*, 2006.
- [141] S. Zhang, X. Ji e e. al., «One-step synthesis of yellow-emissive carbon dots with a large Stokes shift and their application in fluorimetric imaging of intracellular pH,» *Spectrochimica Acta Part A: Molecular and Biomolecular Spectroscopy*, 2020.

- [142] C. Karthikeyan e e. al., «Biomolecule chitosan, curcumin and ZnO-based antibacterial nanomaterial, via a one-pot process,» *Carbohydrate Polymers*, 2020.
- [143] R. Al-Gaashani e e. al., «XPS and structural studies of high quality graphene oxide and reduced graphene oxide prepared by different chemical oxidation methods,» *Ceramics International*, 2019.
- [144] Y. Gong e Z. Dong, «Transfer, transportation, and accumulation of cerium-doped carbon quantum dots: Promoting growth and development in wheat,» *Ecotoxicology and Environmental Safety*, 2021.
- [145] C. Zhang e e. al., «Molecular engineering of donor-acceptor structured g-C<sub>3</sub>N<sub>4</sub> for superior photocatalytic oxytetracycline degradation,» *Chemical Engineering Journal*, 2022.
- [146] Z. Zhou e e. al., «Bilayer porous scaffold based on Poly-(ε-caprolactone) nanofibrous membrane and gelatin sponge for favoring cell proliferation,» *Applied Surface Science*, 2011.
- [147] X. Qin e e. al., «Molybdenum sulfide/citric acid composite membrane-coated long period fiber grating sensor for measuring trace hydrogen sulfide gas,» *Sensors and Actuators B: Chemical*, 2018.
- [148] Z. Ye, Q. Wei e e. al., «ighly-efficient perovskite solar cells based on controllable oxygen defects in tin oxide electron transport layers,» *Ceramics International*, 2022.
- [149] A. Agrawal e e. al., «Anomalous band bowing in pulsed laser deposited Mg<sub>x</sub>Zn<sub>1-x</sub>O films,» *Journal of Crystal Growth*, 2013.
- [150] M. Murugesan e e. al., «Facile preparation of reduced graphene oxide wrapped copper oxide thin film solar selective absorbers,» *Ceramics International*, 2020.
- [151] L. Dlamini e e. al., «A composite of platelet-like orientated BiVO<sub>4</sub> fused with MIL-125(Ti): Synthesis and characterization,» *Nature - scientific reports*, 2019.
- [152] X. Liu, T. Wang e e. al., «A tailored molecular imprinting ratiometric fluorescent sensor based on red/blue carbon dots for ultrasensitive tetracycline detection,» *Journal of Industrial and Engineering Chemistry*, 2019.
- [153] B. Liu, B. Zheng e e. al., «Performance evaluation of hierarchical and conductive fabric-based electrodes decorated with amorphous FeB nanosheets,» *Cellulose*, 2020.
- [154] Q. Zhao e e. al., «Structure and properties of Si and N co-doping on DLC film corrosion resistance,» *Ceramics International*, 2023.
- [155] K. Zeng e e. al., «One-step methodology for the direct covalent capture of GPCRs from complex matrices onto solid surfaces based on the bioorthogonal reaction between haloalkane dehalogenase and chloroalkanes,» *Royal society of chemistry*, 2018.
- [156] Y. Zhou e e. al., «The novel N-rich hard carbon nanofiber as high-performance electrode materials for sodium-ion batteries,» *Ceramics International*, 2021.
- [157] X. Guo e e. al., «An efficient method for tylosin removal from an aqueous solution by goethite modified straw mass,» *Royal society of chemistry*, 2016.
- [158] M. El-Morsy e e. al., «Optimizing the mechanical and surface topography of hydroxyapatite/Gd<sub>2</sub>O<sub>3</sub>/graphene oxide nanocomposites for medical applications,» *Journal of Saudi Chemical Society*, 2022.
- [159] A. Khoshnood e e. al., «Synthesis of a Biological-Based Glycoluril with Phosphorous Acid Tags as a New Nanostructured Catalyst: Application for the Synthesis of Novel Natural Henna-Based Compounds,» *Chemistry select*, 2018.
- [160] C. Zhou e e. al., «Construction and characterization of an antibacterial/anticoagulant dual-functional surface based on poly l-lactic acid electrospun fibrous mats,» *Materials Science and Engineering: C*, 2018.
- [161] J. Jiang e e. al., «Non-fluorinated superhydrophobic and micro/nano hierarchical Al doped ZnO film: the effect of Al doping on morphological and hydrophobic properties,» *Royal society of chemistry*, 2015.
- [162] Z. Fu e e. al., «Hydroxylated high-entropy alloy as highly efficient catalyst for electrochemical oxygen evolution reaction,» *Science China Materials*, 2020.
- [163] P. Makal e D. Das, «Self-doped TiO<sub>2</sub> nanowires in TiO<sub>2</sub>-B single phase, TiO<sub>2</sub>-B/anatase and TiO<sub>2</sub>-anatase/rutile heterojunctions demonstrating individual superiority in photocatalytic activity under visible and UV light,» *Applied Surface Science*, 2018.
- [164] T. Andy Hor e e. al., «Platinum Deposition on Carbon Nanotubes via Chemical Modification,» *Chemistry of materials*, 1998.
- [165] A. Di Clasi e e. al., «Electrochemical performance investigation of electrospun urchin-like V<sub>2</sub>O<sub>3</sub>-CNF composite nanostructure for vanadium redox flow battery,» *Electrochimica Acta*, 2017.
- [166] Y. Chen e e. al., «Synthesis and electrochemical performance of gold nanoparticles deposited onto a reduced graphene oxide/nickel foam hybrid structure for hydrazine detection,» *Journal of Materials Science*, 2020.
- [167] C. Qin e e. al., «Nickel oxide/sulfide nanoparticle-embedded porous carbon prepared from kelp for excellent asymmetrical supercapacitors and microwave absorbers,» *Journal of Alloys and Compounds*, 2022.
- [168] S. Zhang e e. al., «Preparation of TiO<sub>2</sub> films by layer-by-layer assembly and their application in solar cell,» *Journal of Alloys and Compounds*, 2010.
- [169] J. Liang e e. al., «Fast-thermoreponsive carboxylated carbon nanotube/chitosan aerogels with switchable wettability for oil/water separation,» *Journal of Hazardous Materials*, 2022.
- [170] X. Na Wang e e. al., «The Improvement of Performance of HfO<sub>2</sub>/Gd<sub>2</sub>O<sub>3</sub>/Si Stack Compared with Gd-Doped HfO<sub>2</sub> High-K Films,» *Materials Science Forum*, 2011.
- [171] J. Zhang e e. al., «Application of CO<sub>2</sub>-storage materials as a novel plant growth regulator to promote the growth of four vegetables,» *Journal of CO<sub>2</sub> Utilization*, 2018.
- [172] Y. Zhou e e. al., «Magnetic MgFe<sub>2</sub>O<sub>4</sub>/biochar derived from pomelo peel as a persulfate activator for levofloxacin degradation: Effects and mechanistic consideration,» *Bioresource Technology*, 2022.
- [173] Q. Zheng e e. al., «Micro-diamond assisted bidirectional tuning of thermal conductivity in multifunctional graphene nanoplatelets/nanofibrillated cellulose films,» *Carbon*, 2022.

- [174] X. Lin e e. al., «Facile Microwave-Assisted Synthesis of Functionalized Carbon Nitride Quantum Dots as Fluorescence Probe for Fast and Highly Selective Detection of 2,4,6-Trinitrophenol,» *Journal of Fluorescence*, 2021.
- [175] S. Li e e. al., «Solvent- and catalyst-free synthesis of an azine-linked covalent organic framework and the induced tautomerization in the adsorption of U(vi) and Hg(ii),» *Green Chemistry*, 2019.
- [176] M. Raghu e e. al., «Moringa Oleifera leaf extract mediated synthesis of reduced graphene oxide-vanadium pentoxide nanocomposite for enhanced specific capacitance in supercapacitors,» *Inorganic Chemistry Communications*, 2022.
- [177] Priya, A. Sharma, B. Kaith e e. al., «Synthesis of dextrin-polyacrylamide and boric acid based tough and transparent, self-healing, superabsorbent film,» *International Journal of Biological Macromolecules*, 2021.
- [178] J. Shen e e. al., «Diethylenetriaminepentaacetic Acid (DPTA)-modified Magnetic Cellulose Nanocrystals can Efficiently Remove Pb(II) from Aqueous Solution,» *Journal of Polymers and the Environment*, 2022.
- [179] G. Cheng e e. al., «Direct Ink Writing of Hierarchically Porous Cellulose/Alginate Monolithic Hydrogel as a Highly Effective Adsorbent for Environmental Applications,» *ACS Applied Polymer Materials*, 2021.
- [180] M. Kulandainathan e e. al., «Electrochemical sensing of dopamine at the surface of a dopamine grafted graphene oxide/poly(methylene blue) composite modified electrode,» *Royal society of chemistry*, 2016.
- [181] J. Chen e e. al., «Structural and mechanical properties of nitrogen ion implanted ultra high molecular weight polyethylene,» *Surface and Coatings Technology*, 2001.
- [182] N. Wang e e. al., «DNA nano-pocket for ultra-selective uranyl extraction from seawater,» *Nature Communications*, 2020.
- [183] T. Hattori e e. al., «Composition, chemical structure, and electronic band structure of rare earth oxide/Si(1 0 0) interfacial transition layer,» *Microelectronic Engineering*, 2004.
- [184] M. Pishko e e. al., «Encapsulation of Drug Nanoparticles in Self-Assembled Macromolecular Nanoshells,» *Langmuir*, 2005.
- [185] L. Deng e e. al., «Coupling of Bi<sub>2</sub>O<sub>3</sub> nanoparticles with g-C<sub>3</sub>N<sub>4</sub> for enhanced photocatalytic degradation of methylene blue,» *Ceramics International*, 2021.
- [186] L. Zhang e e. al., «Layer-by-layer assembly of chitosan/tungstosilicate acid-Ag nanocomplex with electrocatalytic properties,» *Journal of Materials Chemistry*, 2009.
- [187] S. Guo e e. al., «Room temperature gas sensing under UV light irradiation for Ti<sub>3</sub>C<sub>2</sub>T<sub>x</sub> MXene derived lamellar TiO<sub>2</sub>-C/g-C<sub>3</sub>N<sub>4</sub> composites,» *Applied Surface Science*, 2021.
- [188] C. Liu e e. al., «Enhanced interfacial and mechanical properties of basalt fiber reinforced poly(aryl ether nitrile ketone) composites by amino-silane coupling agents,» *Polymer*, 2021.
- [189] X. Yin, H. Gu e e. al., «Highly fluorescent N doped C-dots as sensor for selective detection of Hg<sup>2+</sup> in beverages,» *Spectrochimica Acta Part A: Molecular and Biomolecular Spectroscopy*, 2022.
- [190] C. Long e e. al., «Porous polymeric resin for adsorbing low concentration of VOCs: Unveiling adsorption mechanism and effect of VOCs' molecular properties,» *Separation and Purification Technology*, 2019.
- [191] N. Li e R. Bai, «Novel modification of chitosan hydrogel beads for improved properties as an,» 2004.
- [192] P. Wang e e. al., «Copper and molybdenum dioxide co-doped octahedral porous carbon framework for high sensitivity electrochemical detection of hydrogen peroxide,» *Ionics*, 2022.
- [193] Y. Liang e e. al., «Friction and wear behaviors of carbon and aramid fibers reinforced polyimide composites in simulated space environment,» *Tribology International*, 2015.
- [194] Z. Ai e e. al., «Facile fabrication of graphitization-enhanced wrinkled paper-like N-doped porous carbon via a ZnCl<sub>2</sub>-modified NaCl-templating method for use as an anode in lithium ion batteries,» *Sustainable Energy & Fuels*, 2020.
- [195] M. Nagano e e. al., «Deposition and characterization of carbon nitride films from hexamethylenetetramine/N<sub>2</sub> by microwave plasma-enhanced chemical vapor deposition,» *Applied Surface Science*, 2005.
- [196] R. Duval e C. Duplais, «Fluorescent natural products as probes and tracers in biology,» *Natural Product Reports*, 2017.
- [197] J. Rückriemen, C. Hohmann, M. Hellwig e T. Henle, «Unique fluorescence and high-molecular weight characteristics of protein isolates from manuka honey (*Leptospermum scoparium*),» *Food Research International*, pp. 469-475, 2017.
- [198] M. Zhang, C. Zhang, Z. Li, X. Fu e S. Huang, «Advances in 3D skin bioprinting for wound healing and disease modeling,» *Regenerative Biomaterials*, 2023.
- [199] W. Lu e e. al., «Preparation, characterization, and antimicrobial activity of nanoemulsions incorporating citral essential oil,» *Journal of food and drug analysis*, pp. 82-89, 2017.